BIOFUNCTIONAL MATERIALS FOR THE MODULATION OF MACROPHAGE PHENOTYPE AND POLARIZATION

By

Shann Say Yu

Dissertation

Submitted to the Faculty of the

Graduate School of Vanderbilt University

in partial fulfillment of the requirements

for the degree of

DOCTOR OF PHILOSOPHY

in

Biomedical Engineering

December, 2012

Nashville, Tennessee

Approved:

Professor Todd D. Giorgio

Professor Fiona E. Yull

Professor Hak-Joon Sung

Professor Craig L. Duvall

Professor David G. Harrison

ACKNOWLEDGMENTS

My work is primarily supported by multiple awards and grants through the Department of Defense CDMRP Breast Cancer Research Program (#W81XWH-10-1-0684, #W81XWH-11-1-0344, & #W81XWH-11-1-0242). For some of the work presented here, I also acknowledge financial support through grants from the National Science Foundation (NSF CAREER CBET 1056046, NSF DMR 1006558), National Institutes of Health (NIH HL091465), and a Vanderbilt University Internal Discovery Grant (4-48-999-9132). I am also grateful to the Vanderbilt University Graduate School for a 2012 Dissertation Enhancement Grant that supported my travel to the University of Washington for a clinical tumor immunology internship, and multiple Travel Awards that funded my trips to multiple conferences across the nation to present my work and develop my professional network.

First of all, I am thankful to the God of the heavens—who created the world as we know it today as partially explained through a combination of the Big Bang Theory, evolution, and other mechanisms that our scientific community continues to unravel every day—and who gave me my identity and granted me my talents, interests, and background to pursue my lifelong mission of contributing to the development of cures to diseases with unmet needs. I am also grateful for the members of my family who have been very supportive in my goals and dreams throughout life. I am thankful for the best parents in the world for their love and support. I am also grateful for my brother, Shaun, who has always been my best friend in every turn of life.

Throughout my time at Vanderbilt, I have had the pleasure of working and collaborating with some of the sharpest, most insightful scientific minds in the world today. Profs. Hak-Joon Sung, Craig Duvall, Fiona Yull, and David Harrison have all been very helpful in promoting my progress, and in bringing up alternative interpretations, approaches, and directions to my research. Their perspectives have also guided and shaped my views on careers and life. In particular, I would like to thank Prof. Todd Giorgio, my mentor and chairman of my committee. In addition to his instrumental role in my professional development as a scientist, he has always openly shared

anecdotes and experiences that have been nothing but insightful, uplifting, and encouraging at various steps along the way. I would also like to thank Becca Thomason, David Bader, Bob Matthews, Carol Ann Bonner, Daniel Colvin, Daniel Perrien, Melissa Skala, and Jared Weis for letting me use equipment in their labs and for their input in helping make some of our experiments work.

In the summer of 2012, funded by a Dissertation Enhancement Grant, I traveled to the Tumor Vaccine Group at the University of Washington in Seattle, to work with a group that performed clinical trials for breast cancer vaccines. I had the opportunity to learn from some of the minds at the forefront of tumor immunology, especially from Chihiro Morishima and Nora Disis. I learned volumes about clinical and translational research in two short months with them, and this experience greatly supplements the years of basic and pre-clinical research I have under my belt.

In similar fashion, I have also interacted professionally with a lot of fellow scholars-in-training who have been my co-workers and friends along the way. This list includes, most notably: Ryan Ortega, Spencer Crowder, Chris Nelson, Angela Zachman, Whitney Barham, Charleson Bell, Hongmei Li, Amanda Lowery, Josh Trantum, Ian McFadden, Randy Scherer, Brian Evans, Mukesh Gupta, Tim Boire, Jason Tucker-Schwartz, and Martina Miteva. I have also had the opportunity to work with and/or mentor a number of undergraduate students and rotation students, including Chadwick Augusty, Nathan Bloodworth, Rebecca Hudson, Rachel Koblin, Travis Meyer, Chelsey Smith, and most of all—Cheryl Lau. Thank you for your invaluable contributions to my work, and for helping me be a better teacher and communicator every day.

My spiritual and personal growth and wellbeing has also been nurtured through the many positive, supportive, and uplifting people I have had the pleasure of meeting and fellowshipping with through the Graduate Christian Fellowship (formerly here at Vanderbilt), including: Jonathan Warren and Tish Harrison-Warren, Rory Pruitt, Will and Christi French, Laura Anzaldi, Chris Mike, Stephen Santana, Ron and Barbara Zimmer, Lindy and Josh Colombini, Alison Schroer, Brad Kiddie, Chris and Trish Pino, Jason Ingalls, Liz Ferrick, Monica Lacy, and Laura Hover. And to other friends, family, and colleagues here at Nashville, Texas, Seattle, and beyond who are too many to list here, thank you for your love, help, and support!

TABLE OF CONTENTS

LIST OF TABLES

LIST OF FIGURES

LIST OF ABBREVIATIONS

AEMA	Aminoethyl methacrylate
AzEMA	2-Azidoethyl methacrylate
AzPMA	3-Azidopropyl methacrylate
BMA	Butyl methacrylate
CD204	Macrophage Scavenger Receptor A-I
CD206	Mannose receptor
CTL	Cytotoxic T Lymphocyte
DC	Dendritic cell
DLS	Dynamic light scattering
DMAEMA	2-(Dimethylamino)ethyl methacrylate
ECT	*S*-ethyl-*S'*-(4-cyanovalerate)-4-trithiocarbonate
GPC	Gel permeation chromatography (size-exclusion chromatography)
HPMA	3-Hydroxypropyl methacrylate
IFN	Interferon
iNOS / NOS2	Inducible Nitric Oxide Synthase
MACS	Magnet-assisted Cell Sorting
MALS	Multi-angle static light scattering
ManNP	Mannosylated nanoparticles
MDSC	Myeloid-derived suppressor cell
MMP	Matrix metalloproteinases
MφT	Macrophage-targeted
NF-κB	Nuclear factor κB

NMR	Nuclear magnetic resonance
oEGMA	Oligoethylene glycol methacrylate
oxLDL	Oxidized Low-density lipoprotein
P_5	Peptide sequence: Ac-KPPPPPK-Amide
P_7	Peptide sequence: Ac-KPPPPPPPK-Amide
P_{10}	Peptide sequence: Ac-KPPPPPPPPPPK-Amide
PA	Proximity-activated
PAA	Propylacrylic acid
PEG	Poly(ethylene glycol)
PPS	Poly(propylene sulfide)
PyMT	Polyoma Middle T
RAFT	Reverse addition-fragmentation chain-transfer
ROS	Reactive Oxygen Species
SIN-1	3-morpholinosydnonimine
STAT	Signal transducer and activation of transcription
TAM	Tumor-associated macrophage
TNF	Tumor necrosis factor
USPIO	Ultrasmall superparamagnetic iron oxides

CHAPTER I

INTRODUCTION

Macrophages have been proposed as a potential therapeutic target because of their central role in the progression of cancer and cardiovascular disease. This is mediated through their potent effector functions on the rest of the immune system. In particular, macrophages demonstrate the ability to secrete a wide range of intercellular signals, including pro-inflammatory cytokines and chemokines, as well as growth factors and angiogenic signals (Brown & Goldstein, 1983; Devaraj & Jialal, 2011; A. Mantovani, Sozzani, Locati, Allavena, & Sica, 2002; Miselis, Wu, Van Rooijen, & Kane, 2008; Ribatti, Levi-Schaffer, & Kovanen, 2008). The diversity of the macrophage secretome is linked to the polarization state of these cells. Through environmental triggers, macrophages can be directed into performing a spectrum of functions, with the pro-inflammatory "M1" state and the anti-inflammatory, pro-healing "M2" state at opposite ends (Mosser & Edwards, 2008). Recent evidence demonstrates the prevalence of M2-polarized and M1-polarized macrophages in tumors and in atherosclerotic plaques, respectively (Hirose et al., 2011; A. Sica et al., 2008). The re-polarization of macrophages may present a promising strategy for the treatment of these diseases, but while some methods have emerged, a vast majority of them are not clinically translatable—involving methods that have produced a slew of critical side effects in humans (e.g. systemic cytokine therapy).

Through nanomaterials, macrophage-specific targeting may be achieved in a clinically-translatable fashion. The emergence of 'smart' biomaterials and nanoparticles has led to a new paradigm in the design of drug delivery platforms—producing injectable materials that circulate as inactive prodrugs until their activation at sites of disease, as well as homing drugs that target pathologically-specific biomarkers. Because macrophages are among the most phagocytic cells in the body, and further, have been observed as permanent residents in various organs—including the liver and bone marrow, the injection of nanomaterials into animal models has usually resulted in the accumulation of the materials in such organs. Therefore, site-specific targeting of nanomaterials to macrophages at diseased sites stands as a significant challenge to the success of this therapeutic strategy.

We have developed MMP-activatable nanoparticles that respond to local MMP activity by unveiling cell-specific ligands. This enables the localization of nanoparticles to sites that present two features—MMP activity and a cell type of interest (Sewell & Giorgio, 2009; Smith, Sewell, & Giorgio, 2008). We will apply these nanoparticles for the delivery of siRNA to macrophages, with the goals of modifying their phenotype and polarization. Finally, the clinical relevance of this strategy will be assessed in mouse models of metastatic human cancer.

Objectives

The central hypothesis of my dissertation is that the polarization of macrophages into pro-inflammatory and anti-inflammatory subtypes facilitates their important

functions in promoting human diseases—including cancer and cardiovascular disease. Through the delivery of siRNA, it would be possible to modify macrophage polarization (ie, inducing M1 polarization in M2 macrophages and vice versa), resulting in therapeutic benefits. Therefore, the objectives of this work are to (1) develop novel biomaterials to enable macrophage-targeted drug delivery, as well as (2) to investigate the use of siRNA to modulate macrophage polarization.

Specific Aims

Specific Aim 1. Macrophage-specific nanoparticles will be assembled, containing multifunctional polymers that have the capability of condensing siRNA, as well as targeting motifs to macrophage endocytic receptors (scavenger receptors and mannose receptor are candidates). Optimization of nanoparticle targeting and endosomolytic behavior will be performed here.

Specific Aim 2. M1 or M2 macrophages will be induced *in vitro*, providing a system for identification of siRNA sequences that can swing the polarization into the opposite direction. Measurements of cytokine release (cytokine bead arrays), gene expression of M1/M2-related biomarkers (real time PCR), and reactive oxygen species will be used in order to assess M1 or M2 polarization.

Specific Aim 3. The marriage of the first two aims should produce a macrophage-specific siRNA-delivering construct suitable for *in vivo* administration. To enhance the clinical relevance of this work, these immunomodulatory nanoparticles will be

delivered to mice with metastatic cancer. Nanoparticle homing will be assessed, as well as the effects of treatment on mouse survival and tumor burden. Tumor-associated macrophages will also be analyzed for changes in gene expression by real time PCR.

Background and Significance

For my dissertation, I proposed to synthesize 'smart' nanomaterials that home in on macrophages located within their areas of highest activity (MMP release / ROS release). The proposed nanoparticles will then be endocytosed, escape the endosomes in response to lower pH (characteristic of late endosomes), and deliver siRNA into the cytosol. Knockdown of target genes is expected to elicit desired changes in macrophage polarization. Ultimately, this strategy is intended to 'jump-start' quiescent macrophage functions in order to produce potential therapeutic benefits in human disease. In this section, I will discuss macrophage biology in relation to cancer and cardiovascular disease, and review previous work by others that guides the design of macrophage-targeted biomaterials.

Macrophage Polarization: Pro- versus Anti-inflammatory

The immune system has evolved to be specialized in the clearance of foreign debris from the body. An intricate network of intercellular signaling, involving a coordinated effort of multiple cell types over various time scales—regulates the powerful ability of the immune system to discriminate self from non-self. The

effector arms of the immune system center on the $CD4^+$ T-helper (Th) cells, which receive stimuli from leukocytes among others, and respond by activating the

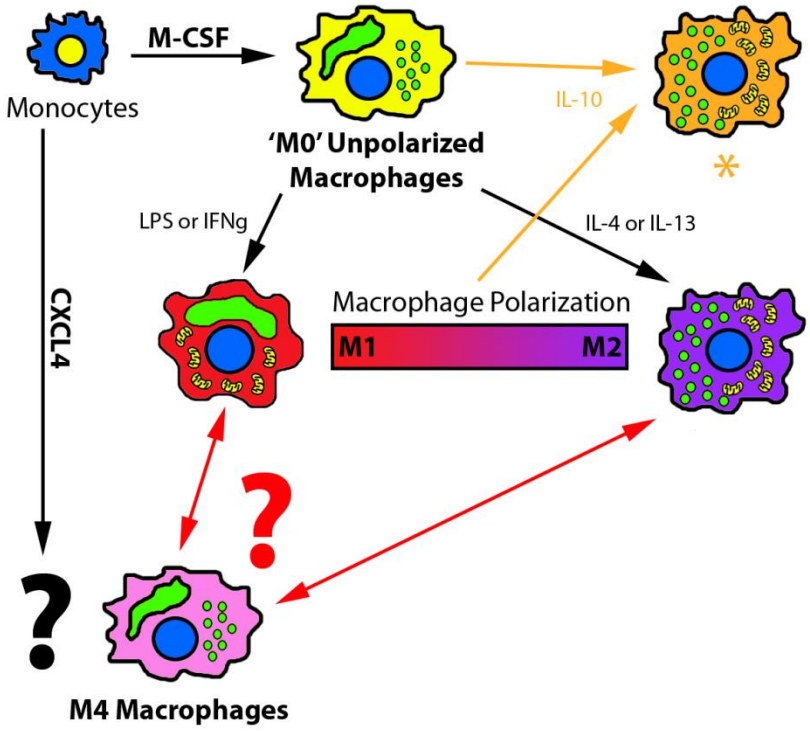

FIGURE 1. Monocyte differentiation into macrophages and macrophage polarization. Circulating monocytes can differentiate into macrophages via the cytokines M-CSF or CXCL4, resulting in very different macrophage phenotypes. The latter has been dubbed the M4 macrophage, and to date have not been completely characterized (Gleissner, Shaked, Little, & Ley, 2010). Macrophages that have been differentiated via M-CSF are capable of being primed by local LPS or IFNγ to produce M1 pro-inflammatory macrophages or via IL-4 or IL-13 to produce alternatively activated M2 macrophages. The presence of IL-10 deactivates the macrophages (*), resulting in a very different expression profile from M1 and M2 macrophages, but these macrophages are still commonly classified as M2 macrophages. Nevertheless, M1 and M2 macrophages represent two poles in a spectrum of macrophage polarization, and these versatile cell types maintain the ability to re-polarize to different phenotypes throughout their lifetime.

appropriate immune system responses. Often, these downstream responses are classified into Th1 responses—involving eradication of viruses and intracellular pathogens (cell-mediated immunity)—or Th2 responses, which result in the

construction of antibody libraries specific for blood-borne and extracellular pathogens (humoral immunity). The Th1/Th2 paradigm continues to drive immunological research today (Scott, 1993). Analogous to this spectrum of Th-mediated inflammatory activity, macrophages have been typically classified into M1 or M2 cells, depending on their 'classical activation' via IFNγ/LPS or 'alternative activation' via IL-4/IL-13 (Gordon, 2003; A. Mantovani, et al., 2002). Unlike Th1 and Th2 cells, M1 and M2 macrophages have not, to date, been observed in pure form *in vivo*. This suggests that macrophage phenotype and activity tends to fall within a spectrum with the M1 and M2 phenotypes on opposite poles, and supports recent thought that macrophages maintain a great degree of functional plasticity in their life cycle (Figure 1) (Mosser & Edwards, 2008). To reflect the current understanding of macrophage polarization and activity, M1-like and M2-like macrophages will be hereafter denoted as *pro-inflammatory* or *anti-inflammatory* macrophages.

As implied by this classification system and confirmed extensively *in vitro* and *in vivo*, macrophages are very involved in the clearance of pathogens and foreign debris (Kindt, Goldsby, Osborne, & Kuby, 2007). To complicate matters, macrophages have also been shown to facilitate the wound healing process by releasing an array of growth factors and pro-angiogenic factors, including EGF, PDGF, VEGF, TGF-β, among others (Brancato & Albina, 2011; A. Sica, et al., 2008). This diverse array of functions is reflected in the activities performed by macrophages at the site of a wound. Unlike most inflammatory cells, which exhibit activities within very short time frames, macrophages are among the first inflammatory cells to arrive the site of injury, and may remain there weeks after the

injury, facilitating the fibrotic response. While the pro-healing macrophage phenotype has previously been classified with the anti-inflammatory macrophages, this subject continues to be under debate (Brancato & Albina, 2011).

TABLE 1. Selected Biomarkers of Polarization-Dependent Macrophage Activity, Gene Expression, and Cytokine Release

	M1	M2	References
IL-1	+	-	(A. Sica, et al., 2008)
IL-6	+	-	(Alberto Mantovani, Sica, & Locati, 2005)
IL-10	-	+	(Alberto Mantovani, et al., 2005; Porta et al., 2009)
IL-12	+	-	(Porta, et al., 2009)
IL-23	+	-	(Alberto Mantovani, et al., 2005)
CCL2 (MCP-1)	-	+	(Porta, et al., 2009)
CCL3 (MIP-1α)	+	-	(Gordon, 2003; A. Sica, et al., 2008)
CCL17 (TARC)	-	+	(Gordon, 2003; Porta, et al., 2009)
CCL22	-	+	(Porta, et al., 2009)
CXCL9	+	-	(Martinez, Gordon, Locati, & Mantovani, 2006)
CXCL10	+	-	(Martinez, et al., 2006)
CXCL11	+	-	(Martinez, et al., 2006)
MMP-1 / MMP-9	-	+	(Gordon, 2003)
Scavenger receptor (CD204)	-	+	(A. Sica, et al., 2008)
Mannose Receptor (CD206)	-	+	(A. Sica, et al., 2008)
TNF-α	+	-	(Porta, et al., 2009)
Arginase I	-	+	(Porta, et al., 2009)
iNOS (NOS2) / ROS Products	+	-	(A. Sica, et al., 2008)

+ indicates upregulated activity or gene expression relative to polarization towards the opposite phenotype.
– indicates lower or lack of activity/gene expression relative to polarization towards the opposite phenotype.

Recent work in Klaus Ley's group has also shown that monocytes differentiated in platelet factor-4 (CXCL4) become macrophages with very distinct

gene expression profiles from pro- and anti-inflammatory macrophages (Gleissner, et al., 2010). The CXCL4-differentiated macrophages expressed the same canonical macrophage markers as the M-CSF-differentiated macrophages (CD45, CD11b, CD14). However, the expression of a variety of cytokines and chemokines were vastly different from typical profiles expected with M1 and M2 macrophages. This newly identified macrophage subtype has been dubbed the "M4" macrophage, but this finding has yet to be accepted into the dogma of macrophage biology.

Macrophages as a Therapeutic Target in Cancer

Because the metastatic phase of cancer is so lethal compared to the primary tumor, focus on treatment of metastasis is paramount to the goal of eradicating deaths due to cancer. Treatment of distributed disease through the induction of an anti-tumor immune response has the potential to provide acute therapeutic effects. In addition, immune memory of the anti-tumor response may provide long-term therapy against emergent micrometastases that possess a phenotype similar to the original primary tumor. To achieve this goal, others continue to investigate cell therapies centered on tumor-associated dendritic cells, T-cells, and NK-cells. While they have received some interest, tumor-associated macrophages (TAMs) have not been investigated as heavily.

TAMs have been proposed as a potential drug target in cancer because they have been shown to support tumor growth and invasiveness through the secretion of growth and angiogenic factors, as well as MMPs and cathepsins that degrade the local extracellular matrix (A. Mantovani, et al., 2002; Miselis, et al., 2008) . Pro-

inflammatory macrophages play key roles in activating the immune response against early-stage tumors, in part by mediating immune recognition of aberrant protein expression profiles. However, the macrophage infilitrate at later-stage breast tumors mostly consists of anti-inflammatory macrophages, which suppress the anti-tumor immune response and facilitate tumor survival and growth (de Visser, Eichten, & Coussens, 2006; Dirkx, Oude Egbrink, Wagstaff, & Griffioen, 2006; Murdoch, Muthana, Coffelt, & Lewis, 2008; Pollard, 2008). This pro→anti-inflammatory transition has been implicated as a key mechanism in facilitating the metastatic progression of tumors (de Visser, et al., 2006). Recently, reversal of this transition has been achieved *in vitro* and *in vivo* in mouse models, and has triggered activation of the immune system-mediated anti-tumor cascade (Stout et al., 2005; Watkins, Egilmez, Suttles, & Stout, 2007). The activation of an anti-tumor immune response correlated with a reduction in tumor mass (Guiducci, Vicari, Sangaletti, Trinchieri, & Colombo, 2005). Clinical trials investigating the potential impact of such treatment in humans are ongoing in Taiwan and results have not yet been reported to date (ClinicalTrials.gov ID# NCT00690261).

Nevertheless, it is clear that systemic immunotherapy leads to significant off-target side effects, and intratumoral injection of cytokines—as done in the laboratory—is not always practical in the clinic. Novel, translational technologies are necessary to harness the power of immunotherapy in cancer. Nanomaterials have been known to passively accumulate in solid tumors due to the presence of leaky vasculature and poor lymphatic drainage. Further, macrophages are among the most phagocytic cells in the body. Recently, others have begun to leverage these

features to synthesize nanoparticles that localize to TAMs (Larsen et al., 2009). However, the use of this technology to modulate the polarization state of TAMs is as yet uninvestigated.

Macrophages as a Therapeutic Target in Atherosclerosis

Cardiovascular disease continues to be the leading cause of death in the United States, accounting for 1 of every 2.9 deaths (Lloyd-Jones et al., 2010). Development of atherosclerotic plaque is responsible for many of these events, and is characterized by a cascade of events including the accumulation of lipids in arterial walls, oxidation of the lipids, and recruitment of inflammatory cells into these lipid-rich regions (Insull, 2009). Under the influence of chronic lipid deposition and oxidation, inflammatory activity, and resulting abnormal blood flow and mechanical loading conditions in the region, these plaques may suddenly rupture, producing emboli that may potentially lead to a lethal acute event such as a stroke or a myocardial infarction.

Because of the intimate involvement of macrophages throughout plaque progression, atherosclerosis is commonly thought of as an inflammatory disease, and this classification continues to guide burgeoning work in this area (Libby, 2002). This is highlighted in descriptions of events that may contribute to plaque destabilization, which include: (1) active inflammatory activity, (2) thin fibrous caps and large lipid cores, (3) endothelial erosion and thrombosis, (4) fissured or ruptured caps, and (5) luminal stenosis (>90%) (Naghavi & Falk, 2010; Saam et al., 2007). Contrary to this theory, it continues to be difficult to clinically identify

'vulnerable plaques' that are most likely to rupture—as many ruptured plaques occur in otherwise asymptomatic regions, and therefore, the concept of a vulnerable plaque remains somewhat controversial.

Nevertheless, it is clear that macrophages play multiple roles in destabilizing atherosclerotic plaques, some of which are particularly important to note here. Their production of matrix metalloproteinase (MMP)-8 and -9 in response to pathological stimuli leads to degradation and destabilization of the local extracellular matrix, increasing the likelihood of plaque rupture (de Nooijer et al., 2006; Gough, Gomez, Wille, & Raines, 2006; Herman et al., 2001; Johnson, Sung, Lessner, Fini, & Galis, 2004; Sluijter et al., 2006). Moreover, macrophages are recruited to lesions and express various scavenger receptors that facilitate endocytosis of lipids and other interstitial debris. This activity eventually results in transformation of macrophages into foam cells, and contributes to the gradual expansion of the necrotic core (Pluddemann, Neyen, & Gordon, 2007).

This array of events in the plaque is explained by the co-existence of pro- and anti-inflammatory macrophages within plaque regions (Alberto Mantovani, Garlanda, & Locati, 2009). Due to the prevalence of Th1 cells in plaque development, pro-inflammatory macrophages are found in the earlier stages of plaque progression, resulting in elevated local levels of ROS, inflammatory mediators, and MMPs. Local ROS production leads to the emergence of oxidized lipoproteins such as oxLDL, which is one of the leading biomarkers of plaque progression (Tsimikas, Willerson, & Ridker, 2006). However, oxLDL also activates transcription factors

related to anti-inflammatory mediators. A number of products of anti-inflammatory macrophages have been shown to counter plaque de-stabilization and dampen inflammation. Because of this, the anti-inflammatory macrophage is the more desired phenotype in atherosclerosis. Indeed, commercially available PPAR agonists have been shown to contribute to the induction of anti-inflammatory macrophage polarization and stabilize atherosclerotic plaques, although side effects from systemic administration continue to hinder the success of this therapeutic strategy (Tabas, 2010).

Molecular Homing of Drugs & Nanoparticles to Macrophage-Specific Receptors

As one of the most phagocytic cells in the human body, macrophages are among the first cells of the innate immune system to arrive at a site of injury, but have also been observed as permanent residents in certain organs, such as in the liver and bone marrow (Bouwens, Baekeland, de Zanger, & Wisse, 1986; Felix et al., 1990; Martin, 1997). Pro-inflammatory macrophages are central to the clearance of pathogens and microbes, while anti-inflammatory macrophages aid in the removal of host cell and matrix debris that are present at an injury site. Macrophages recognize and interact with this multitude of potential targets through a variety of pattern recognition receptors, including toll-like receptors, mannose receptor (CD206) and scavenger receptor A (CD204) (Brown & Goldstein, 1983; Kindt, et al., 2007; Linehan, Martinez-Pomares, & Gordon, 2000). The polygamous nature of these pattern-recognition receptors is not restricted to endogenous ligands and targets—for example, CD204 has been shown to contribute to the uptake of

nanoparticles surface-functionalized with carboxylic acids, antibodies, as well as poly(ethylene glycol) (PEG) (Chnari, Nikitczuk, Wang, Uhrich, & Moghe, 2006; Lipinski et al., 2006). Therefore, it is not very difficult to target synthetic nanoparticles to macrophages through non-specific means. However, the rational design of macrophage receptor-targeted nanoparticles for *in vivo* use requires an application-driven minimization of such nonspecific interactions between macrophage pattern recognition receptors and the nanoparticles.

Nonspecific interactions between macrophage receptors and nanoparticles may be dictated by particle size, shape, surface charge, and hydrophobicity, and facilitated by surface chemistry-specific complement activation on the nanoparticle (Doshi & Mitragotri, 2010; Thomas et al., 2011). Doshi and Mitragotri treated macrophages at 4°C with a library of polystyrene microparticles exhibiting a variety of sizes and shapes to mimic bacterial dimensions, and observed optimal attachment for rod-shaped particles with the longest dimension at 2-3μm (Doshi & Mitragotri, 2010). Raynal et al. showed in 2004 that macrophages exhibit size-dependent uptake of nanoparticles functionalized with dextran (Raynal et al., 2004). While the findings of these two studies furthered understanding of macrophage-particle interactions, significant questions remain unanswered. The smallest particles investigated in Doshi's study were in the range of 500 nm, and have yet to be extended to the sub-100 nm dimensional range of interest in many *in vivo* applications. Raynal et al.'s study was conducted before the identification of a dextran receptor (SIGNR1/CD209b) on murine macrophages.

TABLE 2. Known biomarkers of the monocyte/macrophage lineage and known expression in other cell lines.

Biomarker	Description	Monocytes	Macrophages	Other Cells
CD11b	α_M integrin/iC3B receptor	+	+	NK, granulocytes
CD64	Fc fragment of IgG receptor (FcγR1A)	+	+	DCs
CD115	Colony stimulating factor 1 receptor / CSF1R	+	+	Osteoclasts, breast, microglia
CDw136	Macrophage-stimulating protein receptor / MST1R	–	+	Epithelial cells
CD163	Hemoglobin scavenger receptor, M130	+	+	Hematopoietic progenitors
CD204	Scavenger receptor 1	–	+	–
CD206	Mannose receptor C type 1	–	+	DCs

Information up-to-date as of June 16, 2011, based on NCBI-GENE database: http://www.ncbi.nlm.nih.gov/gene .

While a very small, baseline level of nonspecific uptake may be acceptable, the optimization of specific targeting strategies remains an area of intense activity today. A number of monocyte/macrophage-specific cell surface biomarkers have been identified for this purpose, but in most cases, have later also been discovered on other cell types (Table 2). For example, while mannose receptor/CD206 is primarily expressed in macrophages, they have also been reported on dendritic cells, and therefore, macrophage targeting approaches to this receptor may also lead to off-target effects. Studies in the 1990's discovered that the mannose receptor binds—as the name implies—mannose, as well as a few other sugars such as fucose, glucose, and *N*-acetylglucosamine, and more avidly binds oligosaccharides composed of these sugars as opposed to monosaccharides (Stahl & Ezekowitz, 1998). Espuelas et al. confirmed these findings by tethering mannose monosaccharides, disaccharides, or tetrasaccharides onto liposomes, and observed

that liposomal uptake into dendritic cells was enhanced by multivalent presentation of mannose ligands on the liposomal surface (Espuelas, Thumann, Heurtault, Schuber, & Frisch, 2008).

The macrophage scavenger receptor 1 (CD204) is one of the very few known endocytosis receptors to have not been discovered in other cell lines besides those of the monocyte/macrophage lineage. Originally discovered by Brown and Goldstein in the 1980s, CD204 enhances macrophage uptake of acetylated low-density lipoproteins and was later observed to also facilitate the endocytosis of oxidized LDLs, branched fucose polymers (e.g., fucoidan), dextran, polyanions, and even PEGylated particles (Brown & Goldstein, 1983; Chnari, et al., 2006; Raynal, et al., 2004). Optimization of specific targeting strategies to this receptor remains difficult due to its nature as a pattern recognition receptor. High-affinity ligands for CD204 are well-characterized and include fucoidan and polyinosinic acid, which have classically been used to compete away binding of modified LDLs to the receptor (Brown & Goldstein, 1983).

Intracellular delivery of drugs and nucleic acids, as proposed in this work, is likely to require molecular targeting approaches to endocytotic receptors. Therefore, CD204 and CD206 are leading molecular targets for the nanoparticles to be described here.

Candidate Target Genes for Therapeutic siRNA-Mediated Knockdown to Modulate Macrophage Polarization

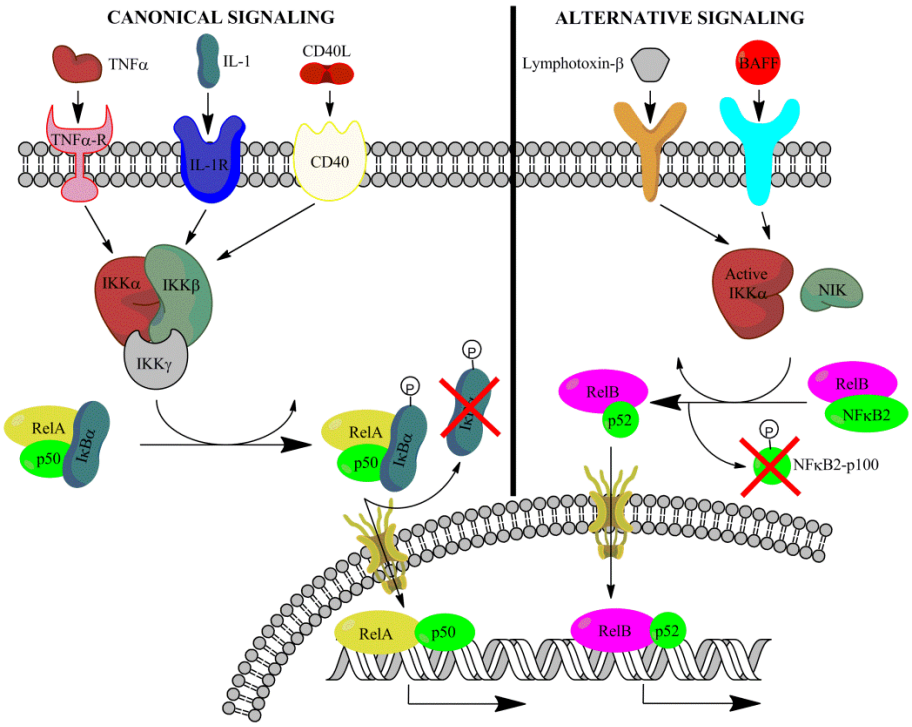

FIGURE 2. The Signaling Pathways of the NF-κB Transcription Factor Family. The NF-κB family includes the Rel proteins, NF-κB1, and NF-κB2. The canonical pathway is activated through LPS, TNFα, IL-1, or CD40L and results in the activation of the IκB kinase (IKK) complex. IκB proteins retain dimers of RelA and NF-κB1-p50 in the cytoplasm, and phosphorylation of IκB enables the dimer to translocate to the nucleus, resulting in activation of downstream genes. In the alternative pathway, LTβ or BAFF activate the IKKα subunit of IKK independently of the other IKK subunits, as well as another kinase—NIK. These two kinases act on the RelB-NF-κB2 dimer, resulting in the degradation of the NF-κB2-p100 subunit, translocation of RelB-p52 (p52 is the remaining subunit of NF-κB2) to the nucleus, and activation of downstream genes. Adapted from (Cao & Karin, 2003b).

Current understanding of the molecular mechanisms governing macrophage polarization remains hazy. However, preliminary work has identified a few pieces to the puzzle, as a number of transcription factors have been correlated with the expression of hallmark pro- and anti-inflammatory polarization markers.

Previous work suggests that the NF-kappaB (NF-κB) transcription factor in macrophages contributes to their impact during tumorigenesis (Figure 2) (de Visser, et al., 2006; Dirkx, et al., 2006; Murdoch, et al., 2008; Pollard, 2008; Stout, et al., 2005; Watkins, et al., 2007). A number of these studies have demonstrated aberrant expression of NF-κB in breast cancer cell lines and primary tumors (Cogswell, Guttridge, Funkhouser, & Baldwin, 2000; Dejardin et al., 1995; Nakshatri, Bhat-Nakshatri, Martin, Goulet, & Sledge, 1997; Sovak et al., 1997). While NF-κB activation in TAMs may elicit anti-tumor effects by polarizing these cells towards an M1 phenotype, elevated NF-κB signaling has been observed in breast cancer cells and has been shown to promote cell growth through the activation of cyclins (Cao & Karin, 2003b; Guiducci, et al., 2005; Porta, et al., 2009). Therefore, macrophage-specific modulation of NF-κB activity has potential as a novel therapeutic approach for breast cancer, including triple-negative and refractory phenotypes. NF-κB family members exist as dimers sequestered in the cytoplasm of most mammalian cells by inhibitory molecules. In the canonical NF-κB pathway, inhibitors such as IκBα are destroyed upon cell stimulation, allowing NF-κB to enter the nucleus and associate with cognate DNA binding sites, influencing gene transcription (Vallabhapurapu & Karin, 2009; Verma, Stevenson, Schwarz, Van Antwerp, & Miyamoto, 1995). Activation of NF-κB by the canonical pathway is known to be a key modulator of multiple intracellular activities and is responsible for a wide variety of consequent cellular behaviors. In the alternative NF-κB signaling pathway, interaction between p100 and RelB maintains the complex in the cytoplasm until processing of the p100 to the mature p52 form results in translocation of the complex to the nucleus

(Senftleben et al., 2001; Solan, Miyoshi, Carmona, Bren, & Paya, 2002). The alternative pathway can be activated by upstream signals that are different from those that activate the canonical pathway (Xiao, Rabson, Young, Qing, & Qu, 2006). The upstream activators specific to the alternative pathway include; receptor activator of NF-κB ligand (RANKL) (Cao et al., 2001) and tumor necrosis factor (TNF)-like weak inducer of apoptosis (TWEAK) (Saitoh et al., 2003). Cellular responses to NF-κB activation by the alternative pathway are relatively unexplored, especially for applications in cancer immunology, but are likely to have distinct functions to those of the canonical pathway (Bonizzi & Karin, 2004). Both the canonical and the alternative pathways have been implicated in oncogenesis (Cao & Karin, 2003a; Eliopoulos et al., 2003; Perkins, 2003; Romieu-Mourez et al., 2001).

Since the NF-κB signaling pathway is regulated through the balance of several inhibitor proteins, enzymes, and DNA-binding domains, there are a number of 'druggable' targets within this pathway that can be leveraged in an attempt to induce pro-inflammatory (knockdown of IκB/other inhibitors) or anti-inflammatory polarization (knockdown of IκB kinases or DNA-binding domains).

Alternatives to this NF-κB-centric siRNA targeting scheme include the STAT family of transcription factors and the suppressor of cytokine signaling (SOCS) family. Williams et al. installed a constitutively active STAT3 transcription factor into macrophages and replicated the IL-10 induced suppressed macrophage phenotype in the transfected cells (Williams et al., 2007). In converse, the siRNA-mediated silencing of STAT3 in macrophages, dendritic cells, and B-cells results in

the re-activation of an anti-tumor immune response (Kortylewski et al., 2009). Others showed that knockdown of the SOCS3 protein attenuates M1 macrophage activity and activates expression of CD206, arginase, and STAT3-related genes, indicating activation of the M2 macrophage phenotype (Liu et al., 2008). In the later parts of this work, these pathways will be considered alongside the NF-κB pathway for siRNA-mediated knockdown, with the goals of re-polarizing M1 or M2 macrophages to the opposite phenotype.

Design of Macrophage-Targeted Biomaterials

My dissertation is organized in to several manuscripts, a few of which are already published, based on the following steps as we pursued the design and validation of macrophage-targeted biomaterials: (1) Optimization of nanoparticle characteristics that would reduce non-specific recognition of the particles by macrophages that may exist outside of the desired site of intervention, (2) Optimization of nanoparticle characteristics that would increase site-specific recognition of pathologic macrophages, (3) Design of a localized delivery platform that may serve as an implantable patch for delivery of nanoparticles to a site of pathologic inflammation, and (4) Identification of potential molecular and gene pathway targets for biomaterials-mediated, therapeutic intervention *in vivo*.

CHAPTER II

SIZE- AND CHARGE-DEPENDENT NON-SPECIFIC UPTAKE OF PEGYLATED NANOPARTICLES BY MACROPHAGES

The assessment of macrophage response to nanoparticles is a central component in the evaluation of new nanoparticle designs for future *in vivo* application. This work investigates which feature, nanoparticle size or charge, is more predictive of non-specific uptake of nanoparticles by macrophages. This was investigated by synthesizing a library of polymer-coated iron oxide micelles, spanning a range from 30-100 nm in diameter and -23 mV to +9 mV, and measuring internalization into macrophages *in vitro*. Nanoparticle size and charge both contributed towards non-specific uptake, but within the ranges investigated, size appears to be a more dominant predictor of uptake. Based on these results, a protease-responsive nanoparticle was synthesized, displaying a matrix metalloproteinase-9 (MMP-9)-cleavable polymeric corona. These nanoparticles are able to respond to MMP-9 activity through the shedding of 10-20 nm of hydrodynamic diameter. This MMP-9-triggered decrease in nanoparticle size also led to up to a six-fold decrease in nanoparticle internalization by macrophages and is observable by T_2-weighted magnetic resonance imaging. These findings guide the design of imaging or therapeutic nanoparticles for *in vivo* targeting of macrophage activity in pathologic states (Yu et al., 2012). For the purposes of the dissertation, the results presented in this chapter aided in the design and selection of optimal

nanoparticle characteristics to reduce non-specific recognition of nanoparticles by macrophages.

Introduction

As one of the most phagocytic cells in the human body, macrophages are among the first cells of the innate immune system to arrive at a site of injury, but also have been observed as permanent residents in certain organs, such as in the liver and bone marrow (Bouwens, et al., 1986; Felix, et al., 1990; Martin, 1997). They function to clear pathogens and microbes, as well as host cell and matrix debris that are present at sites of tissue injury. Macrophages recognize and interact with this multitude of potential targets through a variety of mechanisms, including phagocytosis and receptor-mediated endocytosis. The latter is mediated primarily through pattern recognition receptors, which include toll-like receptors, the mannose receptor (CD206), and scavenger receptor A (CD204) (Brown & Goldstein, 1983; Kindt, et al., 2007; Linehan, et al., 2000). The polygamous nature of these pattern-recognition receptors is not restricted to natural ligands and targets. For example, CD204 has a wide range of molecular partners, leading to receptor-mediated endocytosis, distinct from the non-specific uptake due to pinocytosis (Pluddemann, et al., 2007). For the purposes of this dissertation, we have defined this polygamous behavior as 'non-specific' uptake or internalization. This is emphasized by evidence that CD204 has been shown to contribute to the non-specific uptake of nanoparticles surface-functionalized with carboxylic acids, antibodies, as well as synthetic polymers.(Chnari, et al., 2006; Lipinski, et al., 2006)

Therefore, the rational design of nanoparticles for *in vivo* use requires an application-driven minimization or optimization of such non-specific interactions between macrophages and synthetic nanoparticles. However, this area remains largely uninvestigated.

Therefore, in this work, we sought to investigate non-specific uptake of synthetic nanoparticles by macrophages, extending the work of these earlier groups into sub-100 nm PEGylated nanoparticles. To our knowledge, this is the first investigation of the effects of nanoparticle size, surface chemistry, and charge on non-specific uptake by macrophages. The rationale for using a PEG-functionalized nanoparticle system to accomplish these objectives is that macrophages are unlikely to have specific receptors for PEG. Further, PEG can be easily modified to display various chemical functionalities, enabling the modulation of nanoparticle charge without significantly varying the bulk properties of the PEG coating. This is also a relevant model system for study because PEGylation of nanoparticles is commonly performed in order to render synthetic nanoparticles water-soluble and applicable for *in vivo* use. This is, in part, because PEG has been shown to discourage protein adsorption and opsonization on nanomaterial surfaces (Ratner, 1996).

Therefore, we used block copolymers of poly(ethylene glycol)-bl-poly(propylene sulfide) (PEG-PPS), which are amphiphilic copolymers that are capable of forming micelles and stabilizing hydrophobic drugs and nanoparticles at their liquid, PPS core (Velluto, Demurtas, & Hubbell, 2008; S. S. Yu, R. L. Scherer, et al., 2011). The incorporation of ultrasmall superparamagnetic iron oxides (USPIOs) into the micellar core of PEG-PPS block copolymers serves two functional

purposes—enabling easy quantification of particle uptake through colorimetric assays, while also being a widely investigated contrast agent for T_2-weighted magnetic resonance imaging (MRI). Through the use of a variety of materials processing techniques to form the micelles, including thin film hydration and direct hydration, the same starting PEG-PPS copolymers and iron oxide cores can lead to monodisperse micelles (PEG-PPS-USPIOs) exhibiting hydrodynamic diameters at 30, 40, or 100 nm. Additionally, PEG-PPS-USPIOs can be fashioned with different surface chemistries at the PEG terminus, enabling an examination of charge-dependent non-specific uptake of nanoparticles by the macrophages.

To demonstrate the utility of these studies, we evaluated a protease-activity MRI probe design against these results. To make activity probes, PEG chains containing a protease-cleavable peptide substrate were synthesized and conjugated to PPS, in order to fashion surfactants for the micellization of USPIOs. The resulting nanoparticles that are 'activatable' by protease activity through a ≥10 nm decrease in hydrodynamic diameter. Macrophages are therefore expected to internalize protease-treated nanoparticles differently than untreated nanoparticles. We hypothesize these differences can be visualized via MRI with the aid of the contrast agent USPIOs encapsulated within the micelles. Taken together, the work presented here shows methods to design ideal nanoparticle dimensions and properties in order to better optimize nanoparticle behavior *in vivo*.

Materials and Methods

All reagents were purchased from Sigma-Aldrich (St. Louis, MO) and used as purchased unless otherwise noted below. MMP-9, MMP-9 inhibitor, Fmoc-protected L-amino acids, and resins for solid-phase peptide synthesis were purchased from EMD Biosciences (Gibbstown, NJ). PEG reagents were purchased from Laysan Biosciences (Arab, AL). All dialysis supplies were ordered from Pierce Scientific (Rockford, IL) and used with modifications to the factory-provided protocol as indicated in the appropriate sections below. Copper TEM grids with Formvar film and uranyl acetate were purchased from Electron Microscopy Sciences (Hatfield, PA). RPMI-1640 medium, penicillin-streptomycin, and fetal bovine serum (FBS) were purchased from Invitrogen (Carlsbad, CA).

PEG-PPS Block Copolymers and Functionalization

Synthesis of ~7kDa carboxy-PEG-PPS (cPEG-PPS) was carried out as previously described (S. S. Yu, R. L. Scherer, et al., 2011). For fluorescent polymers, FITC-PEG-NH_2 was used in place of cPEG-NH_2 in the coupling reaction to PPS. The MMP-9-cleavable peptide GGPRQITAGC (M9C; Gly-Gly-Pro-Arg-Gln-Ile-Thr-Ala-Gly-Cys)(Deguchi et al., 2006) was synthesized on a Rink-amide MBHA resin support, via standard Fmoc-based solid phase peptide synthesis on an automated system (Protein Technologies PS3, Tucson, AZ) (Chan & White, 2000). The peptide (1.5eq, 45mmol) was then reacted overnight with 1eq of 5kDa methoxy-PEG-maleimide (mPEG-MAL; 30 mmol; 150 mg), in an aqueous buffer containing 0.1M Na_3PO_4 and 0.15 M NaCl at pH 7.2. Unbound peptide was removed by dialysis across a 2 kDa

molecular weight cutoff membrane overnight at room temperature. The completed mPEG-[M9C] conjugate was lyophilized, then coupled to cPEG-PPS via standard carbodiimide chemistry to yield mPEG-[M9C]-PEG-PPS block copolymers.

For FT-IR spectroscopy, polymer samples were prepared by mixing with IR-grade KBr and pelleting on a KBr press (Specac, Slough, United Kingdom). FT-IR was performed on a Bruker Tensor 27 system (Billerica, MA).

^{1}H NMR spectra were obtained at 400 MHz using a 9.4 T Oxford magnet operated by a Bruker AV-400 console. The main NMR probe for the instrument is a 5 mm Z-gradient broadband inverse (BBI) probe with automatic tuning and matching capability (ATM).

Gel permeation chromatography (GPC) was performed on three resolving columns running in series (Tosoh Biosciences 1x TSKGel Alpha4000, 2x TSKGel Alpha3000; King of Prussia, PA) with DMF + 0.1 M LiBr mobile phase. Columns were incubated at 60°C, and chromatograms were obtained with a Shimadzu SPD-10A UV detector and RID-10A refractive index detector (Shimadzu Scientific Instruments, Columbia, MD), and a Wyatt miniDAWN Treos multi-angle light scattering detector (MALS; Wyatt Technology, Santa Barbara, CA). Data collection and analysis was achieved through the Wyatt ASTRA software (version 5.3.4).

Encapsulation of Ultrasmall Superparamagnetic Iron Oxides (USPIOs) in PEG-PPS Copolymers

Synthesis of hydrophobic, monodisperse USPIO core particles and their encapsulation in PEG-PPS copolymers was carried out as previously described (S. S. Yu, R. L. Scherer, et al., 2011). In brief, USPIO cores of predictable diameters were first synthesized through thermal decomposition, by controlling the molar ratios of iron precursor to oleic acid introduced in the reaction feed (Figure 3). A 1:2 mass ratio of dried hydrophobic USPIO cores to PEG-PPS polymers were then dissolved in toluene, vortexed to mix, sonicated for 5 s to break apart clumps, and then dried by rotary evaporation for 20 min. The dried polymer/USPIO mixture was then rehydrated in 3 mL of nanopure water and vortexed vigorously to suspend all particulates. Large clumps and byproducts were removed by magnetic pelleting, and the colloidal phase was collected and further centrifuged at 2500 × g for 5 min to precipitate excess polymers. The supernatant is gently aspirated by pipette into fresh scintillation vials and stored at 4°C.

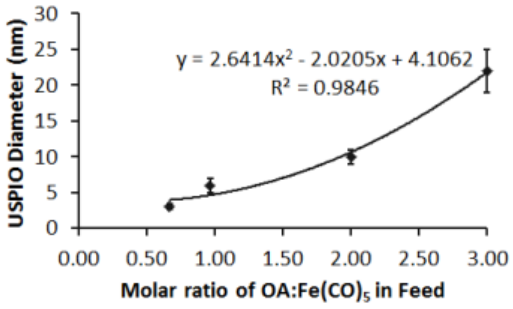

FIGURE 3. Tuning USPIO diameters by varying surfactant to precursor feed ratios. Feed ratio of oleic acid surfactant to iron pentacarbonyl precursors and resulting USPIO diameters. 6 mmol of $Fe(CO)_5$ was introduced into reactors containing 40 mL octyl ether and varying amounts of oleic acid at 100°C. USPIO cores were allowed to grow and then oxidize as described above, and then imaged by HRTEM. Core diameters were measured via ImageJ software.

To fabricate fluorescent micelles, a 1:40:20.5 mass ratio of FITC-PEG-PPS : PEG-PPS : iron oxide cores was mixed and micellized as described above. Therefore, the overall mass ratio of polymers to iron oxides is preserved at 1:2 for all micellization procedures. To make "proximity-activated" USPIOs (PA-USPIOs)—which are able to respond to local MMP-9 activity, OA-USPIOs were encapsulated in MMP-9-cleavable mPEG-[M9C]-PEG-PPS polymers using the same protocol.

Pluronic-PPS Nanoparticles and Loading with USPIOs

Pluronic-stabilized PPS NPs were synthesized by inverse emulsion polymerization as described previously (Rehor, Hubbell, & Tirelli, 2005; Thomas, et al., 2011). Pluronic F-127 (a block copolymer of polyethylene glycol and polypropylene glycol terminated by α and ω hydroxyl groups) was used alone or in combination with carboxyl-terminated Pluronic derivatized as previously described (van der Vlies, O'Neil, Hasegawa, Hammond, & Hubbell, 2010). The hydrophobic core was stabilized by di-sulfide crosslinking of the linear PPS chains (Rehor, et al., 2005). However, since crosslinking cannot reach completion, remaining free sulfhydryl groups on the NP surface were irreversibly capped by reaction with the alkylating reagent iodoacetamide. NP solutions were sterile-filtered, and then loaded with 3 nm USPIO cores through a direct hydration process. 100μL of the hydrophobic OA-USPIOs (20 mg/mL in THF) was added to 1mL of the Pluronic-PPS NPs (15 mg/mL in water) with swirling, and was followed by removal of THF by rotary evaporation, and removal of non-encapsulated OA-USPIOs by filtration through 0.45 μm Teflon filters (Whatman Inc., Piscataway, NJ).

Nanoparticle Characterization

Size and ζ-potential of NPs were investigated by dynamic light scattering (DLS) in a Malvern Zetasizer Nano-ZS with the reusable dip-cell kit (Malvern Instruments Ltd., Worcestershire, U.K.). For measurements of ζ-potential in serum media, nanoparticles were mixed with THP-1 growth medium and allowed to incubate at 37°C for 24 h prior to DLS measurements. No further purification of the nanoparticles was performed. This is because the purification process ends up diluting the particles (along with the adsorbed proteins), and may lead to further protein exchange interactions with media used downstream of isolation procedures, as per the Vroman effect (Ratner, 1996). Therefore, in order to best mimic *in vivo* conditions, the nanoparticles were measured in the presence of serum. Measurements of hydrodynamic diameter demonstrated the presence of a peak at < 5 nm that corresponded to proteins, while nanoparticles could still be easily discerned within the 20-100 nm diameter range.

Transmission electron microscopy (TEM) was conducted on a Philips CM20 system operating at 200 kV. Carbon film-backed copper grids were inverted onto droplets containing nanoparticle suspensions of interest and blotted dry. Images were collected using a CCD camera with AMT Image Capture Engine software (Advanced Microscopy Techniques, Danvers, MA), and sizing of the particles was automated using a particle analyzer on ImageJ software. Images were thresholded, and then the built-in Analyze Particles function was used to measure the major and minor axes of the fit ellipses around each particle. After artificially discarding clumps of particles encompassed within single fit ellipses (usually identified by

major and minor axes that were >10% different from one another), or ellipses drawn around globs in the carbon grid (usually identified by any dimension < 1 nm), the diameter of individual particles was taken to be the average of the major and minor axis.

For aqueous samples, nanoparticles on TEM grids were also counterstained with 3% uranyl acetate in water for 2 min, gently blotted dry, and dried in a vacuum desiccator for 2 h prior to imaging.

Cell Culture and Nanoparticle Co-incubation Experiments

Non-adherent THP-1 human leukemic monocytes (American Type Culture Collection, Manassas, VA) were grown in RPMI-1640 medium supplemented with 10% FBS, 1% penicillin-streptomycin, 1X MEM vitamins (Mediatech, Manassas, VA), 120 μM β-mercaptoethanol, and 10mM HEPES at 37°C in a 5% CO_2 incubator. For all cell experiments, monocytes were seeded into standard tissue culture-treated plates at a density of 300,000 cells/cm^2, and differentiated for 3 days in growth medium (above) supplemented with 200 nM of phorbol myristate acetate (PMA). The differentiation process leads to induction of cell adherence onto tissue culture polystyrene surfaces.

For nanoparticle co-incubation experiments, cells were washed 1x with PBS to remove unbound cells, prior to addition of growth medium. The medium was supplemented with nanoparticles and fucoidan. Nanoparticle dosing was based on

total iron concentration as measured through the colorimetric phenanthroline assay as previously described (Christian, 1994). Final iron concentrations in the wells were calculated to be between 30-200μM. For fucoidan competition experiments, media was supplemented with fucoidan to a final concentration of 0-500 μM.

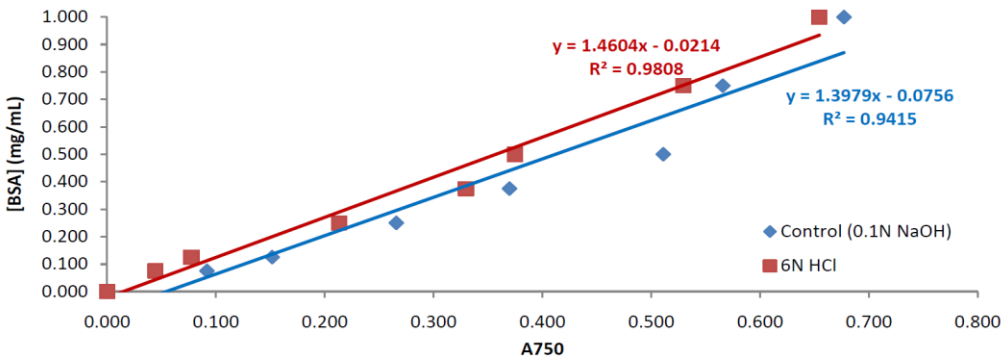

FIGURE 4. Lowry protein assay standard curves. Bovine serum albumin (BSA) was dissolved in PBS and treated with either 0.1 N NaOH or 6N HCl prior to performance of the Lowry protein assay. While the assay is typically run under alkaline conditions (blue), strong acidic conditions do not significantly affect the sensitivity or reliability of this assay.

At selected time points, cells were washed 3X with PBS to remove unbound nanoparticles, and then lysed in 3N HCl and 0.25% Triton X-100 for at least 2 h. The strongly acidic environment also promotes solubilization of the endocytosed USPIOs via oxidation of the amphiphilic PEG-PPS shell on the nanoparticles into fully hydrophilic polymers (Rehor, et al., 2005), as well as leaching and mineralization of the iron in the USPIO core. The cell lysate was analyzed for protein content using a commercial Lowry protein assay kit (Bio-Rad Laboratories, Hercules, CA), while iron content was measured using the colorimetric phenanthroline assay as previously described (Christian, 1994). While the acidic conditions for the Lowry protein assay

deviate significantly from the protocol described by the supplier (alkaline conditions), this does not significantly affect the sensitivity or results of the assay (Figure 4).

TABLE 3. Quantification of nanoparticle uptake into THP-1 cells

Nanoparticle Type	Required Measurements	Units	Equation	Rationale
PEG-PPS-USPIOs	[Fe] and [Protein] in cell lysates	μg Fe / mg protein	$\frac{[Fe]}{[Protein]}$	Result is a quantity normalized to cell number, but reflects dose-dependence and cell number-dependence of quantified internalization.
Pluronic-PPS-USPIOs	[Fe] and [Protein] in cell lysates, and $[Fe]_0$ (concentration of iron administered at time 0)	% / mg protein	$\frac{\left(\frac{[Fe]}{[Fe]_0}\right) \times 100}{[Protein]}$	Different surface chemistries led to differing loading efficiencies of Pluronic-PPS nanoparticles with USPIOs. Quantification method enables experiments to be run at constant nanoparticle concentrations, without worry of effects of different loading efficiencies on measured iron internalization.

Calculation of nanoparticle internalization was dependent upon nanoparticle type, as shown in Table 3. The rationale behind the two different measurement types is inherent to the loading efficiencies possible. Because PEG-PPS-USPIO samples are purified, all cell-nanoparticle interactions in experiments involving them involve an iron 'tag'. However, since Pluronic-PPS-USPIOs are a subpopulation of the nanoparticles used in this system, not all cell-nanoparticle interactions here

involve the iron 'tag'. Due to differing USPIO loading efficiencies across the different Pluronic-PPS surface chemistries available to us, an additional normalization method was required in order that resulting figures fully represented charge-dependent uptake of nanoparticles. The normalization of internalization data to the initially administered dose of iron was therefore used to report internalization of Pluronic-PPS-USPIOs (Table 3).

For cell viability experiments, cells were incubated for 24 h with PEG-PPS-USPIOs, at a final iron dose of 30, 60, or 120 μM. After rinsing cells 3x with PBS to remove unbound nanoparticles, they were stained with a commercial calcein-AM/ethidium homodimer live-dead assay kit (Invitrogen, Carlsbad, CA), and quantified according to the manufacturer's instructions.

Protease-Activatable Nanoparticles

"Proximity-activated" USPIOs (PA-USPIOs)—which are able to respond to local MMP-9 activity, were formed as described for other PEG-PPS-USPIOs above. For protease experiments, 50 μL PA-USPIOs (Iron dose = 600 μM) were incubated with 10 μL MMP-9 (final concentration = 2 μg/mL) in an aqueous buffer containing 0.1 M HEPES, 0.15 M NaCl, and 5 mM $CaCl_2$ (pH 7.2) for 24 h at 37°C. For control experiments, PA-USPIOs were incubated with buffer only. Following cleavage, nanoparticles were added directly to cell cultures. The final concentration of iron and MMP-9 in the cell cultures is 120 μM and 400 ng/mL, respectively. In some

control experiments, MMP-9 inhibitor was also added to the cell cultures, to a final concentration of 300 ng/mL.

Magnetic Resonance Imaging (MRI)

MRI was performed on a Varian 4.7 T horizontal bore imaging system. T_2 signal decay was measured using a Carr-Purcell-Meiboom-Gill (CPMG) spin-echo pulse sequence with N = 8 echoes with 6.5 millisecond echo spacing. The signal from each voxel at the 8 imaging time points was fit to a mono-exponential signal decay model to determine T_2 for each voxel:

$$S = S_0 e^{-\frac{t}{T_2}} \quad [1]$$

A region of interest (ROI) was manually drawn using MATLAB (MathWorks, Inc, Natick, MA) for the first imaging time point and translated to the images from later echoes. The mean T_2 and standard deviation for each well was then calculated from all voxels within this ROI. Other imaging parameters included TR = 2 seconds, field of view = 22 mm x 22 mm, data matrix = 128 x 128, slice thickness = 1 mm, number of acquisitions = 24 (total scan time ~ 1 h 45 m).

To prepare cells for MRI, the supernatant containing unbound nanoparticles in medium was aspirated and replaced with PBS, prior to scraping of the cells into the buffer (Corning Life Sciences, Lowell, MA). Cells were centrifuged into a pellet at 300 x g for 5 min, and rinsed with PBS twice more. Cells were then fixed with 10%

buffered formalin, gently mixed, and allowed to incubate for 30 min at room temperature before they were pelleted and imaged.

Results and Discussion

The primary objective of this study was to investigate size- and charge-dependent non-specific uptake of nanoparticles by macrophages. With the targeted size range being in the sub-100 nm hydrodynamic diameter range, the objectives required the synthesis of a library of highly monodisperse, water-soluble nanoparticles in order to reduce size overlap between different nanoparticle formulations and elucidate trends between size and uptake. Therefore, USPIO cores were synthesized by thermal decomposition in organic solvents, which led to oleic acid-stabilized USPIOs (OA-USPIOs) of 3.0 ± 0.4 nm (Figure 5A, $n \sim 200$) and 12.0 ± 1.0 nm (Figure 5B, $n > 400$). Control over USPIO core diameters was accomplished by adjusting the molar ratios of oleic acid surfactant to iron pentacarbonyl precursor in the reaction feed, and to date, we have synthesized OA-USPIOs of up to 24 nm in diameter using this method (Figure 3). These results extend previous work by Woo et al. (Woo et al., 2004), who showed the ability to synthesize particles from 5 – 19 nm in diameter using this same exact method. Additionally, we were also able to scale up this original synthesis and now are able to produce the uniform OA-USPIOs in 1-gram amounts.

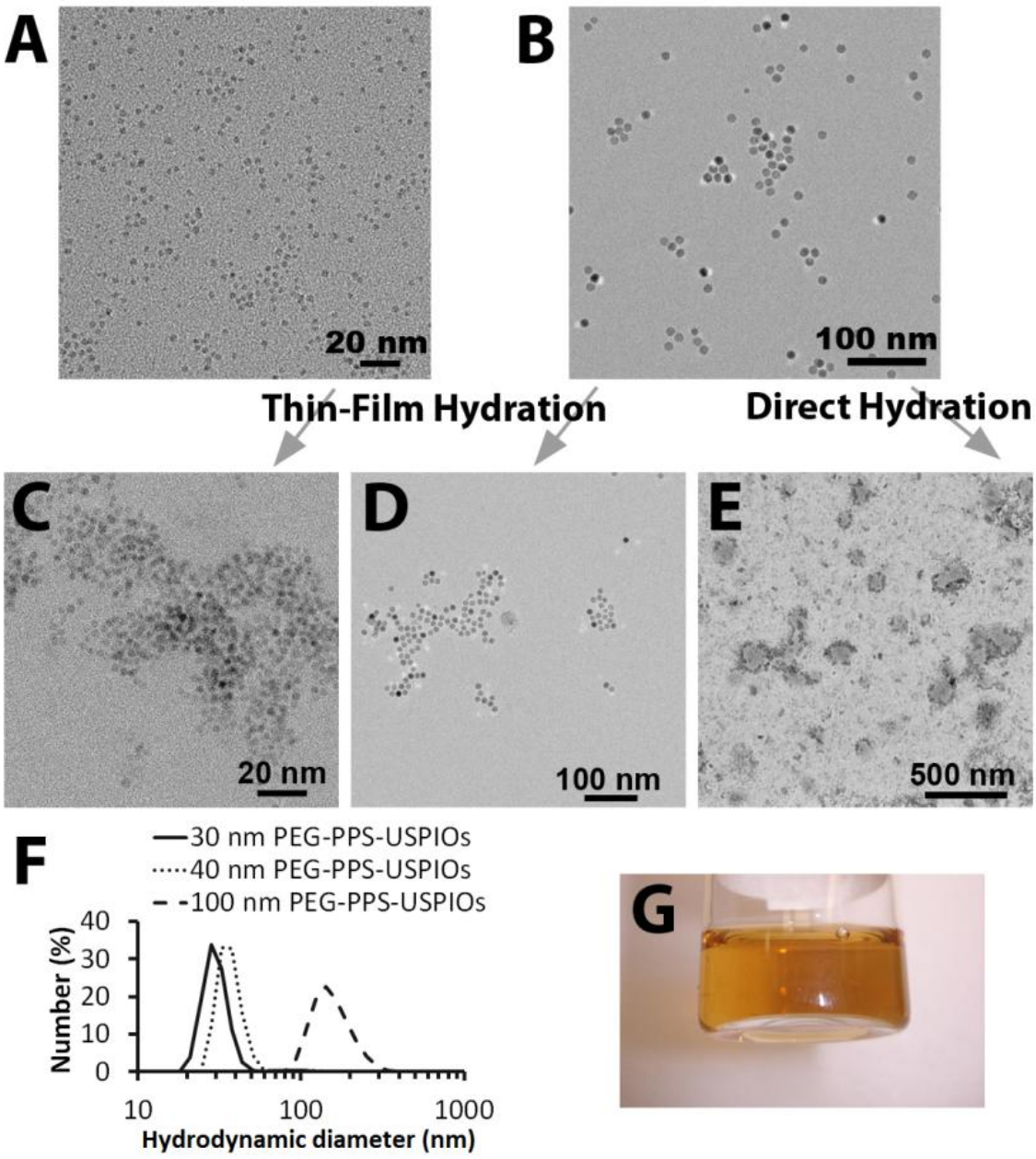

FIGURE 5. Characterization of USPIOs and PEG-PPS-USPIO micelles. HRTEM images of (A) 3 nm and (B) 12 nm hydrophobic, oleic acid-stabilized USPIO cores (γ-Fe_2O_3), which were synthesized via thermal decomposition. To render particles water-soluble, they were coated with PEG-PPS block copolymers via thin-film hydration to yield, respectively, (C) 30 nm and (D) 40 nm PEG-PPS-USPIO micelles. (E) 100 nm PEG-PPS-USPIO micelles can also be synthesized via direct hydration using the same feed materials used to create micelles in (D); this TEM image has been counterstained with 3% uranyl acetate. (F) Size-number distributions of these PEG-PPS-USPIO micelles were obtained by dynamic light scattering. (G) As shown in this representative photograph, 40 nm PEG-PPS-USPIOs remain stable in water and do not flocculate even after storage at room temperature over four months. Scale bars = (A,C) 20 nm; (B.D) 100 nm; (E) 500 nm.

To render the OA-USPIOs water-soluble, either a thin-film hydration or a direct hydration method was employed, effectively encapsulating OA-USPIOs within micelles composed of amphiphilic PEG-PPS block copolymers (1.65 kDa PPS block, 4.2 kDa PEG block; Figure 5C-E). Prior to cell experiments, the micelles were sterile-filtered; size-number distributions of the completed USPIO-loaded micelles are shown in Figure 5F. However, due to the larger size of the 100 nm micelles, these materials tended to be caught in the Teflon filters and were thus used as synthesized. The 30 nm and 40 nm micelles were particularly stable in water and flocculated minimally even after storage for several months at room temperature (Figure 5G). These two formulations were also extremely difficult to pellet by centrifugation or through the influence of an externally-applied 1 T neodymium magnet. The completed micelles exhibited ζ-potentials that were weakly anionic (Table 4), owing partly to the terminal mono-methyl ether group on the PEG block that is displayed on the nanoparticle surface.

TABLE 4. Size and ζ-potential of as-synthesized PEG-PPS-USPIO micelles

Sample Name	USPIO Core Diameter (nm)	Micelle Diameter Range (nm) [a]	ζ-Potential (mV)
30nm PEG-PPS-USPIOs	3	30.0 ± 2.6	-2.8 ± 5.9
40nm PEG-PPS-USPIOs	12	36.6 ± 11.9	-1.7 ± 4.6
100nm PEG-PPS-USPIOs	12		-7.8 ± 5.1

[a] Determined after filtration through a 0.45μm PTFE filter. 100 nm PEG-PPS-USPIOs were not as stable to filtration and were not subjected to this additional treatment step prior to use in cell experiments.

Nanoparticles were next administered to THP-1 human leukemic macrophages in order to establish a quantitative basis for the remainder of the experiments, while also examining the kinetics of particle uptake. THP-1 cells were

chosen for this study because uptake and processing of lipid nanoparticles by THP-1 and primary human monocyte-derived macrophages is not significantly different between the two cell types (Griffin, Ullery, Cox, & Jerome, 2005; Jerome, Cox, Griffin, & Ullery, 2008). We expected, therefore, that macrophage interactions with synthetic nanoparticles can be similarly modeled through this readily available, *in vitro* system.

As an example, varying doses of the 100 nm PEG-PPS-USPIOs were administered to THP-1 macrophages. Because first-order rate equations are often used as governing equations in efforts to model receptor-mediated endocytosis of nanoparticles by macrophages (Ece Gamsiz, Shah, Devalapally, Amiji, & Carrier, 2008), the resulting 24 h uptake profiles (Figure 6A) were fit to first-order rate kinetic equations (Figure 6A-B). The successful curve-fit suggested that USPIO concentration is the primary determinant of uptake rate. The best-fit equations take the form:

$$[2] \qquad [C] = [C]_{max}(1 - e^{-kt}) \qquad [2]$$

where $[C]_{max}$ represents the maximum possible concentration of iron in the cells and $[C]$ is a measure of the accumulated iron content in the cells. As the fit equations show (Figure 6A), the calculated $[C]_{max}$ values are proportional to the initially administered doses of PEG-PPS-USPIOs (standard errors < 13%), while the calculated rate constants k do not vary significantly across the doses (standard errors 25-40%). Relative to the initial doses of USPIOs, macrophages receiving 30, 60, and 120 μM of iron endocytosed 8.4 ± 3.7%, 7.7 ± 3.2%, and 6.2 ± 0.9% of the

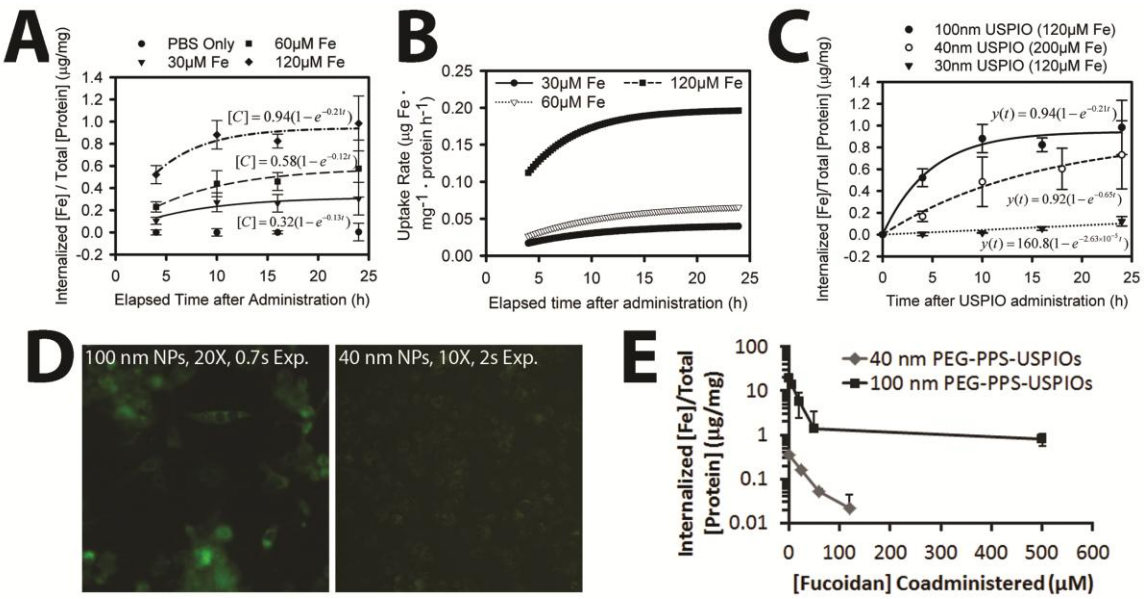

FIGURE 6. Dose- and size-dependent internalization of PEG-PPS-USPIOs by THP-1 macrophages. THP-1 cells were treated for up to 24 h with standard growth serum medium supplemented with varying doses of PEG-PPS-USPIOs in PBS. As a negative control, PBS was used in place of the PEG-PPS-USPIO colloidal suspension. Iron internalization and initial doses were quantified using a colorimetric phenanthroline assay, and internalized iron content was normalized to cell number indirectly via a protein assay. (A) Internalization of nanoparticles over the time period of interest is described by first-order rate kinetics, indicating that initial dose of nanoparticles is the primary determinant of internalization rate and total internalization amount. Relative to the initial doses of USPIOs, macrophages receiving 30, 60, and 120 μM of iron endocytosed 8.4 ± 3.7 %, 7.7 ± 3.2 %, and 6.2 ± 0.9 % of the maximum possible USPIOs, respectively. Error bars indicate standard deviations from 6 independent experiments. (B) Derivatives of the best-fit kinetic equations plotted in (A) demonstrate further the dependence of uptake rate on initial dose of PEG-PPS-USPIOs. (C) Of the three sizes investigated, 100 nm nanoparticles were most effectively internalized by the macrophages. Smaller nanoparticles were internalized less effectively, and 30 nm nanoparticles experienced almost negligible uptake levels over the 24 h experimental period. Normalization of the 24 h uptake amounts to the initially administered doses shows that macrophages internalized 6.2 ± 0.9 %, 1.4 ± 2.3 %, and 1.1 ± 0.3 % of the 100 nm, 40 nm, and 30 nm PEG-PPS-USPIOs, respectively. Error bars represent standard deviation from 3-6 independent experiments. (D) Fluorescent imaging of the delivery of 40 nm and 100 nm fluorescent PEG-PPS-USPIO micelles. The uptake of 100 nm nanoparticles was easily visualized at 20X magnification with a 0.7 s exposure time, but even with a lower magnification and roughly a threefold higher exposure time, the microscope was insufficiently sensitive to visualize the internalization of the 40 nm nanoparticles. (E) 40 nm PA-USPIOs (at 200 μM Fe) or 100 nm PEG-PPS-USPIOs (at 120 μM Fe) were co-administered to THP-1 macrophages with varying amounts of fucoidan for 24 h, and allowed to incubate overnight prior to cell lysis and measurement of internalized iron. Increasing concentrations of fucoidan correlated with decreased uptake of the nanoparticles, suggesting that the mechanism of PEG-PPS-USPIO uptake is via receptor-mediated endocytosis, and facilitated by the scavenger receptor CD204. Error bars represent standard deviation of three independent experiments.

maximum possible USPIOs, respectively. In order to ensure that the measurements excluded USPIO binding events not resulting in uptake, some experiments were also conducted at 4°C to block endocytosis, resulting in insignificant iron levels quantified in the lysates (Figure 7). In addition, a live-dead cytotoxicity assay was also conducted in order to confirm that treatment of macrophages with the PEG-PPS-USPIOs resulted in minimal cell death (Figure 8).

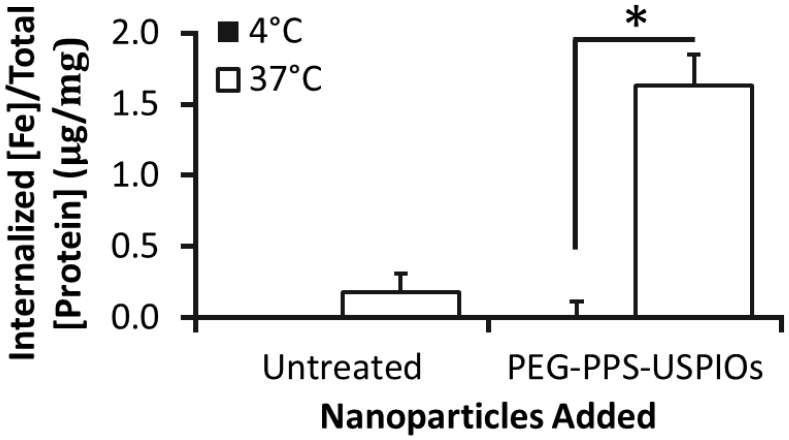

FIGURE 7. 24 h uptake of nanoparticles by THP-1 macrophages. Cells were treated with 40 nm PEG-PPS-USPIOs for 24 h, and then measured for iron content via the phenanthroline assay. Iron content was normalized to cell number indirectly via a protein assay. To confirm that the phenanthroline assay measures internalized nanoparticles and not just nanoparticles that have bound to macrophage receptors, some cells were incubated with nanoparticles at 4°C. Results showed about 10-fold lower iron content in these samples relative to samples treated at 37°C, indicating that the protocol successfully lyses cells and enables measurements of internalized iron. Error bars indicate standard deviation of 3 independent experiments (*$p < 0.01$).

Similar nanoparticle uptake kinetics were also observed for particles of smaller hydrodynamic diameters (Figure 6C). The results also show that by mass, smaller nanoparticles are internalized less effectively than their larger counterparts. The 40 nm nanoparticles shown in this graph were based on a higher iron dose for

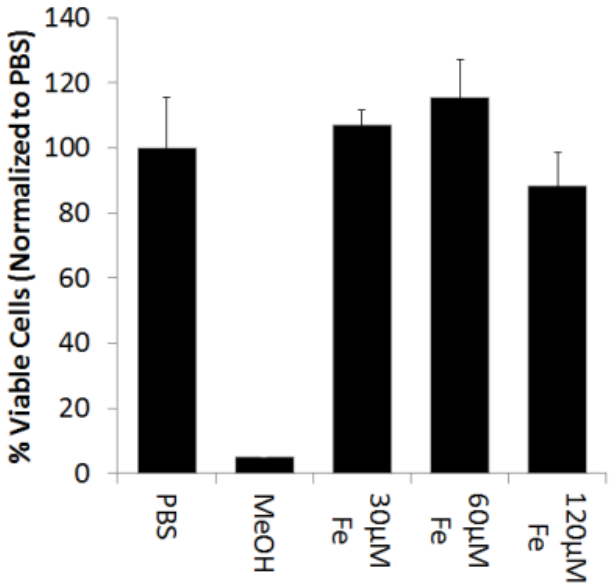

FIGURE 8. Cell viability measurements on nanoparticle-treated THP-1 cells. All measurements have been normalized to untreated cells (media + PBS). Cells were treated with increasing doses of 100 nm PEG-PPS-USPIOs for 24 h, prior to removal of unbound nanoparticles and assessment of cell viability via quantification of calcein-AM/ethidium homodimer staining. Dosage on the x-axis represents actual iron concentration within the samples. No statistically significant differences in viability were observed between any of the treatment groups (n = 3).

easier visualization; however, the same nanoparticles, administered at the same 120 μM Fe dose as the other two samples, were internalized at 0.36 ± 0.55 μg/mg protein (curve not shown). Normalization of the 24 h uptake data to the initially administered doses shows that THP-1 macrophages were able to internalize 1.1 ± 0.3 %, 1.4 ± 2.3 %, and 6.2 ± 0.9 % of the 30 nm, 40 nm, and 100 nm PEG-PPS-USPIOs, respectively. When nanoparticle internalization is normalized to cell number, a 70% decrease in PEG-PPS-USPIO diameter corresponded with almost a 10-fold decrease in iron uptake per cell. This was supported by fluorescence microscopy experiments, where macrophages were treated with FITC-tagged nanoparticles (Figure 6D), demonstrating the accumulation of 100 nm micelles

within the macrophages. Despite longer exposure times at a lower magnification, the microscope was insufficiently sensitive to visualize the internalization of the 40 nm micelles by the macrophages. Taken together, these data suggest a positive correlation between nanoparticle size and their non-specific recognition and internalization by macrophages.

Given the lack of any specific targeting moieties on the micelle surface, this evidence suggested that within the nanoparticle size range investigated, macrophages were able to optimally recognize and internalize PEGylated nanoparticles of > 100 nm diameter. Further, smaller nanoparticles seemed to experience significantly less non-specific uptake by the macrophages. One of the mechanisms of uptake is likely through receptor-mediated endocytosis via CD204—as PEG-PPS-USPIO internalization can be effectively blocked by co-administration of nanoparticles with fucoidan, which is a well-known CD204 ligand (Figure 6E) (Brown & Goldstein, 1983).

We next investigated the effects of nanoparticle charge on non-specific uptake. Because the sub-40 nm nanoparticles provided a satisfactorily minimal baseline uptake over 24 h, we opted to focus on nanoparticles of this size for this section of the study. End-carboxylated, -aminated, or -thiolated Pluronic were used as surfactants in inverse emulsion polymerization as described previously (Thomas, et al., 2011). The resulting Pluronic-PPS nanoparticles were loaded with USPIOs via direct hydration (Figure 9A-C), and delivered to THP-1 macrophages under the same conditions described for the other cell experiments above. Since Pluronic

polymers are PEG-containing block co-polymers, the properties of Pluronic-PPS are not very different from those of PEG-PPS used in the other studies shown here, and, in effect, still produce PEG-PPS-coated USPIOs. Pluronic-PPS enables facile synthesis schemes necessary to produce the various end-functionalized polymers used in this work that would be difficult to generate from PEG-PPS coatings (Rehor, et al., 2005).

In order to account for differences in USPIO loading efficiencies across the library of Pluronic-PPS nanoparticle formulations, uptake was not only reported as [Fe]/[Protein] as above, but further normalized to initial doses of iron and reported as % injected dose/protein (%ID/mg protein; Figure 9D). We hypothesized that this system would enable us to parse out the roles of surface charge from size on nanoparticle internalization, leading us to identify the sensitivity of size and charge on nanoparticle non-specific uptake by macrophages.

The Pluronic-PPS-USPIOs initially exhibited surface charges from -23 mV up to +9 mV, but following incubation in 10% serum media for 4 h, all nanoparticle formulations experienced significant changes in zeta potential (Figure 9D). Therefore, while the zeta potential of the nanoparticles was tunable to some extent by varying the surface chemistry of the nanoparticles, electrostatic interactions with serum proteins and components, as well as protein adsorption and opsonization processes contributed to significant changes in nanoparticle properties. The addition of serum into the incubation medium for these studies is intended to reflect an interaction environment that includes important components of the *in vivo* environment. Since there is no opportunity for nanoparticle purification following

intravenous injection, we elected to allow nanoparticle interaction with serum proteins during zeta potential measurements, and later on, incubation with THP-1 cells. One outcome of this approach, and equally true *in vivo*, is the modulation of initial nanoparticle zeta potential by serum protein adsorption. These processes have been studied in detail for the Pluronic-PPS nanoparticle system, as reported by Thomas et al (Thomas, et al., 2011). In particular, varying the surface chemistry of this nanoparticle system influenced the ability of the nanoparticles to become functionalized with the C3 complement proteins (Thomas, et al., 2011). More generally, this phenomena is well known in the synthetic gene delivery field, in which cationic nanoscale carriers of pDNA or siRNA rapidly interact with albumin and other serum proteins *in vivo*, and is consistent with the findings reported here (Phillips & Heydari, 1996). This is significant because many consider that a minimum zeta potential of ±30mV is necessary in order to form stable nanoparticle suspensions (Han, Li, Yin, Liu, & Xu, 2008). Because electrostatic interactions and adsorption processes between serum proteins and the nanoparticle surface are inevitable following *in vivo* administration, higher zeta potential magnitudes may actually promote these processes, and in turn, opsonization processes ultimately leading to nanoparticle clearance from the bloodstream.

The observed decrease in the magnitude of the nanoparticle zeta potentials did not correspond with increased agglomeration, as no flocculation or sedimentation was observed in any of the samples following treatment with serum. This observation was true of all nanoparticle formulations regardless of surface

chemistry, possibly owing to the colloidal stability of Pluronic-PPS nanoparticles as shown previously (Rehor, et al., 2005).

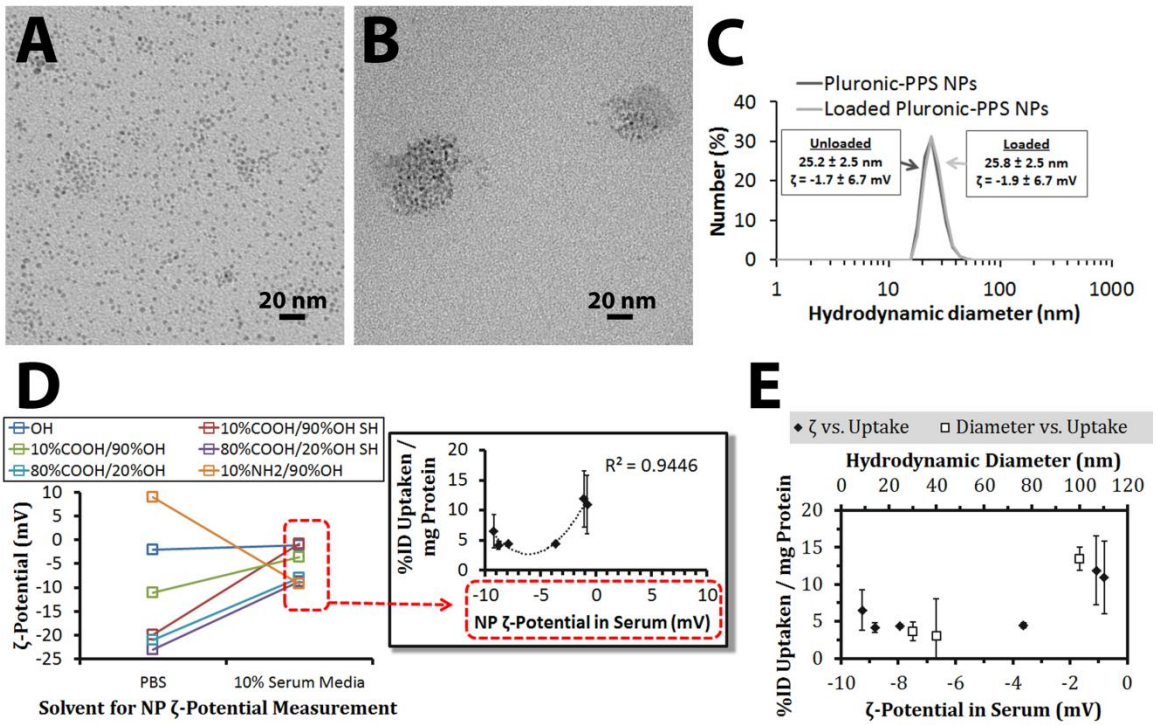

FIGURE 9. Effects of nanoparticle surface charge and chemistry on macrophage uptake. Representative TEM images of hydrophobic, unloaded 3 nm OA-USPIOs (A) and water-soluble Pluronic-PPS nanoparticles after loading with the OA-USPIOs (B). (C) The loading process does not significantly affect the hydrodynamic diameters or the zeta potentials inherent to the Pluronic-PPS nanoparticles. (D) ζ-potential of all nanoparticle formulations (color-coded by surface chemistry) was originally measured in PBS following synthesis, and again following incubation in 10% serum media. While modulation of surface chemistry allows for a wide range of ζ-potentials, this range is compressed due to interactions between nanoparticles and media components. Uptake of nanoparticles correlated with their surface charge as measured in media (inset; red dotted boxes indicate source of data for x-axis), according to a parabolic distribution. To account for differences in USPIO loading efficiency across the different Pluronic-PPS nanoparticle formulations, nanoparticle uptake was normalized to the initial dose administered as well as cell content indirectly, via a protein assay. Error bars indicate standard deviation for 3 independent experiments. (E) Cell internalization data is plotted versus nanoparticle ζ-potentials measured in 10% serum media (solid squares). In order to determine which nanoparticle feature may be more determinant of non-specific interactions with macrophages, the effects of nanoparticle diameter have also been plotted for comparison (open squares).

The two formulations that were most efficiently internalized were the nanoparticles displaying the terminal OH (12 ± 5% ID/mg protein) and the 10%COOH/90% OH/SH (11 ± 5 %/mg). Uptake correlated with nanoparticle charge as measured in serum, yielding a parabolic trend with maximum uptake observed for cationic and strongly anionic nanoparticles (Figure 9D, $R^2 = 0.94$, inset). However, because interactions with serum compressed the range of nanoparticle zeta potentials, we were unable to experimentally explore uptake of the nanoparticles beyond the -10 mV – 0 mV range. Despite the narrow window of zeta potentials covered by the data, the trends suggest that non-specific uptake of nanoparticles may be promoted by nanoparticle cationicity or high anionicity. This is consistent with previous observations (Raynal, et al., 2004).

Uptake of nanoparticles in serum was minimized in the range of zeta potentials from -9.0 mV to -3.5 mV. A three-fold increase in uptake was measured for identically sized nanoparticles having zeta potentials in serum from -3.5 mV to -0.8 mV, representing a 77% decrease in anionicity. In comparison, a four-fold change in uptake was observed for a 60% decrease in PEG-PPS-USPIO diameter (100 nm to 40 nm). Over these ranges and conditions, macrophage uptake of these nanoparticles is 42% more sensitive to size than to zeta potential (Figure 9E).

To expand on this conclusion, we synthesized PEG-PPS-USPIOs containing an MMP-9-degradable peptide ([M9C]) within the PEG chain (Figure 10A-B). This design results in particles that respond to active MMP-9 in the environment by releasing a layer of PEG, effectively leading to a decrease in nanoparticle diameter.

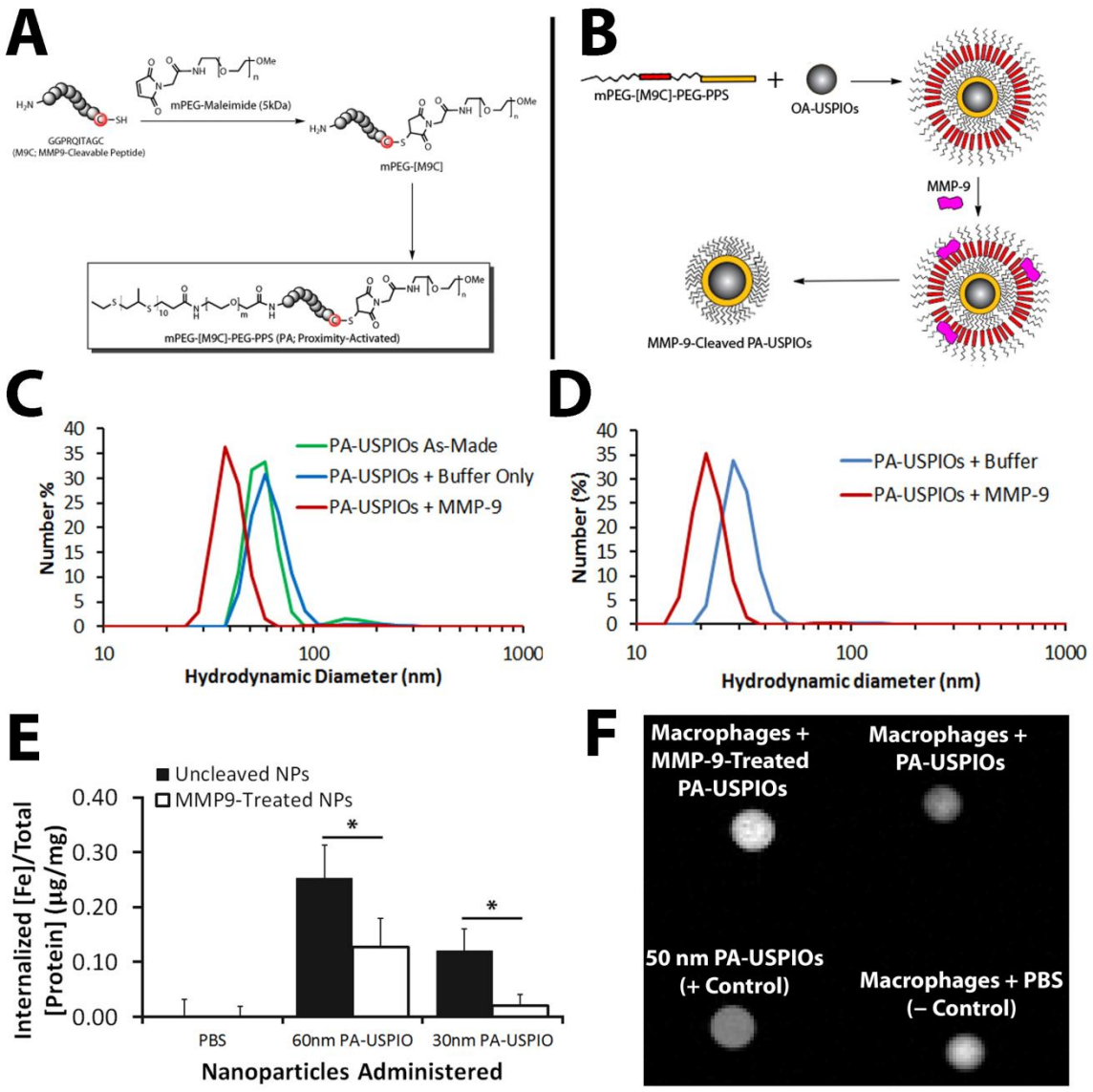

FIGURE 10. Behavior of MMP-9-responsive PA-USPIOs. (A) Synthesis of MMP-9-cleavable PEG-PPS chains (mPEG-[M9C]-PEG-PPS; PA) and (B) encapsulation of USPIOs to form PA-USPIOs. MMP-9 is able to recognize and cleave the [M9C] peptide sequence, resulting in release of a layer of PEG from the nanoparticle surface, accompanied by a decrease in nanoparticle hydrodynamic diameter. (C) DLS characterization of hydrodynamic diameters of as-synthesized 60 nm PA-USPIOs (C; green) and 30 nm PA-USPIOs (D; blue) demonstrates a loss in hydrodynamic diameter following treatment with MMP-9. (E) Buffer-treated or MMP-9-pretreated nanoparticles were delivered to THP-1 macrophages for 24 h. As a control, PBS was used in place of the nanoparticles. For both PA-USPIO formulations tested, the decrease in nanoparticle size following MMP-9 treatment results in less effective nanoparticle internalization by the macrophages. Error bars represent standard deviations from 3-6 independent experiments.*$p < 0.05$ by Student's t-test. (F) T_2-weighted MRI of THP-1 cells treated with MMP-9-cleaved PA-USPIOs appeared brighter than cells incubated with untreated PA-USPIOs, indicating that less cleaved nanoparticles were internalized by the macrophages versus the untreated PA-USPIOs.

Probes for MMP-9 activity are of wide interest because of the upregulation of MMP-9 in the progression of atherosclerosis (Gough, et al., 2006; Schellenberger et al., 2008; Sluijter, et al., 2006). Based on the studies described earlier, we hypothesized that this experimental contrast agent would experience less uptake by macrophages following treatment with MMP-9, relative to the as-synthesized, intact form.

These MMP-9-responsive contrast agents were synthesized by encapsulating 10 nm and 3 nm OA-USPIOs using ~10 kDa mPEG-[M9C]-PEG-PPS (subsequently referred to as 'PA' for protease-activatable), to produce 60 nm and 30 nm PA-USPIOs (Figure 10 C-D). Both PA-USPIO formulations responded to MMP-9 treatment with a 10-20 nm decrease in nanoparticle hydrodynamic diameters as measured by DLS, while ζ-potentials were not significantly affected (30 nm PA-USPIOs: -3.9 ± 6.4 mV pre-cleavage, -2.8 ± 5.9 mV post-cleavage; 60 nm PA-USPIOs: 0.0 ± 7.1 mV pre-cleavage, -4.7 ± 5.5 mV post-cleavage). For cell experiments, PA-USPIOs were incubated with MMP-9 for 24 h prior to their administration to THP-1 cells at equivalent iron doses. In both cases, MMP-9-treated PA-USPIOs were internalized significantly less effectively than their non-cleaved counterparts (Figure 10E). Most notably, the 30 nm PA-USPIOs experienced a six-fold decrease in nanoparticle uptake following MMP-9 cleavage (0.12 ± 0.04 μg Fe/mg protein pre-cleavage vs. 0.02 ± 0.02 μg/mg post-cleavage). Also of note is the slightly higher uptake of the MMP-9-treated 60 nm PA-USPIOs (final diameter = 40.0 ± 6.2 nm) relative to the untreated 30 nm PA-USPIOs (30.0 ± 2.6 nm).

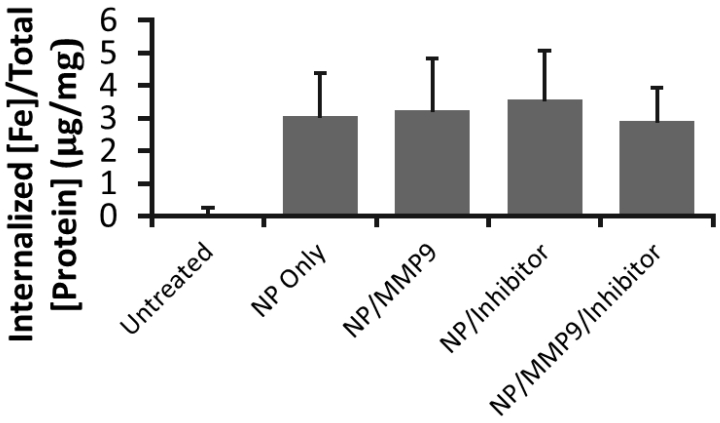

FIGURE 11. Negligible effects of MMP9 on uptake of MMP9-insensitive nanoparticles. Co-administration of 40 nm PEG-PPS-USPIOs (do not contain MMP-9-cleavable peptide) with MMP-9 does not significantly affect internalization of nanoparticles. THP-1 cells were treated with media only (untreated), nanoparticles only, or nanoparticles co-administered with 200 ng/mL MMP9 and/or 300 ng/mL MMP9 inhibitor. Because these nanoparticles do not contain MMP9-cleavable elements, their diameter is unaffected by treatment (data not shown). MMP9 treatment does not change the properties of the THP-1 cell membrane in a way that affects their interactions with nanoparticles. Error bars indicate standard deviation for three independent experiments.

Because these changes in nanoparticle internalization may be due to MMP-9-mediated modifications on the cell membranes, a series of control experiments were also performed, using non-cleavable, 40 nm PEG-PPS-USPIOs (Figure 11). In these experiments, co-administration of non-cleavable nanoparticles with MMP-9 did not lead to significant differences in nanoparticle internalization. Further, co-administration with a MMP-9 inhibitor also did not affect internalization. Taken together, the results suggest that the variations in PA-USPIO internalization by the THP-1 cells were attributable to the size of the nanoparticles, as the nanoparticle zeta potentials did not vary significantly before versus after treatment with MMP-9. Further, cellular capacity for nanoparticle internalization was unaffected by exposure to protease.

To determine if these MMP-9-dependent differences in nanoparticle internalization result in statistically significant changes in sample T_2 relaxation, and therefore, clinically relevant detection of MMP-9 activity in cell samples, 60 nm PA-USPIO-treated cells were pelleted and imaged on a 4.7T magnetic resonance imaging scanner (Figure 10F). Through the use of a Carr-Purcell-Meiboom-Gill (CPMG) spin-echo pulse sequence, MMP-9-treated PA-USPIOs appeared to exhibit higher mean gray intensities versus cells incubated with untreated PA-USPIOs.

While the PA-USPIOs exhibited T_2 = 4.82 ± 0.02 ms, the PA-USPIOs on the macrophages exhibited T_2 = 23.2 ± 3.5 ms. These rather strong changes in T_2 are somewhat surprising assuming that ~1% of the administered dose was taken up by the macrophages as measured in the earlier sections of this work. This implies that for each imaging slice, the concentration of iron responsible for T_2 signal modulation within that slice is about 100-fold less in the nanoparticle-treated cell samples versus the positive control. To quantify this phenomenon, the calculated values above (from first-principles measurements) can be plugged into the R_2 relaxivity equation:

$$[3] \qquad R_2 = \frac{1}{T_2 \times [Fe]}$$

in order to produce a measure of how effective the USPIOs are in modulating the local negative contrast. Given that measured T_2 in the cell samples is only ~5 times higher than the measurements in the positive control, the iron concentration in the cell samples would need to be about a fifth of the concentration in the positive control in order to maintain the same R_2 value. As we have seen, this is hardly the

case, and based on our data, we can conclude that the R_2 values in the cell sample would have to be on the order of 20-fold larger than the R_2 of the free-floating PA-USPIOs. These results indicate that following internalization by the macrophages, the PA-USPIOs are being manipulated in such a way that increases their ability to exert T_2 contrast.

This phenomenon can be explained by previous observations that aggregated or clustered superparamagnetic nanoparticles result in higher R_2 versus fully dispersed, singlet nanoparticles (Perez, O'Loughin, Simeone, Weissleder, & Josephson, 2002; S. S. Yu, R. L. Scherer, et al., 2011). Others have demonstrated via TEM that following endocytosis of iron oxide nanoparticles, macrophages can process the particles into lysosomes, where dense clusters of particles can usually be observed (Muller et al., 2007). Taken together, these other observations help explain how even a small amount of nanoparticle uptake results in a marked change in T_2 contrast in the system.

Summary

PEGylated nanoparticles are internalized by macrophages in a size-dependent fashion for diameters between 30-100 nm. Charge-uptake relationships were investigated by varying the surface properties of nanoparticles. While the data supports the possibility that cationic and strongly anionic nanoparticles may be internalized most effectively, within the ranges investigated, nanoparticle size, not charge, is a stronger determinant of non-specific uptake by macrophages. Based on this information, an MMP-9-sensitive nanoparticle was developed that decreases in

size following treatment with MMP-9. Macrophages respond to MMP-9-treated nanoparticles in a predictable fashion, and cleaved nanoparticles were consistently phagocytosed less efficiently than their untreated counterparts, demonstrating the effects of dynamic nanoparticle size modulation on macrophage uptake. These MMP-9-induced differences in uptake are also detectable via MRI. Despite the low levels of overall uptake over the 24 h incubation periods (≤ 1% initially administered dose), a significant increase in macrophage R_2 was observed. Presumably, and consistent with quantitative analysis, the clustering of nanoparticles into endosomes following endocytosis results in an increase in nanoparticle R_2, providing amplification of negative MR image contrast. The results presented here inform the design of nanoparticles to target or evade macrophages in future *in vivo* applications.

CHAPTER III

MACROPHAGE-SPECIFIC RNA INTERFERENCE VIA 'CLICK', MANNOSYLATED POLYMERIC MICELLES

Macrophages represent an important therapeutic target, because their activity has been implicated in the progression of debilitating diseases such as cancer and atherosclerosis. However, macrophage-specific drug delivery within pathologic sites is a significant challenge, as non-specific drug delivery may lead to off-target side effects and undesired interference with molecular mechanisms in healthy tissues. In this work, we designed and characterized pH-responsive polymeric micelles that were mannosylated using 'click' chemistry. Mannose was chosen in order to achieve CD206 (mannose receptor)-targeted drug delivery, though this 'clickable' platform could be generally used to attach other targeting ligands to this efficient siRNA carrier. CD206 is almost exclusively expressed on macrophages and dendritic cells, and upregulated in tumor-associated macrophages, a potentially useful target for cancer therapy. The glycosylated nanoparticles improved siRNA delivery into primary macrophages relative to a non-mannosylated version of the same carrier. Further, the mannose-targeted siRNA carriers achieved 85±10% knockdown of a model gene within 24h of delivery, relative to non-transfected macrophages. Finally, these nanoparticles were also avidly recognized and internalized by human macrophages, and facilitated the delivery of 13-fold more siRNA into these cells relative to model breast cancer cell lines. We anticipate these glycoconjugates to become an enabling technology to target macrophage

activity in various diseases, especially those where CD206 is up-regulated in macrophages present within the pathologic site.

Introduction

Macrophages perform a spectrum of functions, some of which have cytotoxic effects (i.e., when fighting infection) and others which promote cell growth, matrix remodeling, and wound healing (Kindt, et al., 2007). However, the dysregulation of these multifaceted activities can initiate pathogenesis and promote disease progression. For example, in various cancers, significant levels of macrophage infiltration have been observed, and this has been correlated with poor prognoses. This is hypothesized to occur because tumor-associated macrophages (TAMs) overexpress growth factors, VEGF, and matrix metalloproteinases, promoting tumor growth and invasiveness (Dirkx, et al., 2006). Therefore, macrophages are believed to represent an important therapeutic target in order to address a major underlying cause of cancer progression. Based on this hypothesis, technologies that enable cell-specific phenotypic modulation of aberrant macrophage activity would potentially be of high impact on human health.

A promising strategy to address aberrant macrophage behavior is through the use of RNA interference (RNAi) therapy. One approach to therapeutically harnessing RNAi involves the delivery of duplex RNA sequences called small interfering RNA (siRNA). siRNA is processed by the target cell's inherent machinery, with the ultimate effect of gene silencing through cleavage and degradation of mRNA complementary to the antisense strand of the delivered siRNA duplex (Fire et

al., 1998). By silencing master genes that regulate aberrant macrophage activity, RNAi therapy has the potential to directly block macrophage functions that lead to disease progression. However, due to their highly degradative phagocytic, endosomal, and lysosomal compartments, delivery and cytoplasmic release of siRNA in macrophages is particularly challenging, especially in primary cells (Stacey, Ross, & Hume, 1993). Conventional transfection methods have led to limited success, because they involve chemically-mediated transfection, based on strongly cationic materials which are cytotoxic and have been largely restricted to the laboratory bench (Lv, Zhang, Wang, Cui, & Yan, 2006).

While strategies exist for targeting macrophages at pathologic sites, some of these strategies require prior knowledge of the locations of these sites, in order to design injection routes for local delivery directly into the site of the macrophages (Kortylewski, et al., 2009; Watkins, et al., 2007). Such strategies include, for example, intratumoral or peritumoral injections of biologics, which may be useful when treating a primary tumor site but are poorly translatable to the treatment of dispersed, metastatic cancers. Alternative strategies require expensive technologies with uncertain practical clinical applicability, such as macrophage extraction, *ex vivo* modification, and adoptive transfer (Hagemann et al., 2008); antibody-nanoparticle conjugates (Briley-Saebo et al., 2011; Lipinski, et al., 2006); or custom phospholipids (Cormode, Skajaa, et al., 2008). Very few of these proposed approaches can be practically scaled for pharmaceutical purposes. Some of these methods deliver drugs to all cells non-specifically, and systemic interference with macrophage behavior may lead to autoimmune manifestations. Therefore, the clinical translation

of macrophage-targeted drug delivery is hampered by barriers spanning multiple disciplines, including targeting method, synthesis, and cost.

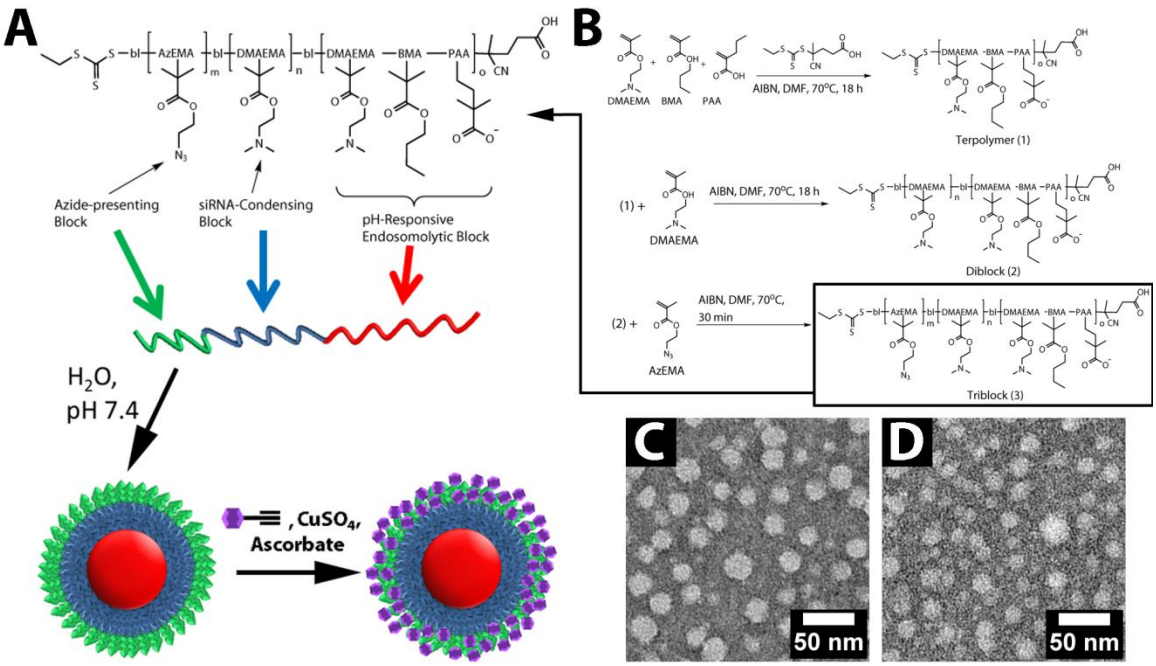

FIGURE 12. Smart Polymeric Nanoparticles for Macrophage-Specific Cytosolic Delivery of siRNA. (A) Schematic representation of the triblock copolymers developed in the manuscript, and resulting, multi-functional nanoscale siRNA delivery vehicles. The blocks include (red) a pH-responsive block that is capable of disrupting endosomes at low pH, (blue) a cationic block for condensation of nucleic acids, and (green) an azide-displaying block for conjugation of targeting motifs (purple) via 'click' chemistry. (B) Synthetic scheme for RAFT polymerization of triblock copolymers composed of blocks of AzEMA, DMAEMA, and the DMAEMA-*co*-BMA-*co*-PAA terpolymer. (C-D) Uranyl acetate-counterstained transmission electron micrographs of (C) micelles of diblock copolymers (2), which had an average diameter of 13.0 ± 6.1 nm (n = 367). (D) ManNPs had an average diameter of 9.7 ± 6.2 nm (n = 415). Scale bars = 50 nm.

Therefore, we designed and evaluated a polymeric glycoconjugate that can be assembled into nanocarriers for macrophage-specific siRNA delivery (Figure 12A). These agents represent a targeted version of construct reported by Convertine et al. (Convertine, Benoit, Duvall, Hoffman, & Stayton, 2009), which is capable of

mediating the escape of its cargo from the endosomal pathway, due to their ability to disrupt phospholipid membranes at pH < 6.5. The original version of this efficient siRNA carrier lacked any molecular targeting functionality and has the ability to enter a range of cell types via non-specific mechanisms.

The molecular structure includes a hydrophobic, pH-responsive component, a cationic, siRNA-condensing component, and a terminal segment with reactive sites for 'click' bioconjugation. These multifunctional polymers were synthesized via reverse addition-fragmentation chain transfer (RAFT) polymerization, which has the advantage of enabling the orthogonal polymerization of acrylate monomers displaying a wide range of chemical functionalities (Boyer et al., 2009). Additionally, it is a controlled radical polymerization method that leads to highly monodisperse products in an industrially-scaleable fashion, making it appropriate for pharmaceutical applications. Therefore, it is ideal for the proposed block copolymers, which feature carboxylic acids, azides, and tertiary amines among their functional groups (Figure 12). In aqueous media at pH 7.4, the polymers self-assemble into micelles and can be surface-functionalized with a wide range of possible molecular structures through the azide-alkyne 'click' reaction. 'Click' reactions have been widely employed to perform covalent conjugations for biological applications, due to their orthogonality, specificity, speed, and efficiency (Kolb & Sharpless, 2003).

Mannose was chosen as the targeting motif, since mannose receptor (CD206) is primarily expressed by macrophages and some dendritic cells (Taylor, Gordon, & Martinez-Pomares, 2005). In these cells, CD206 mediates the recognition and

endocytosis of mannosylated, fucosylated, or N-acetylglucosaminated substrates, which occurs via clathrin-coated vesicles (East & Isacke, 2002). Further, CD206 is upregulated in TAMs, and the potential to directly target these macrophages via mannose has not been explored (Vasievich & Huang, 2011). Mannose is also readily available at significantly lower costs than most alternative targeting motifs, improving the practicality of the approach. In this study, the capabilities of the mannose-targeted nanocarrier for cytosolic siRNA delivery and gene knockdown were evaluated in primary, murine bone marrow-derived macrophages (BMDMs). Specificity of the carriers was examined based on the ability of the glycoconjugate to deliver siRNA into immortalized human macrophages in competition with cancer cell lines. Results indicate that the described carrier offers significant opportunities for drug and siRNA targeting to TAMs.

Materials and Methods

All reagents and materials were purchased from Sigma-Aldrich (St. Louis, MO) and used as described unless described otherwise. Monomers for radical polymerization, including BMA, DMAEMA, PAA, and AzEMA, were all purified by vacuum distillation and stored at 4°C in clean, inhibitor-free containers. Riboshredder RNAse blend was purchased from Epicentre (Madison, WI). Immortalized cell lines were acquired from American Type Culture Collection (Manassas, VA). Cell culture supplies, including media, fetal bovine serum, antibiotics, and non-essential amino acids were obtained from Life Technologies (Carlsbad, CA). The siRNA sequences purchased for transfections were: FAM-labeled

anti-GAPDH siRNA (FAM-siRNA) and Cy3-labeled siRNA. The anti-PPIB siRNA used in knockdown experiments was purchased from Integrated DNA Technologies (Coralville, IA). Horse serum was purchased from Atlanta Biologicals (Norcross, GA).

Synthesis of 2-azidoethanol

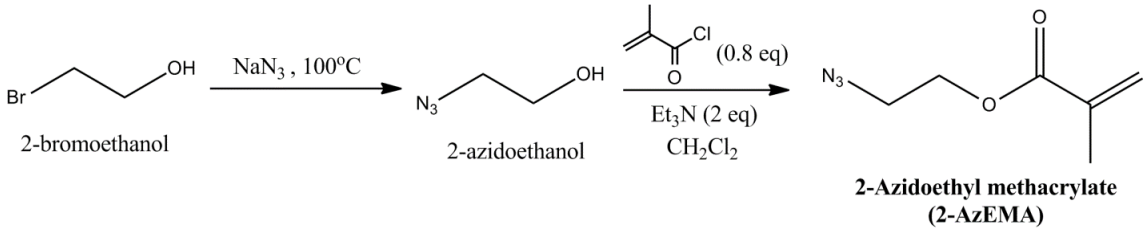

FIGURE 13. Synthetic scheme for 2-Azidoethyl methacrylate (AzEMA).

In a 500 mL round-bottom flask, 15.6 g of sodium azide (0.24 mol) was dissolved in 100 mL of nanopure water, followed by the addition of 5.67 mL of 2-bromoethanol (10 g, 0.08 mol; Figure 13). After capping the system with a septum, the reaction was heated to 80°C and allowed to stir overnight, during which the reaction changes darkens from yellow to orange. After allowing the reaction to cool to room temperature, the product was extracted 4x with 75 mL diethyl ether. Following two extractions, the aqueous phase changed colors from orange to clear. The pooled organic fractions were concentrated by rotary evaporation to yield a clear, colorless oil (95% yield; 6.66 g : 27.6137g – 20.9532g). ^{1}H NMR (400 MHz, $(CD_3)_2SO$): δ (ppm) 3.20 – 3.27 (t, 2H, C**H$_2$**N$_3$), 3.44 (s, 1H, O**H**), 3.54 – 3.60 (q, 2H, C**H$_2$**O). FT-IR (KBr pellet): 3380 cm^{-1} (broad, O-H), 2100 cm^{-1} (N_3), 1295 cm^{-1} (C-N), 1050 cm^{-1} (C-O).

Synthesis of 2-Azidoethyl methacrylate (AzEMA)

In a round-bottom flask, 10 g of 2-azidoethanol (0.11 mol) was mixed with 30.6 mL of Et_3N (22.3 g, 0.22 mol) in 50 mL of CH_2Cl_2 in a dry ice-acetone bath (-78°C; Figure 13). The reaction vessel was capped with a septum and degassed by alternating evacuation of the vessel and equilibration with nitrogen gas, 6x. Next, 8.6 mL of methacryloyl chloride (9.2 g, 0.088 mol) was injected into the system dropwise, and the reaction proceeded overnight (Caution: azide compounds may become shock-sensitive above 75-80°C, and this step is highly exothermic). The dry ice-acetone bath was allowed to warm to room temperature during this reaction. The crude product was extracted 3x with 1N hydrochloric acid to remove excess Et_3N, extracted 2x with 1N aqueous NaOH, and precipitated in nanopure water. After drying the organic fraction over $MgSO_4$, the product was concentrated under rotary evaporation to yield a dark red-orange liquid, which was further distilled under high vacuum to produce pure 2-azidoethyl methacrylate. ^{1}H NMR (400 MHz, $CDCl_3$): δ (ppm) 1.97 (s, 3H, C$\mathbf{H_3}$), 3.5 (t, 2H, C$\mathbf{H_2}N_3$), 4.33 (t, 2H, C$\mathbf{H_2}$O), 5.62 (s, 1H), 6.18 (s, 1H).

Synthesis of alkyne-functionalized mannose

The reaction diagram and characterization have been shown in Figure 14. In a round-bottom flask, 11 g of D-mannose (60 mmol) were dissolved into 30 mL dimethylsulfoxide (DMSO). To activate the sugar into a nucleophile, 10 mL Et_3N (triethylamine; 72 mmol) was added to the reaction, prior to the addition of 5 g propargyl chloride (67 mmol). After flushing the reaction with argon, the reaction

proceeded for 24 h at 40°C. Excess reagents were removed by 5X extraction into diethyl ether. The remaining ether-insoluble phase was dissolved into nanopure water and further extracted 5X with dichloromethane to remove other byproducts and DMSO. The product was flash-frozen in liquid N_2 and lyophilized. ^{1}H- and ^{13}C-NMR and HPLC characterization data are presented in Figure 14.

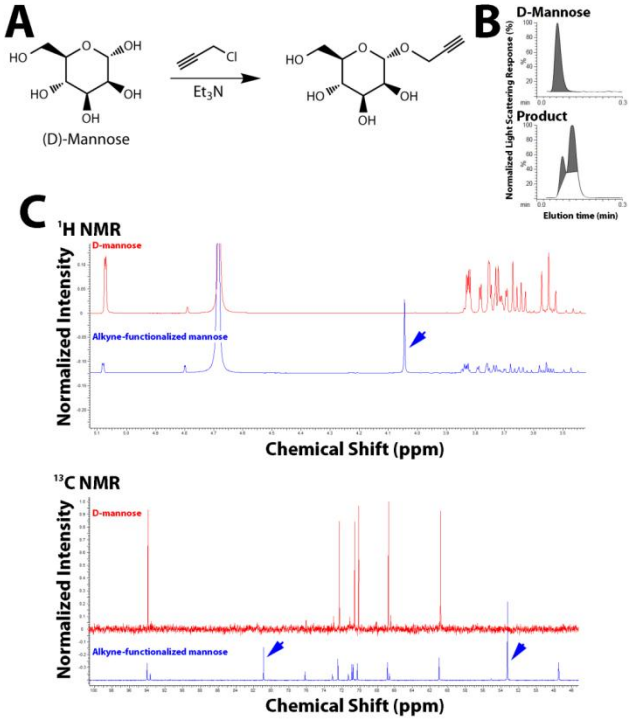

FIGURE 14. Synthesis and characterization of alkyne-functionalized mannose. (A) Reaction diagram for the synthesis of alkyne-functionalized mannose. The ideal product is shown on the right, but the scheme was not designed to be specific for the substitution of a particular hydroxyl group with a propargyl group. (B) Characterization of the precursor and product by HPLC. Evaporative light scattering chromatograms have been shown. The appearance of a large, later-eluting peak at ~0.1 min is due to the addition of a propargyl group onto the monosaccharide, which makes the molecule less polar than its precursor. The presence of excess precursor is not a concern, since the next reaction involving this mixture results in the 'clicking' of the modified sugar onto macromolecular assemblies (ManNPs), and purification by dialysis simply removes the excess precursor. (C) NMR spectroscopy of the precursor and product, with D_2O as the solvent. Because the propargyl chloride reagent is immiscible with water, the purification protocol used ensures the lack of this reagent in the final product. Blue arrowheads indicate peaks unique to the product, and are consistent with the attachment of alkyne groups onto the monosaccharide.

RAFT Polymerizations

Synthesis of the RAFT chain transfer agent (CTA) 4-cyano-4-(ethylsulfanylthiocarbonyl) sulfanylpentanoic acid (ECT) and 2-propylacrylic acid monomer have been described in detail in our previous work (Convertine, et al., 2009; C. E. Nelson et al., 2012). Polymerization of the 47%BMA-25%PAA-28%DMAEMA terpolymer was conducted at 70°C under N_2 for 18 h with DMF as the solvent (90 wt% in feed), an initial monomer-to-CTA molar ratio of 100, and a CTA to initiator molar ratio of 10. After rapidly cooling the reaction in an ice bath, the organic mixture was mixed 1:1 (by volume) with aqueous HCl at pH 2, which initially results in a turbid mixture but quickly turns clear-yellowish as the monomers and polymers equilibrate with the acidic environment. Next, the polymer was precipitated 7x in hexanes and 2x in diethyl ether to remove residual monomers. Finally, the polymers, which were at this point still soluble in the acidic aqueous medium, were dialyzed across 10kDa molecular weight cutoff membrane (Pierce, Rockford, IL) against nanopure water (pH ~ 5, so no change in polymer solubility was observed) overnight. Lyophilization yielded pure terpolymer, which was a yellowish powder (Table 5).

TABLE 5. Characterization of Polymers Synthesized via RAFT Polymerization

Polymer	dn/dc (mL/g) [a]	Target M_n (Da)	M_n (Da) [b]	M_w (Da) [b]	PDI	D_h (nm)	ζ-Potential (mV)
Terpolymer	0.081	14000	11400	13900	1.22		
Diblock	0.049	21000	16800	20700	1.23	34.2 ± 2.2	10.8 ± 11.2
Triblock (Before 'click')	---	22000	22300	28900	1.29	28.0 ± 1.5	19.6 ± 11.7

[a]Measured in off-line batch mode in a Shimadzu RID-10A differential refractive index (dRI) detector, with DMF + 0.1M LiBr as the solvent.
[b]Measured via gel-permeation chromatography with MALS and dRI in-line with columns.

The same monomer:macroCTA:I molar ratios, and 90 wt% DMF conditions were used to polymerize the DMAEMA block onto the terpolymer macroCTA. To purify the diblock, the completed reaction was precipitated in ether at -20°C for 1h, and then pelleted by centrifugation at 800 x g for 5 min. After discarding the supernatant, the pellet was resuspended in deionized water, forming a slightly turbid suspension. Dialysis against deionized water for 48 h, across 10kDa-MWCO membrane, and lyophilization yielded pure diblock, which was a yellow-white powder.

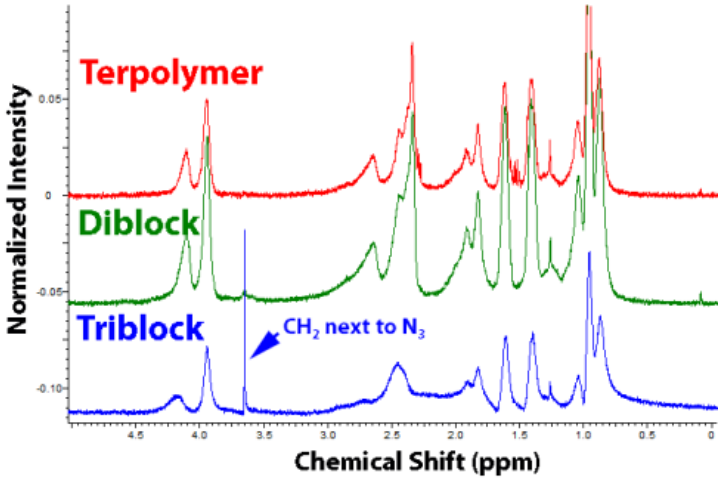

FIGURE 15. Characterization of Copolymers Synthesized via RAFT Polymerization. NMR spectra of the purified copolymers were collected following each round of synthesis and dialysis. Polymers were dissolved in $CDCl_3$ prior to spectral acquisition. The key difference between the terpolymer and the diblock is a quantifiable increase in DMAEMA composition (for diblock, relative to terpolymer). The triblock exhibits an additional peak at ~3.7 ppm, which is characteristic of the alkyl protons next to the free N_3 group presented on the AzEMA block.

The polymerization of the AzEMA block onto the diblock was done to form triblock copolymers according to the same protocol. This mixture was then extensively dialyzed across 10kDa MWCO membranes overnight, against nanopure

water, to yield the completed triblocks. Triblocks were dissolved in deionized water at 1 mg/mL and stored at -20°C until ready for use in 'click' reactions.

^{1}H-NMR spectra for all polymers are shown in Figure 15.

'Click' Chemistry

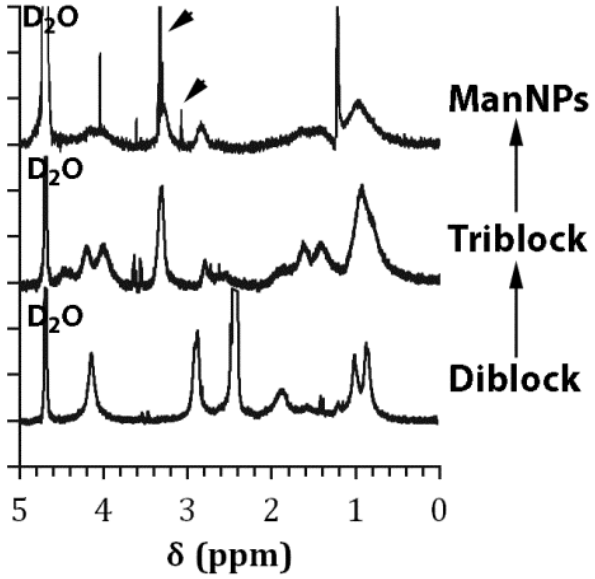

FIGURE 16. NMR Spectroscopy of Micelles of Block Copolymers in D_2O. The surface moieties displayed by the various micelles are plotted at different steps of synthesis. All polymers were extensively dialyzed across 10 kDa-MWCO membranes and lyophilized, prior to reconstitution in D_2O for NMR measurements. The diblock co-polymer forms micelles that display DMAEMA, as evidenced by the broad peaks in its characteristic regions (red). This layer is effectively shielded following the polymerization of AzEMA, which yields strong azide peaks and a small hump in the polymer backbone region (characteristic of the alkyl backbone that composes all poly-acrylates). The mannosylation of the triblock by 'click' chemistry results in the appearance of new peaks in the 3.0-3.5 ppm region, which is slightly lower than where mannose peaks have been shown to appear (Figure 14), but is consistent with the immobilization of these polar molecules onto a hydrophobic polymeric backbone.

In a scintillation vial, 1 mL of triblock co-polymer (1 mg/mL in nanopure H_2O) was mixed with 6 mg alkyne-functionalized mannose (27.5 mmol). After the addition of $CuSO_4$ and sodium ascorbate to final concentrations of 1 mM and 5 mM,

respectively, the reaction was allowed to proceed at 37°C on an orbital shaker in the dark for 48 h. Excess copper was removed by treating the crude product with Chelex 100 Resin (Bio-Rad Laboratories, Hercules, CA) according to manufacturer's instructions. The product was filtered through a 0.45 μm Teflon filter to remove the resin, and then dialyzed through a 2 kDa-MWCO membrane against deionized water to remove excess reactants. ^{1}H-NMR characterization of the micelles before and after 'click' chemistry is shown in Figure 16.

NMR and Chromatography

Proton and carbon nuclear magnetic resonance (^{1}H and ^{13}C NMR) spectra were obtained at 400 MHz using a 9.4 Tesla Oxford magnet operated by a Bruker AV-400 console.

Gel permeation chromatography (GPC) was performed with dimethylformamide (DMF) + 0.1 M LiBr as the mobile phase, by running samples through three resolving columns in series (1 × TSKGel Alpha4000, 2 × TSKGel Alpha3000; Tosoh Bioscience, King of Prussia, PA). Columns were maintained at 60°C, and chromatograms were collected via a Shimadzu RID-10A refractive index detector (Shimadzu Scientific Instruments, Columbia, MD) and a Wyatt miniDAWN Treos multi-angle light scattering detector (MALS; Wyatt Technology, Santa Barbara, CA). Data collection and analysis was achieved through the Wyatt ASTRA software (v 5.3.4). Determination of absolute molecular weights was done by preparing known concentrations of purified polymer samples, and measuring their dn/dc in offline batch mode.

Analytical high performance liquid chromatography–mass spectrometry (HPLC-MS) was performed on an Agilent 1200 series system (Palo Alto, CA) as described elsewhere (S. S. Yu, R. L. Koblin, et al., 2011).

Nanoparticle Characterization

To prepare polymeric nanoparticles for transmission electron microscope (TEM) imaging, carbon film-backed copper grids (Electron Microscopy Sciences, Hatfield, PA) were inverted onto droplets containing aqueous nanoparticle suspensions (1 mg/mL) and blotted dry. Next, all samples were inverted onto a droplet of 3% uranyl acetate and allowed to counterstain for 2 min. After blotting the sample dry, samples were further desiccated *in vacuo* for 2 h prior to imaging on a Philips CM20 system operating at 200 kV. Images were collected using a CCD camera with AMT Image Capture Engine software (v 600.335h; Advanced Microscopy Techniques, Danvers, MA).

Hydrodynamic diameter and ζ-potential of NPs were investigated by dynamic light scattering (DLS) in a Malvern Zetasizer Nano-ZS (Malvern Instruments Ltd., Worcestershire, U.K.).

siRNA Protection Experiments

50 pmol Cy3-labeled siRNA was complexed with mannosylated nanoparticles at N:P ratios of: 1:2, 1:1, 2:1, and 4:1. Ratios were calculated by using the concentration of NH^+ (based on the degree of polymerization of the DMAEMA homopolymer block of the polymers, and the concentration of the polymers in μM)

and PO_4^- (based off the number of siRNA base pairs and the concentration of siRNA in μM). Because the pK_a of the DMAEMA occurs at around pH 7.2, we assumed that the DMAEMA block was 50% charged for the calculation of N:P ratios. The complexes were loaded onto a 2% agarose gel containing 1.5 μM ethidium bromide.

The RNAse protection experiment was performed on siRNA complexes with either diblock copolymers (0.5:1 N:P ratio) or mannosylated nanoparticles (0.5:1 or 4:1 N:P ratios), as described elsewhere (Kirkland-York et al., 2010),

Animals and Cell Lines

Animal work was approved by the Vanderbilt University Institutional Animal Care and Use Committee. All mice were on an FVB background strain. Bone marrow-derived macrophages were isolated from tibiae and femurs immediately after sacrificing the mice and cultured as described elsewhere (Connelly, Jacobs, Palacios-Callender, Moncada, & Hobbs, 2003). Cells were seeded at 300,000 cells/cm^2 for all experiments.

L929 murine areolar fibroblasts were cultured in DMEM (purchased containing 4.5 g/L glucose, 110 mg/L sodium pyruvate, and 3.7 g/L $NaHCO_3$), supplemented with 10% FBS, 1 U/mL penicillin, 1 μg/mL streptomycin, and 1% MEM non-essential amino acids. To create the macrophage colony-stimulating factor (M-CSF) source for differentiating bone marrow into BMDMs, 1.16 x 10^7 L929 cells were seeded into T-225 flasks, in 77 mL of media. After 10 d of culture without any media changes, the supernatant was filtered through a 0.2 μm nylon membrane, and stored at -80°C until further use (Weischenfeldt & Porse, 2008).

THP-1 human leukemic monocytes were cultured in RPMI-1640 media containing 10% FBS, 1 U/mL penicillin, 1 μg/mL streptomycin, 1 X MEM vitamins (Mediatech, Manassas, VA), 120 μM β-mercaptoethanol, and 10 mM HEPES. For experiments, these non-adherent cells were plated at 300,000 cells/cm^2 in growth media containing 1 μg/mL lipopolysaccharide for 3 d, which activates the monocytes into macrophages and induces adherence of the cells to the substrate. For one experiment (shown in Figure 4), cells were seeded at 25,000 cells/cm^2, in order to keep cell number constant across the three independent variables that were tested (cell type).

MDA-MB-231 and MDA-MB-468 cells were cultured in DMEM (purchased containing 4.5 g/L glucose, 110 mg/L sodium pyruvate, and 2 mM L-glutamine), supplemented with 10% fetal bovine serum, 1 U/mL penicillin, 1 μg/mL streptomycin, and 1% MEM non-essential amino acids. For experiments, the cells were trypsinized and then re-seeded into 24-well plates at a density of 25,000 cells/cm^2.

All cells were maintained in a 5% CO_2 incubator at 37°C.

Transfections

Complexes were prepared by as described above. For some transfections, Lipofectamine RNAiMAX® (Life Technologies, Carlsbad, CA) was used to complex siRNA, and was used according to manufacturer's instructions (Except for knockdown experiment, which was conducted for 24 h in order to compare all vehicles in head-to-head fashion). Cells were prepared for transfection by rinsing

wells twice with PBS to remove growth medium. This was replaced with serum-free medium, which is composed of DMEM with 4.5 g/L glucose, 1 U/mL penicillin, 1 μg/mL streptomycin, and 2 mM L-glutamine. Complexes were then added to the wells such that the final concentration of siRNA in the wells was 50 nM (ten-fold dilution from stock). At set time points, wells were rinsed thrice with PBS to remove unbound complexes. Cells were then processed according to the desired experiment as described below.

Transfected cells were analyzed for cell viability using a Live-Dead kit (Life Technologies) according to the manufacturer's instructions. Quantification of live and dead cells was done by flow cytometry.

Quantitative real-time PCR

Total RNA was isolated from cell samples using the RNeasy Kit and QIAShredder columns (Qiagen). After the removal of genomic contamination through DNAse treatment (DNA-free kit, Life Technologies), cDNA libraries were constructed using a reverse transcriptase kit (Life Technologies).

For qRT-PCR, Primers were purchased from Integrated DNA Technologies (Coralville, IA). PPIB sense: 5'- TTCCATCGTGTCATCAAG-3' and antisense: 5'-GAAGAACTGTGAGCCATT-3'. β-actin sense: 5' – CACACCTTCTACAATGAG – 3' and antisense: 5' – GGTCTCAAACATGATCTG – 3'. CD206 sense: 5'-CAAGGAAGGTTGGCATTTGT - 3' and antisense: 5'– CCTTTCAGTCCTTTGCAAGC - 3'. Samples were treated with a SYBR Green PCR Master Mix in MicroAmp Fast optical

96-well plates (both from Life Technologies), according to the manufacturer's instructions.

Data was analyzed for C_T values using the Applied Biosystems 7500 Fast Software (version 1.4.0). All plots of SYBR Green fluorescence versus cycle were set to the same baseline (usually within cycles 3-10; all of the sigmoidal amplification curves did not appear until after cycle ~15), thresholded evenly (same within samples analyzed for the same gene), and the intersection of the amplification curve and the threshold was reported as the C_T value. Relative expression (RE) of a gene of interest (goi) was calculated against a control gene (cont; GAPDH or β-actin), according to the formula: $RE_{goi} = 2^{(C_{T,cont} - C_{T,goi})}$.. Fold-change in goi expression was calculated by dividing RE_{goi} of experimental samples over RE_{goi} of control samples (usually untreated cells).

Flow Cytometry

Flow cytometry was performed on a BD FACSCalibur system (Franklin Lakes, NJ), operated via a BD Cellquest Pro (version 5.2) software. The FL1 channel was used for the quantification of FAM emission of each cell. Data analysis and reporting were performed on FlowJo (version 7.6.4).

Confocal Microscopy

Transfections were performed as described above for 1,2, or 4 h. To prepare cells for confocal microscopy, they were washed with PBS, fixed for 15 min with 10% buffered formalin, rinsed 3x with PBS, and then stained with DAPI (Invitrogen,

Carlsbad, CA) for 10 min. After rinsing cells 3x with PBS, slides were mounted with the Invitrogen ProLong Antifade kit. Imaging was performed on a Zeiss LSM 710 system (Oberkochen, Germany).

Images were processed via ImageJ software (version 1.43u; National Institute of Health, Bethesda, MD). 8-bit LSM images were converted to RGB images in order to make them compatible with the built-in "Merge Channels" function on the software, which creates the merged fluorescence overlay images used for some of the figures. Due to the low DAPI signal in some raw image files, the brightness/contrast of the DAPI channels for all images reported here were enhanced to varying levels.

Hemolysis Assays

Whole, unfractionated human blood samples were obtained from consenting anonymous, healthy adults under Vanderbilt University Institutional Review Board (IRB) approval (Protocol #111251). Whole blood (in K_2EDTA-coated Vacutainer tubes) was centrifuged at 1500 rpm for 5 min (400 x g), and plasma was replaced with an equivalent volume of 150 mM NaCl. After inverting the tubes a few times to resuspend the pellet, and centrifuging the tubes at 1500 rpm for 5 min, the buffer was replaced with PBS at pH 7.4. The cell suspension was split into four tubes, corresponding to each pH to be assayed, and centrifuged at 1500 rpm for 5 min again. The supernatants were discarded, and replaced with PBS pre-adjusted to pH 5.6, 6.2, 6.8, or 7.4. 1 mL of each stock suspension was further diluted 1:50 into PBS at the corresponding pH, prior to further use.

In black, round-bottom 96-well plates, 10 μL of each test polymer, at three concentrations (20, 100, 800 μg/mL), were loaded. After the addition of 190 μL of purified red blood cells, the final concentrations of these polymer samples were adjusted to 1, 5, and 40 μg/mL, respectively. As controls, plain PBS (negative control) or 20% Triton X-100 (positive control) were added to some wells. These mixtures were allowed to incubate at 37°C in a 5% CO2 incubator for 1 h, following which they were centrifuged at 1500 rpm for 5 min. 100 μL of the supernatant in each well was transferred to clear, flat-bottom 96-well assay plates. This protocol enables the quantification of the release of hemoglobin as erythrocytes are lysed. Absorbance was plate-read at 450 nm using a Tecan Infinite F500 system (Männedorf, Switzerland), operated by Tecan i-Control software (version 1.7.1.12). The absorbance of the negative control sample was set to 0% hemolysis, and the absorbance of the positive control sample was set to 100% hemolysis. After setting up a linear regression based on these two data points, the resulting formula was applied on all other wells to calculate % hemolysis.

Statistical Significance

For all experiments, statistical significance was assessed using the unpaired Student's t-test or one-way ANOVA as indicated in the text.

Results

Modular Design, Synthesis, and Characterization of Mannosylated siRNA Delivery Vehicles

The synthesis of the mannosylated delivery vehicles could be summarized into three parts: (1) the polymeric components were synthesized in three sequential iterations of RAFT polymerization and purification (Figure 12), (2) alkyne-functionalized mannose was separately synthesized (Figure 14), and (3) the polymers from (1) are formed into micelles and reacted with the alkyne-functionalized mannose from (2). These steps result in immobilization of mannose onto the micelle corona through reaction with the distal azide groups via 'click' chemistry (Figure 12A).

The polymers that make up the mannosylated siRNA carriers were synthesized via RAFT polymerization. These modules include a pH-responsive block (Figure 12A, red), a cationic block for condensing nucleic acids (blue) and an azide-presenting block (green) for the attachment of alkyne-functionalized ligands. First, a ~14 kDa random terpolymer block composed of 47% butyl methacrylate (BMA), 25% 2-propylacrylic acid (PAA), and 28% 2-dimethylaminoethyl methacrylate (DMAEMA) was synthesized (Figure 12B; Table 5). The percentages represent molar composition of each monomer in the copolymer structure, as determined by proton nuclear magnetic resonance spectroscopy (^{1}H-NMR).

To form a hydrophilic, corona-forming segment, a cationic DMAEMA block (8.9 kDa by ^{1}H-NMR) was block-polymerized from the terpolymer, yielding a diblock copolymer (22.8 kDa; Figure 12, red and blue; Table 5). This diblock copolymer forms micellar nanoparticles (Figure 12C), consistent with previous work by others (Benoit, Srinivasan, Shubin, & Stayton, 2011; Convertine, et al., 2009; Duvall, Convertine, Benoit, Hoffman, & Stayton, 2010; Palanca-Wessels et al., 2011).

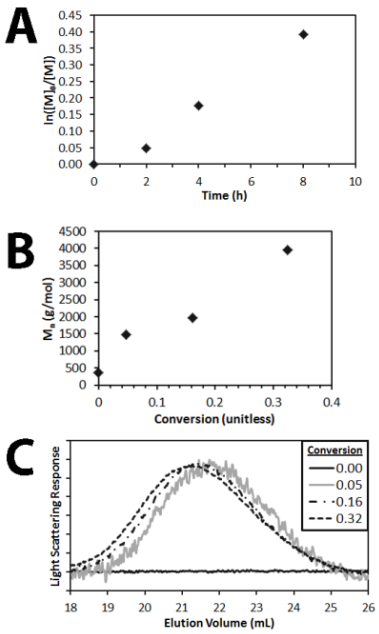

FIGURE 17. RAFT Polymerization Kinetics of AzEMA. (A) Semilogarithmic kinetic plot of monomer conversion. (B) M_n vs. monomer conversion. (C) Gel permeation chromatograms of light scattering response (signal normalized to tallest peak in chromatogram, therefore scale is not the same across samples) vs. elution volume, as a function of monomer conversion (see legend). Reaction conditions: [AzEMA]:[DCT]:[AIBN] 1000:10:1, 85 vol % DMF, T = 70°C.

Finally, an azide-presenting block composed of 2-azidoethyl methacrylate (AzEMA) was extended from the DMAEMA terminus of these polymers (Figure 15). The synthetic route for AzEMA (Figure 13) was significantly modified from published schemes for the synthesis of 3-azidopropyl methacrylate, a similar monomer, in order to remove the need for chromatographic purification of the desired product (Crownover, Duvall, Convertine, Hoffman, & Stayton, 2011; Sumerlin, Tsarevsky, Louche, Lee, & Matyjaszewski, 2005). The polymerization kinetics of AzEMA have also been shown here (Figure 17).

Morphologically, the triblock copolymers are expected to form assemblies as depicted in Figure 12, where the azide-presenting block effectively shields the pDMAEMA block in the final micellar structures. However, the addition of the final, AzEMA block to the base diblock leads to a 6 nm decrease in the hydrodynamic diameter of the resulting micelles, and a corresponding +10 mV increase in ζ-potential (Table 5). NMR spectra of the micelles were also obtained in D_2O. The base diblock micelles featured peaks in chemical shift regions characteristic of DMAEMA, while the micelles composed of the triblock produced none of these peaks (Figure 16). Furthermore, the latter micelles featured a strong peak at 3.6 ppm, a region that is consistent with the expected chemical shift of alkyl protons adjacent to an azide group. Therefore, the triblock copolymers form micelles that present azide groups at their corona, enabling the facile immobilization of alkyne-functionalized ligands onto the micelles.

The synthesis of alkyne-functionalized mannose (Figure 14) was adapted from a synthetic scheme for derivatized sugars presented by Plotz and Rifai (Plotz & Rifai, 1982). The resulting NMR spectra of the product indicated the successful alkyne-functionalization of the monosaccharide. HPLC showed that the product is 70-80% pure following synthesis. No further purification was done because during micelle functionalization, any non-functionalized mannose that was present would be unable to 'click' onto the polymers and was easily removed via dialysis from the final, mannosylated nanoparticles (ManNPs).

Following the 'click' reaction to functionalize the polymers with mannose, the polymers retained the ability to form micellar nanoparticles, similar to those formed

by the diblock copolymers lacking the azide block and mannose (Figure 12C-D). The ManNPs also exhibited a distinct NMR signature compared to that of the micelles made of triblock copolymer before the 'click' mannosylation reaction (Figure 16). This is particularly evident in the 3.0-3.5 ppm region, where the appearance of a broad peak, corresponding to mannose, is consistent with the success of the 'click' reaction.

ManNPs Form Complexes with siRNA and Protect Cargo from Degradation

The completed ManNPs are able to complex siRNA in an N:P ratio-dependent fashion as evidenced by a gel retardation assay (Figure 18A). The slow-moving band corresponding to siRNA/ManNP complexes increased in brightness with increasing N:P ratios, while the fast-moving band corresponding to free siRNA decreased in brightness. The ManNPs are also able to protect their cargo from degradation by RNAses, and this ability is elevated at higher N:P ratios (Figure 18B). In this study, the degradation of siRNA results in a hyperchromic effect, which is characterized by increased sample absorbance at 260 nm (Kirkland-York, et al., 2010). The 65% increase in Abs_{260} of free siRNA within 10 min of RNAse treatment is a demonstration of this effect and is used as a positive control. At a 1:2 N:P ratio, diblock copolymers were more effective than the ManNPs in protecting siRNA from degradation. At an 4:1 N:P ratio, the ManNPs were most effective at protecting their cargo from RNAse degradation, which was in agreement with the siRNA complexation seen in the gel retardation assay.

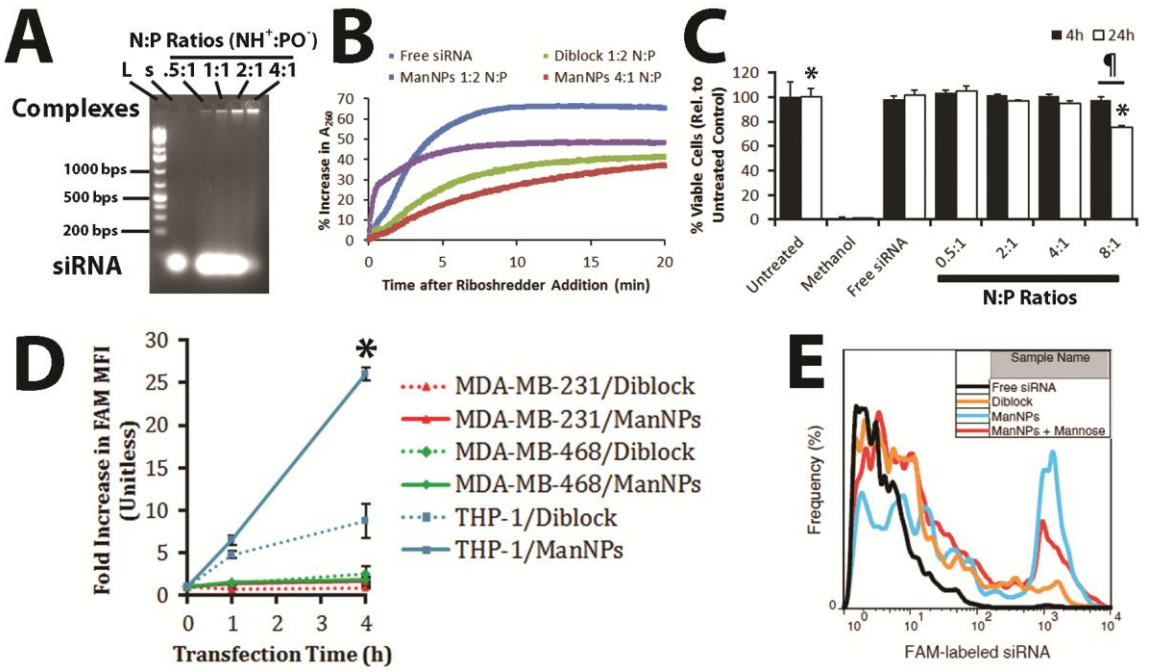

FIGURE 18. ManNP siRNA Complexation, Nuclease Protection, and Enhanced siRNA Delivery into Macrophages. (A) Gel retardation assay of siRNA-loaded ManNPs at various N:P ratios. Control samples included the DNA ladder (L; numbers indicate # base pairs corresponding to band) and free, Cy3-labeled siRNA (s). (B) Protection of siRNA from degradation by RNAses. Micelle/siRNA complexes were incubated with RNAse cocktails. RNAse-mediated degradation of siRNA was characterized by a hyperchromic effect at 260 nm, which is less pronounced for samples containing the polymeric nanoparticles. (C) Cytotoxicity assay of immortalized THP-1 macrophages, treated with ManNPs complexed with siRNA at various N:P ratios. Error bars represent standard deviation from 3 independent experiments (*,¶ $p < 0.01$). (D) ManNPs enhanced siRNA delivery to macrophages up to 26-fold over two model breast cancer cell lines, and 3-fold in macrophages relative to untargeted diblock carriers, as measured via flow cytometry. (*$p < 0.01$ vs. all other treatment groups at 4 h timepoint; n = 3). (E) Flow cytometry confirms improved delivery of FAM-siRNA into BMDMs via ManNPs (blue) relative to untargeted nanoparticles (orange) or free siRNA without vehicle (black) within 4 h of administration. Co-administration of 100 mg/mL free mannose with the ManNPs reduces delivery of siRNA into BMDMs (red).

ManNPs Are Cytocompatible at N:P < 8:1

Immortalized human THP-1 macrophages were incubated with siRNA-loaded ManNPs at various N:P ratios, with siRNA concentration kept at 50 nM for all conditions. Cell viability was assessed via calcein AM/ethidium homodimer incorporation at 4 or 24 h after ManNP delivery, and experimental groups were

quantified via flow cytometry relative to untreated cells (100%) or methanol-killed cells (set to 0%; Figure 18C). For all N:P ratios investigated, negligible cytotoxicity was observed at 4 h of treatment. However, at 24 h, only 76 ± 1% of the cells treated at the 8:1 N:P ratio remained viable, indicating that prolonged treatment of BMDMs with ManNPs/siRNA at this charge ratio results in significant cytotoxicity (¶ $p < 0.01$, vs. 4 h treatment; *$p < 0.01$ relative to 24 h untreated cells). The 4:1 N:P ratio was selected for further experiments because it did not result in significant cytotoxicity at 24 h.

ManNPs are Avidly Internalized by Human Macrophages, but not Cancer Cells

To examine the potential of using the ManNPs to selectively target TAMs, ManNPs loaded with FAM-siRNA were incubated with immortalized human macrophages (THP-1) or human breast cancer cell lines (MDA-MB-231 & MDA-MB-468) for up to 4 h. Cellular internalization of the siRNA was assessed via flow cytometry (Figure 18D). As controls, untreated cells were measured, as well as cells treated with complexes made with the non-targeted diblock copolymers. For both breast cancer cell lines, internalization of FAM- siRNA/ManNPs was relatively minimal, and both cell types experienced less than a two-fold increase in FAM mean fluorescence intensity (MFI) over the 4 h study period. With the macrophages, the same study period led to a 26-fold increase in the FAM MFI of the cells, showing that these cells preferentially internalize the constructs relative to the model cancer cell lines (Figure 18D; *$p < 0.01$ vs. all other treatment groups at 4 h). Further, ManNPs

facilitated a 3-fold increase in siRNA delivery to the macrophages, relative to the non-targeted diblock micelles.

ManNPs Enhance CD206-Dependent Intracellular siRNA Delivery and Target Gene Knockdown in Primary Murine Macrophages

siRNA delivery and gene knockdown were next examined in primary murine bone marrow-derived macrophages (BMDMs). Within 4 h of siRNA administration, ManNPs improved delivery of FAM-siRNA into macrophages by more than 40-fold relative to free siRNA or fourfold relative to the untargeted, diblock copolymers (Figure 18E; $p < 0.01$). Notably, the uptake of ManNPs can be partially blocked via co-administration with D-mannose, indicating that internalization of the ManNPs is mediated by the mannose receptor.

In support of these observations, imaging of the uptake of fluorescently-labeled siRNA into BMDMs was accomplished by confocal microscopy (Figures 19-20). Consistent with the flow cytometry results, mannose targeting significantly increased siRNA delivery into macrophages, and co-administration of D-mannose with the ManNPs reduced FAM-siRNA signal in the BMDMs. Significant levels of FAM-siRNA can be visualized in the BMDMs within 1-2 h of administration. The punctate staining (Figure 20) is consistent with the sequestration of the siRNA into intracellular vesicles. Within 4 h, the FAM staining becomes more diffuse, suggesting that the FAM-siRNA has escaped the endosomal compartment and accessed the cytosol.

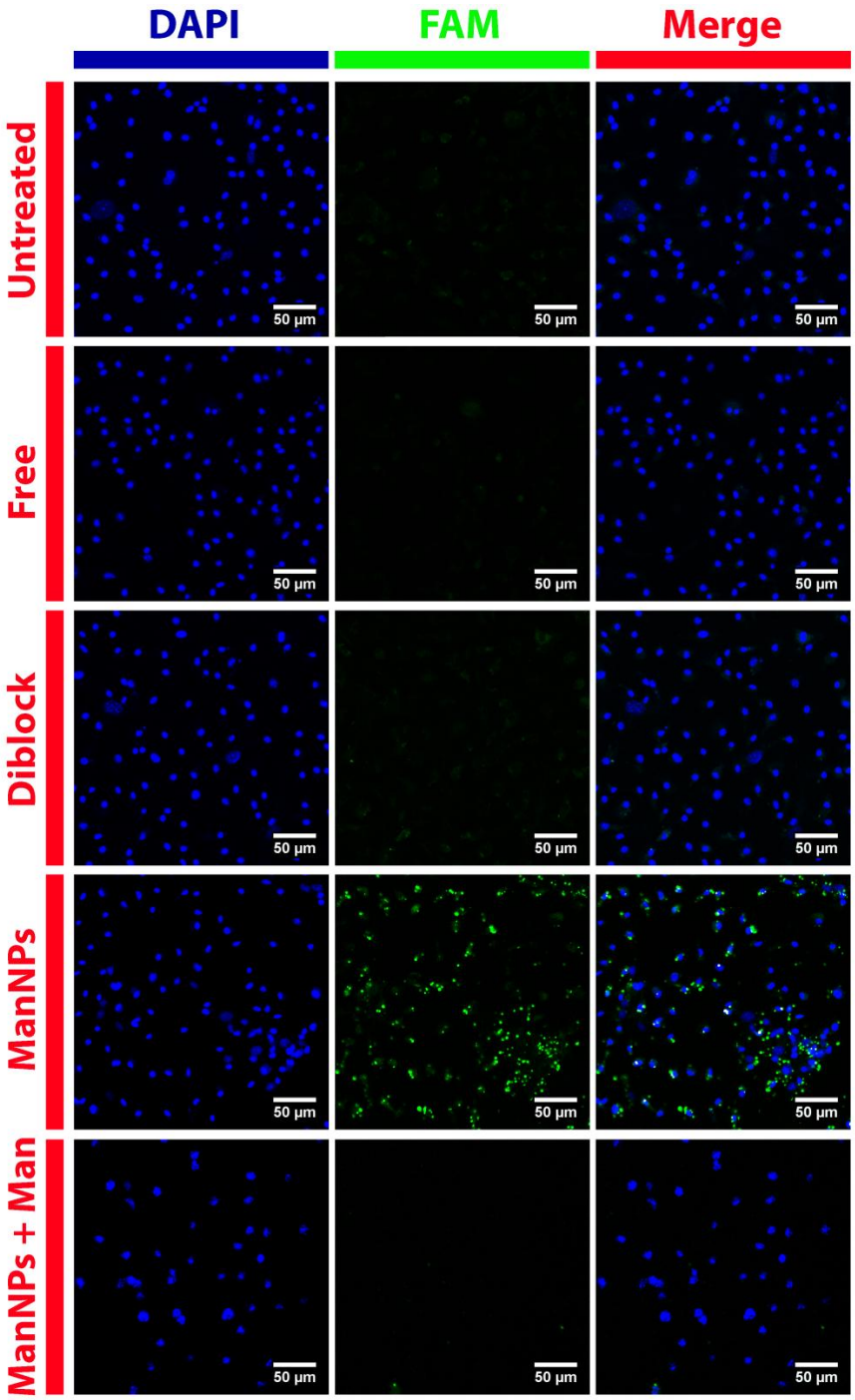

FIGURE 19. Improved Delivery to Primary Macrophages using ManNPs with Specificity for Mannose Receptor (CD206). Following 4h of transfection with FAM-siRNA (green; free or complexed into nanoparticles), BMDMs were fixed, nuclei stained with DAPI (blue), and imaged via confocal microscopy. (Scale bars = 50 µm). Mannosylation of the polymeric vehicles enhanced their internalization by BMDMs. This could be competed away by co-administration of the ManNPs with 100 mg/mL of free D-mannose. Brightness & contrast were enhanced in the DAPI channel to account for small differences in staining between samples. FAM channels were left unaltered.

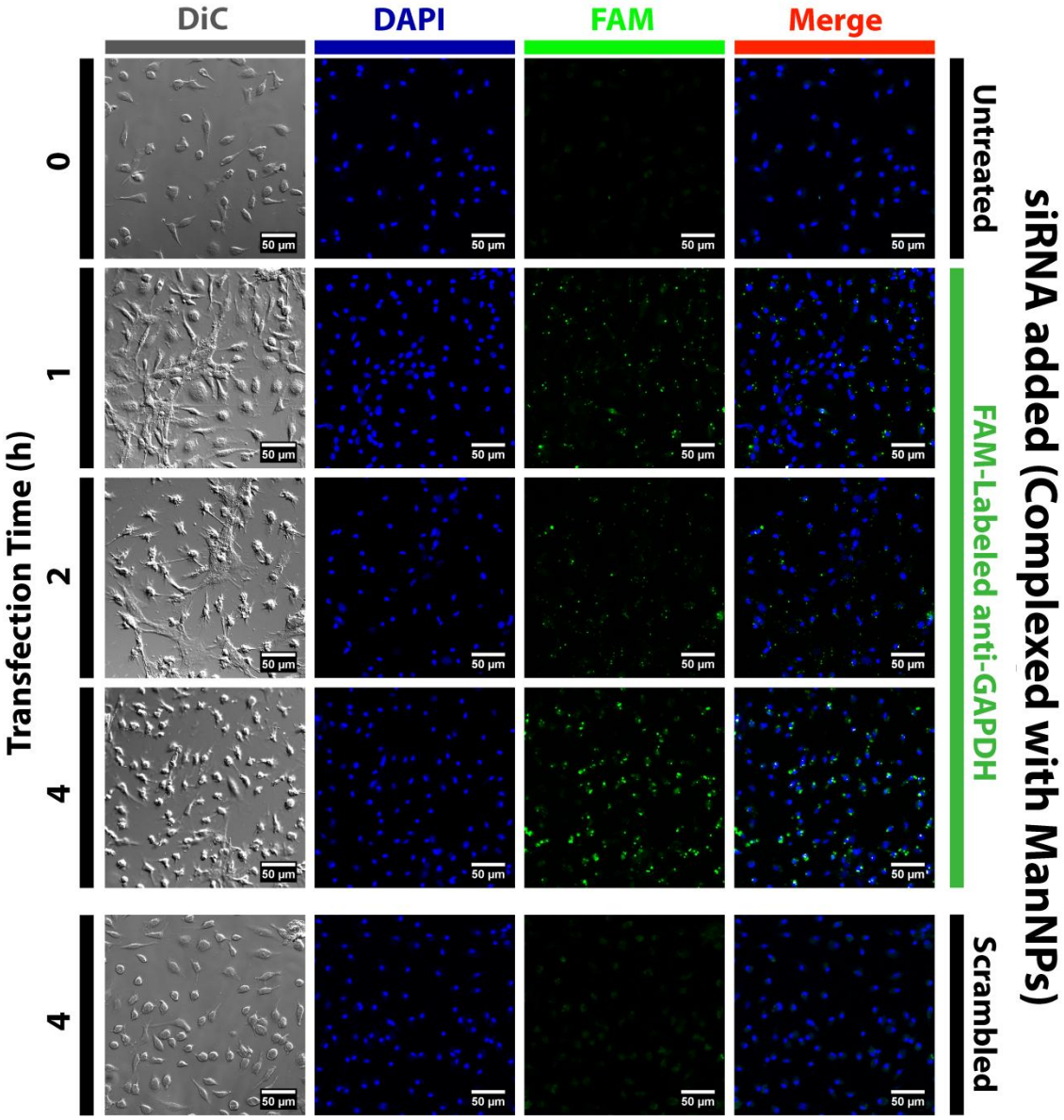

FIGURE 20. Kinetics of ManNP-Mediated siRNA Delivery into Primary Macrophages. BMDMs were transfected with FAM-siRNA (green; complexed into ManNPs) for 1-4 h prior to being fixed, stained with DAPI (blue), and imaged via confocal microscopy. (Scale bars = 50 µm). As a comparison, BMDMs treated with non-fluorescent, scrambled siRNA (complexed into ManNPs) have been shown. Brightness & contrast were enhanced in the DAPI channel to account for small differences in staining between samples. FAM channels were unaltered. Punctate green signal is observed within 1-2 h of administration, suggesting internalization of siRNA into vesicles. At 4h, the green fluorescence is more diffuse, consistent with endosomal escape of the siRNA into the cytosol.

The enhanced delivery of siRNA via the ManNPs also corresponded with significantly improved knockdown of target gene expression in BMDMs relative to non-transfected cells and cells treated with free siRNA (PPIB; Figure 21A; *$p < 0.05$). The commercially-available Lipofectamine RNAiMAX® transfection reagent was even more effective at facilitating the knockdown of PPIB expression, but was also cytotoxic at the 24 h time point used in this study. In spite of lower levels of siRNA delivery into the BMDMs relative to ManNPs (Figure 19), the diblock nanoparticles also facilitated a significant level of PPIB knockdown ($p = 0.06$ relative to ManNPs, via one-way ANOVA). This is likely due to the higher hemolytic activity of the diblock nanoparticles at endosomal pH ranges, relative to the ManNPs (Figure 21B).

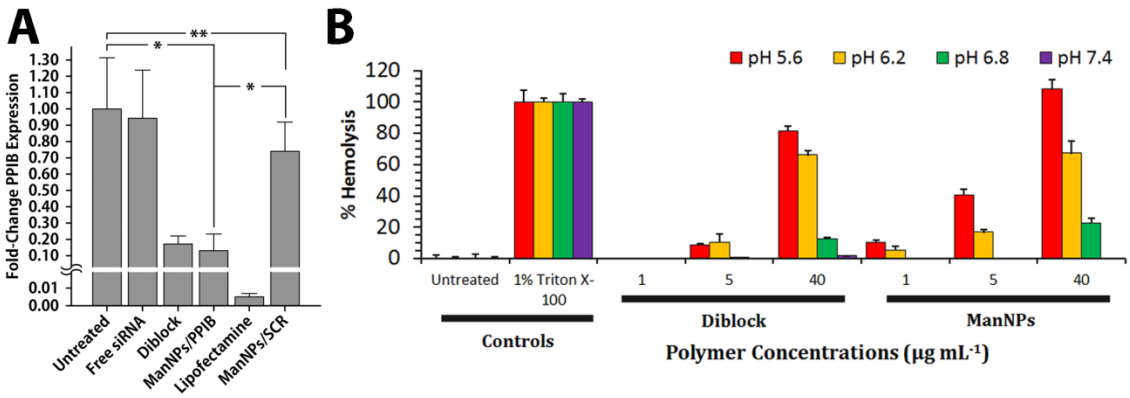

FIGURE 21. ManNPs Enhance Knockdown of PPIB Expression in BMDMs. (A) siRNA-mediated knockdown of PPIB expression by transfection vehicle. PPIB expression levels were quantified relative to the housekeeping gene GAPDH. qRT-PCR confirmed ManNPs carrying anti-PPIB siRNA mediated 87 ± 10% decrease in target gene expression following 24 h of treatment, relative to non-transfected (NT) cells. Error bars represent standard deviation of 3 independent experiments (*$p < 0.05$ by one-way ANOVA, **Not statistically significant). (B) Erythrocyte hemolysis assay showcases pH-responsive behavior of diblock nanoparticles and ManNPs. The block copolymers exhibit pH-dependent disruption of phospholipid membranes, and better facilitate erythrocyte lysis at pH < 6.8 . Error bars represent standard deviation of 4 independent experiments.

Discussion

Recently, polymers for siRNA delivery applications were described by Convertine et al., but these polymers lack cell specificity, due to their cationic corona (Convertine, et al., 2009). Other variants of these carriers have been recently developed that target folate receptor and CD22 (Benoit, et al., 2011; Palanca-Wessels, et al., 2011). In spite of the improved cell specificity of these constructs, their production required the use of more tedious, multi-step synthetic schemes (Benoit, et al., 2011; Henry, Convertine, Benoit, Hoffman, & Stayton, 2009) or expensive targeting motifs such as antibodies (Palanca-Wessels, et al., 2011). Furthermore, unlike the approach described herein, these approaches did not generate a generalized platform that can be utilized for "clicking" on alternative targeting agents. Because macrophage-specific siRNA delivery is the central goal of the current work, CD206 was evaluated as the target receptor, motivated by its expression primarily on macrophages and some dendritic cells (Taylor, et al., 2005).

Therefore, the first objective of this work was to develop a simple and rapid method for the immobilization of mannose onto micelle-forming polymeric siRNA carriers. Due to the presence of a number of reactive functional groups in the structure of the polymers, an orthogonal synthetic scheme was necessary to enable the synthesis of the desired block co-polymers, followed by site-selective functionalization with mannose in a final step. To accomplish this goal, we opted for a strategy involving the rapid and highly-efficient Huisgen 1,3-dipolar cycloaddition reaction, otherwise known as azide-alkyne 'click' chemistry (Figure 12).

Compared with other variants of the mannosylated carriers, our synthetic scheme yields the modular, molecularly-targeted siRNA delivery vehicles from less costly starting materials, and requires fewer reaction steps.

The terpolymer block confers pH-responsiveness to the final polymers because at pH 7.4, approximately 50% of the carboxylic groups on PAA and approximately 50% of the amine groups on DMAEMA are protonated, resulting in approximate charge neutrality of this block. Electrostatic and hydrophobic interactions enable this block to form a micelle core at pH 7.4, when it is covalently attached to a hydrophilic polymeric block. With decreasing pH, the PAA and DMAEMA become increasingly protonated, leading to a net cationic charge on this block that triggers micelle disassembly (Convertine, et al., 2009). The exposed terpolymer is hypothesized to disrupt endosomal and lysosomal membranes and ferry siRNA into the cytoplasm.

Diblock copolymers composed of a cationic DMAEMA component bound to this terpolymer were next synthesized (Figure 12B-C). Such polymers have been shown to facilitate the cytosolic delivery of siRNA and peptides into immortalized cell lines *in vitro* (Benoit, et al., 2011; Convertine, et al., 2009; Duvall, et al., 2010; Palanca-Wessels, et al., 2011). These 'base', diblock nanoparticles can enter many cell types because of their cationic surface charge, arising from the DMAEMA corona, which promotes interactions with the anionic cell membrane, triggering internalization (Kumari, Yadav, & Yadav, 2010).

The ManNPs retain the functional properties of the cationic DMAEMA component, endowing the micelles with the ability to complex siRNA and protect it

from nucleases that may be present in the *in vivo* environment (Figure 18). These properties are somewhat attenuated from those of the diblock copolymers, and is likely due to the morphology of the ManNPs, as the mannosylated corona may partially alter the properties of the underlying DMAEMA layer, including access of siRNA to binding through its cationic charge (Figure 16). Therefore, the ManNPs are likely to be slightly less amenable to complexation with siRNA than is the base diblock copolymer, which displays an outermost corona of DMAEMA. Nevertheless, the resulting ManNPs form multifunctional nanoparticles that display mannose on the surface, while veiling underlying structures designed to carry nucleic acids and other biologics into the cytosol of targeted cells.

The ManNPs show cell selectivity, and the data suggest that in a tumor environment where cancer cells coexist with a significantly smaller population of macrophages, the ManNPs will enter macrophages markedly faster than the cancer cells (Figure 18D). While this increased internalization rate was also observed for the non-targeted diblock copolymers, the effect was more enhanced for the mannosylated constructs. Despite significant levels of cytotoxicity at N:P ratios of > 4:1, these results were not surprising, as cationic transfection agents have been shown to exhibit charge-dependent cytotoxicity (Lv, et al., 2006). To counter this, all polyplexes for subsequent experiments were prepared at N:P ratios for which negligible cytotoxicity was observed at 24 h treatment time (Figure 18C). It is anticipated that the presented strategy for preferential macrophage targeting can be leveraged in diseases where infiltrating macrophages at pathologic sites exhibit upregulated CD206 expression, including cancer (Luo et al., 2006). Therefore,

ManNPs provide a promising platform for macrophage-specific delivery of RNAi therapeutics in pathologic sites.

The ManNPs also facilitated improved siRNA delivery into primary murine macrophages and generated robust knockdown of a model gene (Figures 18-21). The untargeted, diblock polymers also achieved potent gene knockdown despite delivering significantly lower amounts of siRNA into the macrophages. However, like the ManNPs, the diblock polymers are capable of efficiently escaping from the endosomal compartment in a pH-dependent manner, as modeled via the hemolysis assay (Figure 2G) (Evans et al., 2012). Therefore, even if the diblock copolymers are not as efficiently internalized into BMDMs as are the ManNPs, the diblock copolymers still deliver sufficient siRNA to cause significant levels of gene knockdown. This effect can depend on the potency of the siRNA sequence itself, as different siRNA sequences against the same target gene can exhibit widely different abilities to recognize the targeted mRNA sequence for knockdown (Rettig & Behlke, 2012).

Nevertheless, these results are significant because primary macrophages possess highly degradative phagocytic, endosomal and lysosomal compartments, providing a formidable barrier to the cytosolic delivery of siRNA (Stacey, et al., 1993). Moreover, these data suggest that the ManNPs and their cargo are interacting with an endocytotic receptor, leading to internalization of the complexes. The cargo is then able to escape the endosomal pathway, through a mechanism that is likely mediated by the pH-responsive, endosomolytic behavior of the terpolymer block within the ManNPs (Convertine, et al., 2009). Moreover, the data implies that the

targeted receptor is likely CD206, as it is known to effectively bind mannosylated substrates, resulting in internalization of the bound substrates via receptor-mediated endocytosis or phagocytosis (Stahl & Ezekowitz, 1998).

Summary

The data presented here showcase a novel strategy to selectively target TAMs. The capacity of this system for endosomal disruption enables biologics to be delivered into the cytosol, promoting their access to intracellular drug targets and processes. In a broader sense, this work is the first demonstration of a 'clickable' siRNA delivery platform that will enable the attachment of other targeting ligands to the azide-functionalized corona of pH-responsive, endosomolytic micelles. These strategies will potentially open up new areas in cancer immunotherapy, enabling selective intervention with the activities of TAMs while leaving surrounding cells relatively undisturbed.

CHAPTER IV

LEVERAGING PATHOLOGIC MACROPHAGE OXIDATIVE ACTIVITY FOR LOCALIZED DRUG DELIVERY VIA OLIGO(PROLINE) CROSS-LINKED POLYMERIC SCAFFOLDS

Chronic inflammation-mediated oxidative stress is a common mechanism of implant rejection and failure. Therefore, polymer scaffolds that can degrade slowly in response to this environment may provide a viable platform for implant site-specific, sustained release of immunomodulatory agents over a long time period. In this work, proline oligomers of varying lengths (P_n) were synthesized and exposed to oxidative environments, and their accelerated degradation under oxidative conditions was verified via high performance liquid chromatography and gel permeation chromatography. Next, diblock copolymers of poly(ethylene glycol) (PEG) and poly(ε-caprolactone) (PCL) were carboxylated to form 100 kDa terpolymers of 4%PEG-86%PCL-10%cPCL (cPCL = poly(carboxyl-ε-caprolactone); *i%* indicates molar ratio). The polymers were then crosslinked with bi-aminated PEG-P_n-PEG chains—where P_n indicates the length of the proline oligomer flanked by PEG chains. Salt-leaching of the polymeric matrices created scaffolds of macroporous and microporous architecture as observed by scanning electron microscopy. The degradation of scaffolds was accelerated under oxidative conditions, as evidenced by mass loss and differential scanning calorimetry measurements. Immortalized murine bone marrow-derived macrophages were then seeded on the scaffolds, and activated by adding γ-interferon and

lipopolysaccharide to cells throughout the 9-day study period. This treatment promoted the release of H_2O_2 by the macrophages, and the degradation of proline-containing scaffolds compared to the control scaffolds. The accelerated degradation was evidenced by increased scaffold porosity, as visualized through scanning electron microscoopy and X-ray microtomography imaging. The current study provides insight into the development of scaffolds that respond to oxidative environments through gradual degradation, for the controlled release of therapeutics targeted to diseases that feature chronic inflammation and oxidative stress (S. S. Yu, R. L. Koblin, et al., 2011).

Introduction

Abnormal changes in environmental parameters, such as temperature, pH, protease activity, or redox balance, have been documented in a wide array of pathophysiological conditions (Cammas et al., 1997; Galis, Sukhova, Lark, & Libby, 1994; Gupta, Vermani, & Garg, 2002; Halliwell, Clement, & Long, 2000; Scherer, McIntyre, & Matrisian, 2008). Therefore, the development of 'smart', synthetic biomaterials that are capable of responding specifically to changes in these environments holds promise in facilitating the programmed delivery of therapeutics and imaging contrast agents in a site and/or timing-specific way (Fattori & Piva, 2003; Schmedlen, Elbjeirami, Gobin, & West, 2003; Tanaka et al., 2009; Zhang, Srivastava, & Misra, 2007).

In particular, elevated levels of reactive oxygen species (ROS), such as H_2O_2 and O_2^-, are typically observed in the pro-inflammatory response to pathogens and

to implanted biomaterials. In the latter case, the chronic production of ROS has been a mechanism behind implant rejection and failure, necessitating follow-up implant replacement surgeries years after the original procedure. This phenomenon has been observed for a wide array of applications, including orthopedic, vascular, and neurological implant materials (Azuma & Tilney, 1994; Massia, Holecko, & Ehteshami, 2004; Moilanen et al., 1997). Consequently, ROS-responsive materials would be desirable as implant coatings for such applications, in order to facilitate controlled local release of inflammatory modulators and suppressors without off-target side-effects elsewhere in the body.

The first example of a ROS-responsive biomaterial was demonstrated by Napoli et al. using a poly(propylene sulfide)-(PPS) based system, which is initially hydrophobic but becomes oxidized into more hydrophilic sulfones by peroxides (Napoli, Valentini, Tirelli, Muller, & Hubbell, 2004). In this work, the authors self-assembled vesicles composed of PPS cores with hydrophilic poly(ethylene glycol) (PEG) coronas. Within a few hours of H_2O_2 addition, the vesicles exhibited a hydrophobic-to-hydrophilic transition—a behavior that can be leveraged for controlled release applications. These materials have now begun to see applications in immunobioengineering, leading to new vaccine nanoparticles that have been validated *in vivo* in mouse models (Reddy, Rehor, Schmoekel, Hubbell, & Swartz, 2006; Reddy et al., 2007; Thomas, et al., 2011). At the same time, it may also be desirable to produce materials that respond to oxidative environments with slower changes in material properties.

The accumulation of oxidatively modified proteins has been demonstrated as a hallmark of the aging process and also in certain diseases (Berlett & Stadtman, 1997; E. R. Stadtman & Berlett, 1997). Within such proteins, the amino acids histidine, proline, arginine, and lysine have been found to be particularly susceptible to oxidative processes (Amici, Levine, Tsai, & Stadtman, 1989). Further, the reaction of proline residues with environmental oxidants can lead to cleavage of the parent polypeptide chains at these sites (E. R. Stadtman & Levine, 2003).

Inspired by this work, we synthesized polymeric scaffolds crosslinked with proline oligomers and assessed their degradation following exposure to oxidative environments. As a backbone, we selected a terpolymer system composed of PEG, poly(ε-caprolactone) (PCL), and poly(carboxyl-ε-caprolactone) (cPCL). The selection of this terpolymer system was driven by the functional properties of each component, as the PEG provides hydrophilicity and reduces protein adsorption (Sung et al., 2010), the PCL provides elastic mechanical strength and hydrophobicity for cell adhesion (Sung et al., 2005), and the cPCL provides carboxylic groups that can be chemically crosslinked with biaminated species under mild conditions. Copolymers of *x* mol % PEG, *y* mol % PCL, and *z* mol % cPCL are identified as *x*%PEG-*b*-*y%*PCL-*co*-*z*%cPCL where PEG-PCL is a block copolymer but cPCL addition is random within the PCL subunit. The polymers are abbreviated *x*%PEG-*y*%PCL-*z*%cPCL. This new class of copolymers is designed provide tunable properties for biomedical applications as polymer properties are influenced by the molar ratios of the individual subunits and, by varying their aforementioned contributions, the resulting physical, chemical and mechanical properties can be controlled (Crowder,

Gupta, Hofmeister, Zachman, & Sung, 2011). In particular, the studies below used a 4%PEG-86%PCL-10%cPCL system, where the numbers include molar percentages of the individual units. PCL was chosen as the majority component because it has been shown to be minimally degraded in environments containing H_2O_2 over more than 20 weeks, requiring much stronger metal-catalyzed oxidative environments to produce any significant degradation within this time frame (Ali, Doherty, & Williams, 1994).

The proline oligomers Ac-KP_nK, in which *n* indicates the number of proline residues, were synthesized by standard Fmoc chemistry on a Rink amide resin to fashion two free amines for the coupling of Fmoc-PEG_{12}-COOH (MW = 500 Da). The oxidative degradation of the peptides with and without PEGylation was first assessed through gel permeation chromatography (GPC) and high performance liquid chromatography-mass spectrometry (HPLC-MS). Next, scaffolds of 4%PEG-86%PCL-10%cPCL were covalently crosslinked with PEG-P_n-PEG crosslinkers, and degraded in acellular and cellular *in vitro* models mimicking physiologic oxidative conditions. Oxidation-dependent changes in scaffold material properties and morphology were assessed via scanning electron microscopy (SEM), differential scanning calorimetry (DSC), and X-ray micro-computed tomography (μCT) imaging.

Materials and Methods

Materials

All reagents, including murine γ-interferon (IFNγ) and bacterial lipopolysaccharide (LPS), were purchased from Sigma-Aldrich (St. Louis, MO) and

used as purchased unless otherwise noted below. ε-caprolactone was purchased from Alfa Aesar (Ward Hill, MA). Fmoc-protected L-amino acids and resins for solid-phase peptide synthesis were purchased from EMD Biosciences (Gibbstown, NJ). RPMI-1640 medium, penicillin-streptomycin, and fetal bovine serum (FBS) were purchased from Invitrogen (Carlsbad, CA). 3-morpholinosydnonimine (SIN-1) was purchased from Invitrogen as packages of individual 1 mg aliquots. Dialysis filters were purchased from Thermo Fisher (Rockford, IL). All organic solvents, including *N,N*-dimethylformamide (DMF), *N*-methylpyrrolidone (NMP), tetrahydrofuran (THF) and methanol, were purchased from Fisher Scientific (Pittsburgh, PA) and used as purchased.

The ring-opening polymerization of ε-caprolactone is highly water-sensitive, and therefore, all monomers and reagents for this purpose were carefully dried before use. 15 g MeO-PEG (Mn = 5000 Da; ~3 mmol) was dissolved in 150 mL toluene and dried via a Dean-Stark trap at 130˚C under N_2 environment. The dried MeO-PEG was concentrated by distillation at 40 ˚C, precipitated in diethyl ether at -20˚C, then further dried *in vacuo*. In a separate vessel, 150 mL ε-caprolactone (161.7 g; 1.41 mol) was mixed with 2 g calcium hydride (47.5 mmol) overnight under N_2 gas. The product was distilled *in vacuo* at 70 ˚C, and stored under N_2 until use.

Synthesis of Biaminated PEG-P_n-PEG 'Crosslinkers'

The peptide sequences KPPPPPK (P_5), KPPPPPPPK (P_7), and KPPPPPPPPPPK (P_{10}) were synthesized via standard Fmoc-based solid phase methods on a Rink amide-MBHA resin (Figure 22). The peptides were then acetylated in excess acetic

anhydride for 4 h, prior to cleavage in a 95:5:3:2 mixture of trifluoroacetic acid : thioanisole : ethanedithiol : anisole for 2 h. The liberated peptide was precipitated in diethyl ether and lyophilized to form a dense, white powder. All peptides were at least 70% acetylated as determined by HPLC-MS, therefore, containing only two amine groups for downstream coupling, which are located on the lysine residues. As a result of incomplete acetylation of the peptides, the remaining < 30% of peptide also contained a third amine group responsible for the N-terminus of the peptide chain.

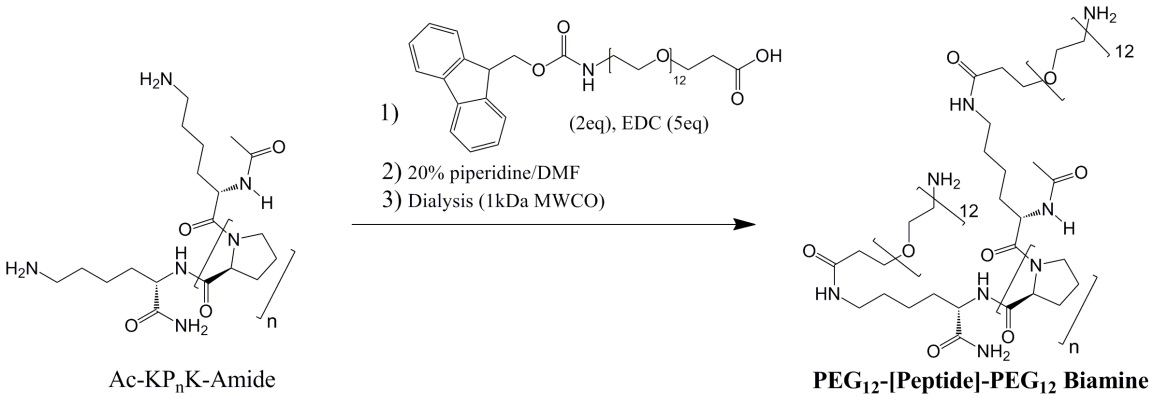

FIGURE 22. Synthesis of Biaminated PEG-P$_n$-PEG Crosslinkers.

Fmoc-PEG$_{12}$-COOH (EMD Biosciences) was then coupled to the peptides via standard carbodiimide chemistry.(Hermanson, 2008 (2nd ed.)) Removal of the Fmoc-protecting group was achieved via 20% piperidine in DMF, followed by dialysis of the completed crosslinkers in 1 kDa MWCO membranes for 48 h against nanopure water. Lyophilization of the retentate yielded a white, fluffy powder that was stored at -20°C until use.

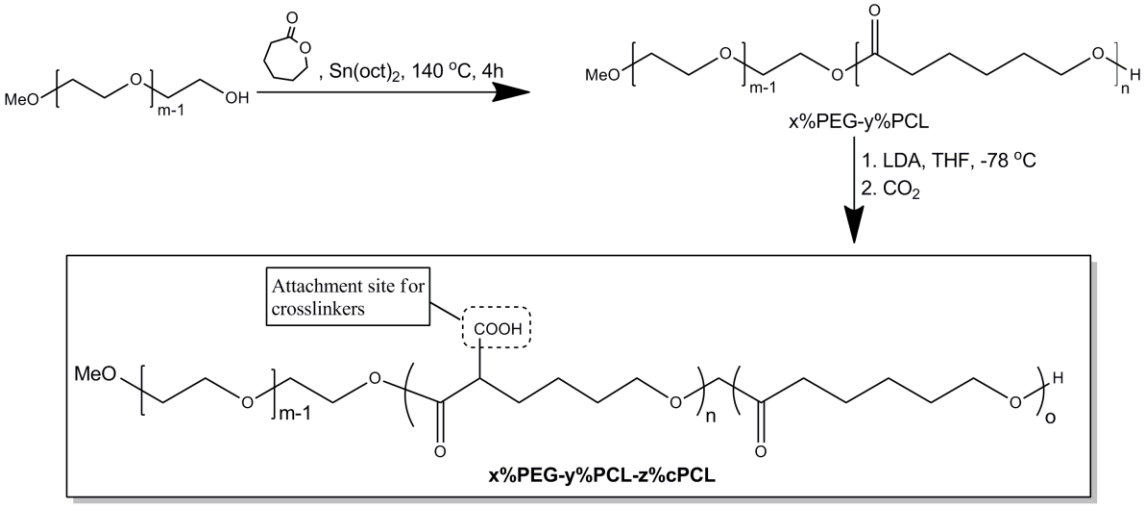

FIGURE 23. Synthesis of *x*%PEG-*y*%PCL-*z*%cPCL Backbone Polymers.

Synthesis of 4%PEG-86%PCL-10%cPCL 'Backbone' Polymers

To synthesize *x*%PEG-*y*%PCL block copolymers (Figure 23), 0.4 g dried MeO-PEG (0.08 mmol) was added to a round bottom flask. The flask was capped with septum, heated to 40°C, and degassed with repeated cycles of evacuation followed by equilibration with N_2. Next, 9.4 g ε-caprolactone (82 mmol) and 17.9 mg of tin 2-ethylhexanoate (44.2 μmol) in 500 μL toluene were injected sequentially into the reaction vessel. The polymerization was carried out at 140°C for 4 h. The resultant 100 kDa 4%PEG-96%PCL was cooled to room temperature, dissolved in 200 mL methylene chloride, precipitated in diethyl ether, and dried *in vacuo*.

The formation of *x*%PEG-*y*%PCL-*z*%cPCL was carried out via random carboxylation of the *x*%PEG-*y*%PCL diblock copolymers. 8.57 g of 4%PEG-96%PCL was evacuated in a round bottom flask for 1 h, and then dissolved in 300 mL anhydrous THF. The solution was cooled to -78°C, and 37.5 mL 2 M lithium

diisopropylamide (LDA; 75 mmol) was injected drop-wise by syringe. This reaction proceeded for 30 min at -78°C. In a separate Schlenk flask, CO_2 was generated through the reaction of concentrated sulfuric acid with sodium carbonate, and dried through a column filled with molecular sieves and sodium hydride. The resulting dry CO_2 was bubbled through the 4%PEG-96%PCL/LDA reaction for 30 min at -78°C, during which the reaction exhibits a color change from orange to white. The solution was then brought to room temperature, and 150 mL of 1 M ammonium chloride was added drop-wise. The solution was then neutralized by drop-wise addition of hydrochloric acid. The crude product was extracted with 500 mL of methylene chloride, and the pooled organic fractions were concentrated via rotary evaporation. 4%PEG-86%PCL-10%CPCL was precipitated in diethyl ether and dried *in vacuo*. ^{1}H NMR (400 MHz; $CDCl_3$): δ 9.25 (s, <1 H, COO**H**), 4.06 (t, 2H, -OC**H₂**), 3.4 (m, 1H, - C**H**-COOH), 2.31 (t, 2H, -C**H₂**), 1.66 (m, 4H, -C**H₂**), 1.5 (m, 2H, -C**H₂**), 1.37 (m, 2H, -C**H₂**).

Scaffold Fabrication

0.3 g of the 4%PEG-86%PCL-10%cPCL terpolymers were dissolved in 3 mL of ice cold CH_2Cl_2, and was followed by the addition of 67 mg of crosslinkers and 12 mg of *N*-ethyl-*N′*-(3-dimethylaminopropyl) carbodiimide hydrochloride (EDC). For control scaffolds, 2 kDa PEG-dihydrazide (Laysan Bio, Arab, AL) was used in place of the PEG-P_n-PEG crosslinkers. After vortexing this mixture vigorously, the solution was poured into a Teflon dish 5 cm in diameter, containing 10 g of pre-sieved NaCl crystals (212-425 μm). This mixture was manually mixed vigorously to spread the

salt crystals evenly throughout the pre-polymer, and then the pre-polymer was evenly spread throughout the bottom of the Teflon dish. The pre-polymer was allowed to crosslink over ice for 30 min. Next, the polymers were immersed in liquid N_2 for 2 minutes and lyophilized overnight to remove all traces of organic solvents. The removal of excess byproducts, salts, and reagents was achieved by salt-leaching the scaffolds in nanopure water over 5 days. Water was changed daily. Finally, the completed scaffolds were dried *in vacuo* overnight at room temperature, and weighed prior to use in any experiments. Wet masses of the scaffolds were measured after allowing scaffolds 3 days to swell to equilibrium. Swollen scaffolds were blotted dry to remove excess buffer before weighing. Swelling ratio was calculated according to the formula [Swelling ratio] = (Wet mass)/(Dry mass).

Oxidation Experiments and Chromatography

To investigate oxidative degradation, peptide crosslinkers were incubated in 1 mg/mL in phosphate-buffered saline (PBS, pH 7.4) at 37°C, and then H_2O_2 and $CuSO_4$ were added to the samples to final concentrations of 5 mM H_2O_2 and 50 μM Cu(II). Peptide crosslinkers that were incubated in the absence of H_2O_2 and $CuSO_4$ served as a control. Reactions were incubated in the dark at 37°C until they were ready for analysis, at which point they were frozen at -20°C.

For scaffold degradation experiments, dry scaffolds were weighed before incubation then allowed 3 days to swell to equilibrium in PBS prior to the beginning of the experiment. From here, scaffolds were incubated in PBS with or without 1 mM SIN-1 for 28 days. Buffers were changed daily owing to the relatively short half-

life of SIN-1 in aqueous environments (< 10 h). At days 3, 7, 14, and 28 post incubation, scaffolds were dried *in vacuo* overnight prior to re-weighing and further characterization.

GPC was performed by injecting samples into three serial Tosoh Biosciences TSKGel Alpha columns (Tokyo, Japan), operated at 60°C. For various experiments, water or DMF with 0.1 M LiBr were used as mobile phases. Chromatograms were recorded via a Shimadzu SPD-10A UV detector and RID-10A refractive index detector (Shimadzu Scientific Instruments, Columbia, MD), and a Wyatt miniDAWN Treos multi-angle light scattering detector (MALS; Wyatt Technology, Santa Barbara, CA). Data acquisition and analysis was performed on Wyatt ASTRA software (version 5.3.4).

Analytical high performance liquid chromatography-mass spectrometry (HPLC-MS) was performed on an Agilent 1200 series system equipped with UV detection at 215 and 254 nm and a 6130 quadrupole mass spectrometer with electrospray ionization (Agilent Technologies, Santa Clara, CA). On-line evaporative light-scattering detection was also activated for some samples (Varian, Santa Clara, CA). C18 columns were purchased from Phenomenex (Kinetex 2.1 x 5.0 mm; Torrance, CA), and run with a gradient of 10-95% acetonitrile (over 2 min) in 0.1% trifluoroacetic acid in water.

Scanning Electron Microscopy (SEM)

SEM was performed on a Hitachi S-4200 system (Tokyo, Japan). An accelerating voltage of 2 kV was used for all images. To prepare scaffolds for

imaging, scaffolds were sputter-coated with gold (Cressington Sputter Coater 108, Watford, United Kingdom) at a plasma current of 30 mA for 120 seconds.

Differential Scanning Calorimetry (DSC)

All polymeric scaffolds were analyzed for thermal transitions and heat capacity via DSC (TA Instruments, Newcastle, DE). Samples were weighed (2-5 mg), and sealed within aluminum sample pans with tops. The measurement procedure included two temperature sweeps from -80°C to 100°C at a ramp rate of 10°C/min. The values from the second sweep were reported such that thermal history was erased.

Cell Studies

For cell studies, immortalized bone marrow-derived macrophages (BMDMs) were generated from NGL (**N**F-κB-**G**FP-**L**uciferase construct) transgenic mouse lines on C57Bl6/DBA background (NGL-BMDMs), and were provided by the laboratory of Dr. Fiona E. Yull (Vanderbilt-Ingram Cancer Center, Nashville, TN) (Everhart et al., 2006). NGL-BMDMs were grown in high-glucose (4.5 g/L) DMEM containing 4 mM L-glutamine, and further supplemented with 10% (v/v) FBS and 1% (v/v) penicillin-streptomycin. All cells were cultured at 37°C in a 5% CO_2 incubator.

For all experiments, NGL-BMDMs were detached from flasks by gently rinsing the confluent monolayers with serum-free medium (high-glucose DMEM with 4 mM L-glutamine, 1% penicillin-streptomycin, 1X non-essential amino acids, and 1X MEM vitamins), counted via a Coulter Counter (Beckman Coulter, Miami, FL),

and seeded into scaffolds or directly to 24-well plates at a density of 300,000 cells/cm^2. Cells were allowed 24 h to associate with scaffolds or well plates before further experimentation. The serum-free medium was used in the course of the experiment to minimize serum-induced changes in macrophage activation states.

For pro-inflammatory activation, NGL-BMDMs were treated with 50 ng/mL IFNγ and 10 μg/mL LPS in serum-free medium. In order to maintain a high level of macrophage activation, media containing these activators was replaced daily for the duration of the experiments.

Micro-Computed Tomography (μCT) Imaging of Scaffolds

To analyze the porosity and the distribution of pore size in the scaffolds, portions of each scaffold were imaged using a μCT50 (Scanco Medical, AG, Switzerland) and the manufacturer's software. Images of an approximately 6 mm wide by 10 mm long section of each sample were acquired with an isotropic voxel size of 1 μm at 45 kV, 200 μA, 1000 projections per rotation, and an integration time of 1 sec without beam filtering and using the default beam hardening correction. Three different scaffolds were imaged per experimental condition (n=3). The low X-ray attenuation of the scaffolds was offset by the extremely low noise produced by the extended acquisition protocol which maintained signal-to-noise ratio sufficient for threshold based segmentation of scaffold from internal pores. A cylinder of 1355 μm in diameter and 500 μm long was selected as the volume of interest in each sample. After creating a z-stack of the individual slices, the volume of interest (VOI) was extracted and the threshold and noise filter applied to extract the 3D pore

structure from the grey-scale images. The mean pore diameter and distribution of the pore diameters within each scaffold was calculated using standard, accepted ball filling method reported elsewhere (Hildebrand & Ruegsegger, 1997; Ruegsegger, Hildebrand, Laib, Muller, & Dequeker, 1999). By distance transformation, the calculation of the metric distance of every pore voxel to the nearest pore-matrix interface is understood. These distances can be imagined as the radius of a sphere with center in this voxel that fits inside the pore. Redundant spheres are removed such that big spheres incorporate small, encompassed spheres. The result is the mid-axes transformed structure with the centers of maximal spheres filling the pore completely. To calculate pore thickness, each voxel then gets the value of the radius of the maximal sphere it sits within.

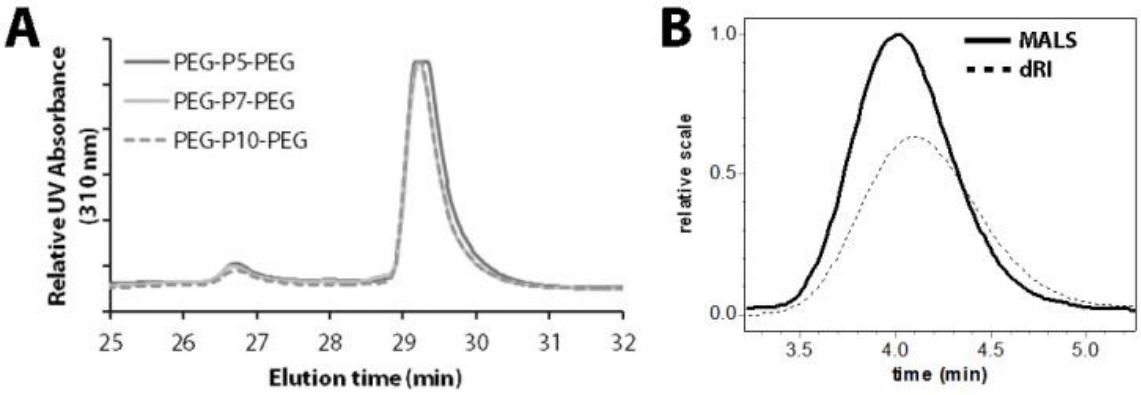

FIGURE 24. GPC chromatograms of the oxidation-responsive scaffold components. (A) PEG-P_n-PEG crosslinkers (10 mg/mL in DMF + 0.1M LiBr) prior to final Fmoc deprotection are detectable via a UV detector set at 310 nm. The presence of a small, earlier-eluting hump at ~27 min represents the tri-PEGylated peptides due to incomplete acetylation of the peptide sequences. The major peak at 29-30 min is the major, bi-PEGylated product. (B) The 4%PEG-86%PCL-10%cPCL backbone (10 mg/mL in THF) is relatively monodisperse, as evidenced by the near-complete overlap of the MALS and differential refractive index (dRI) chromatograms. With the dn/dc of the terpolymer measured at 0.0663 mL/g in THF, the molecular weights were calculated at M_n = 99.4 kDa and M_w = 115 kDa (PDI = 1.16).

Results

Synthesis and Characterization of PEG-P_n-PEG Crosslinkers and 4%PEG-86%PCL-10%cPCL Backbone

The two major components of the scaffolds were synthesized via well-characterized methods as described, and characterized by GPC (Figure 24). The crosslinkers primarily consisted of bi-PEGylated proline oligomers, as evidenced by the predominant peak at 29.5 min, but also included smaller amounts of tri-PEGylated proline oligomers, as indicated by the earlier-eluting peak between 26-27 min. The presence of this minor peak is due to incomplete acetylation of the peptide prior to coupling of the PEG sequences. Nevertheless, all three crosslinker sequences exhibited similar sizes, as indicated by their overlapping chromatograms.

The terpolymer backbone was synthesized via the polymerization of ε-caprolactone onto a PEG-based macroinitiator, followed by random carboxylation of the PCL block (Gimenez, Ponsart, Coudane, & Vert, 2001). This scheme led to a relatively monodisperse terpolymer of M_n = 99.4 kDa and M_w = 115 kDa (PDI = 1.16), as measured via GPC-MALS. The terpolymer exhibited a dn/dc of 0.0663 mL/g in THF and was poorly soluble in methanol, DMF, and *N*-methylpyrolidone—characteristics that are consistent with the primarily PCL composition of the terpolymer (An & Cho, 2004).

H_2O_2-Mediated Degradation of P_n Peptides and PEG-P_n-PEG Crosslinkers

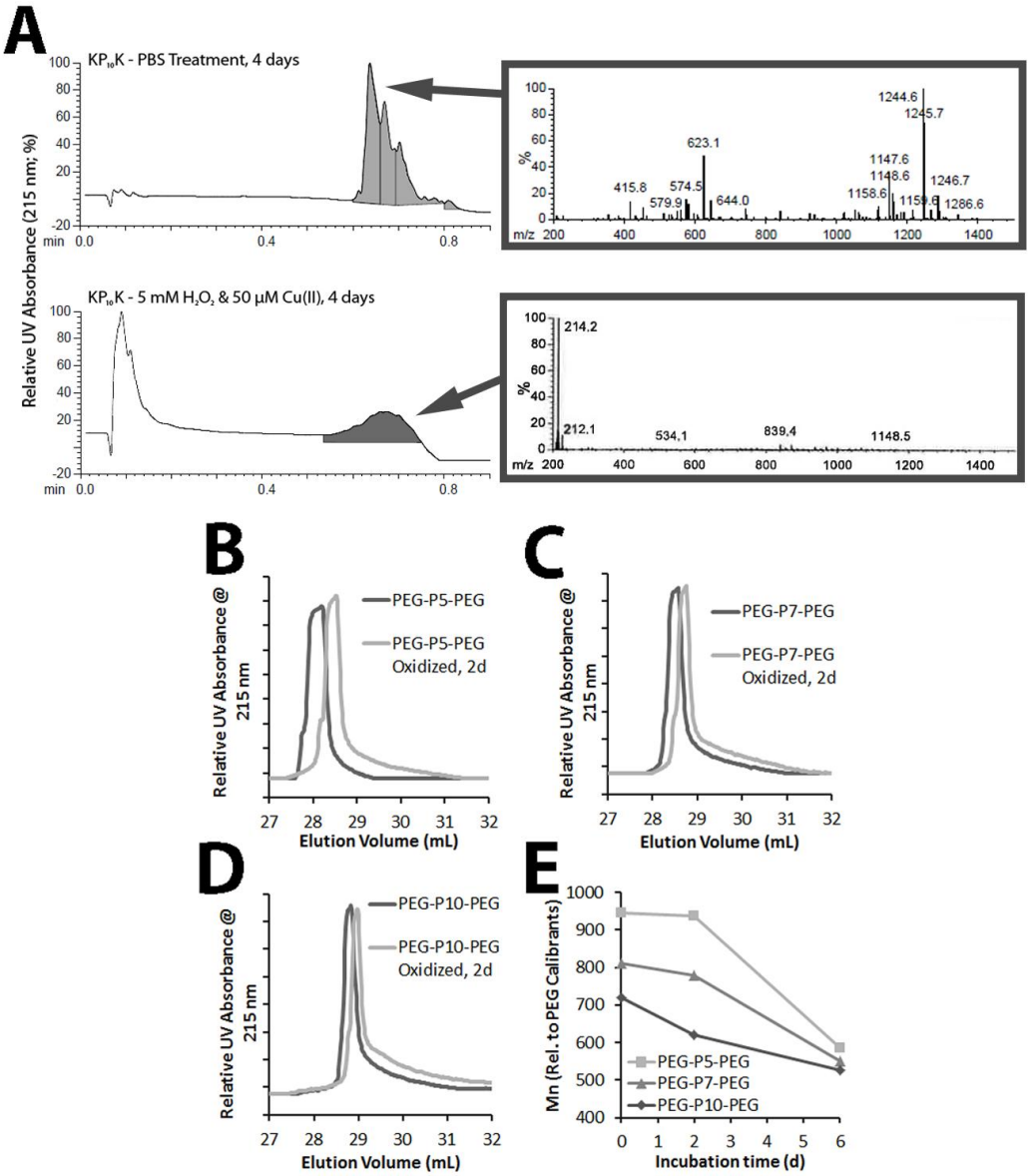

FIGURE 25. Metal-catalyzed oxidation of proline oligomers. (A) P10 was incubated at 37°C for 4 days in PBS only or PBS containing H2O2 and Cu(II), then analyzed via HPLC-MS. The latter treatment resulted in the disappearance of chromatograms and mass spectra characteristic of the intact peptide. To further confirm oxidative degradation of the peptide, PEG-Pn-PEG was incubated under the same conditions prior to analysis via GPC (B-E). In all cases, these molecules eluted at later times following only 2 d in the oxidative environment. (E) Peak molecular weights were calculated based on elution time, relative to monodisperse PEG standards. Within the first 2 d of treatment, degradation rate was proportional to the length of the proline oligomers. Further, all crosslinkers degraded to form a 550 Da product within 6 d, which is consistent with the molecular weight of the PEG reagent that was coupled to both ends of the peptides used in the study, to form the PEG-Pn-PEG crosslinkers for the scaffolds.

The susceptibility of the peptide components to oxidative cleavage was validated at multiple intermediate steps in the scaffold synthesis, starting from the completed peptides. In this way, the oxidation-responsiveness of the scaffolds can be attributed primarily to the peptide components and not any other polymeric components.

To begin, as-synthesized proline oligomers were incubated in PBS at 37°C, with or without the mediators of metal-catalyzed oxidation (MCO). The samples were then analyzed by HPLC-MS to detect the presence of peptides and degradation byproducts (Figure 25). In particular, after four day incubation in the MCO environment, the P_{10} oligomers demonstrated significant changes in their UV chromatogram within the elution time regions specific for the intact peptide, as well as the concomitant disappearance of MS peaks at 1244 and 623 m/z that are characteristic of the intact peptide. These phenomena were not observed for reactions that were incubated at room temperature for the same time period (data not shown), indicating that physiological temperature is required to induce the oxidative cleavage of peptides.

To confirm the oxidation-induced cleavage of the peptides, the PEG-P_n-PEG crosslinkers were incubated under the same conditions, and analyzed by GPC. In all cases, MCO-treated crosslinkers eluted later than untreated crosslinkers, indicating a decrease in the hydrodynamic size of these crosslinkers following oxidative treatment. Further, the average molecular weights of the crosslinkers were calculated relative to monodisperse PEG standards, and within the first two days of MCO treatment, the degradation rate of the crosslinkers was proportional to the

length of the proline oligomers contained within the crosslinkers. Moreover, after six days of MCO treatment, the molecular weights of the different crosslinkers converged on 550 Da, the molecular weight of the PEG component flanking each end of the peptides, indicating the complete degradation of the proline component of the crosslinkers.

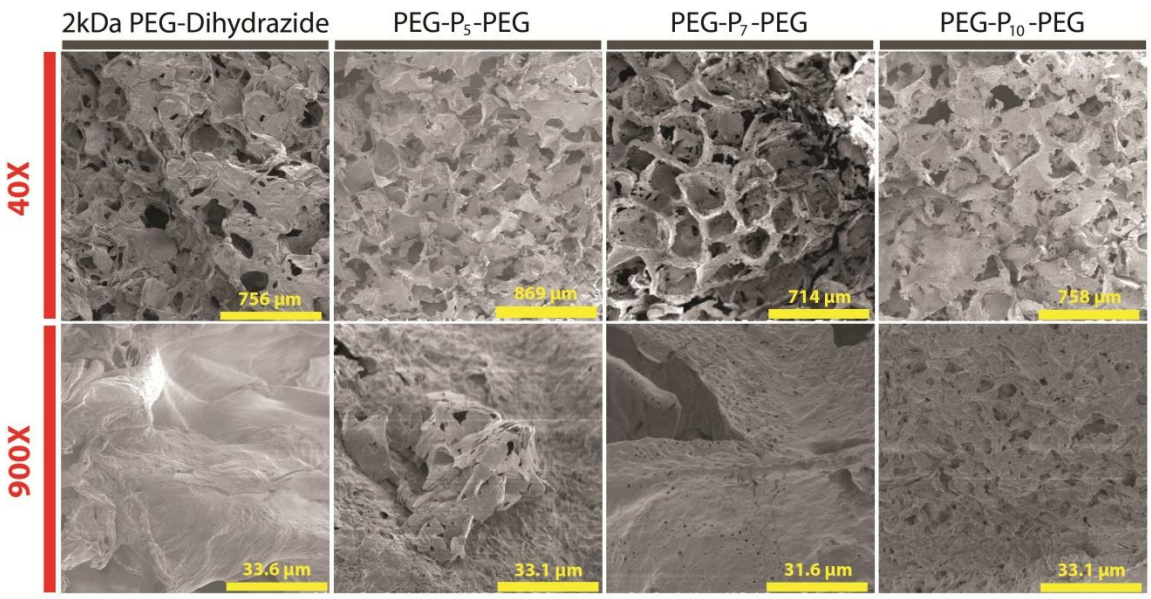

FIGURE 26. SEM of scaffolds of 4%PEG-86%PCL-10%cPCL by crosslinker type. Two different magnifications showcase macropores of > 100 µm diameter (top row) and micropores of < 10 µm in diameter (bottom row). Only the PEG-dihydrazide-crosslinked scaffolds failed to show any widespread microporous architecture. Macropores were templated into the polymer network through a salt-leaching procedure, while micropores were generated through the phase separation of the water generated during the crosslinking reaction from the hydrophobic solvent used to dissolve the pre-polymer.

Fabrication and Characterization of Crosslinked 4%PEG-86%PCL-10%cPCL Terpolymer Scaffolds

Polymeric scaffolds exhibiting macroporous and microporous architecture were fabricated using a procedure adapted from previous methods (Sung et al.,

2008). The completed scaffolds were morphologically examined via SEM (Figure 26). By dissolving the pre-polymer mixture in a hydrophobic solvent, the condensation of water due to the amine-carboxylic acid crosslinking reaction results in the phase separation of water from the bulk solvent, producing micropores (diameter < 10 μm) in the polymer network. Macropores of > 100 μm in diameter were templated into the polymer network by performing this crosslinking reaction in a bed of pre-sieved NaCl salt crystals. While all scaffold types appeared morphologically similar, PEG-dihydrazide-crosslinked scaffolds produced noticeably fewer micropores.

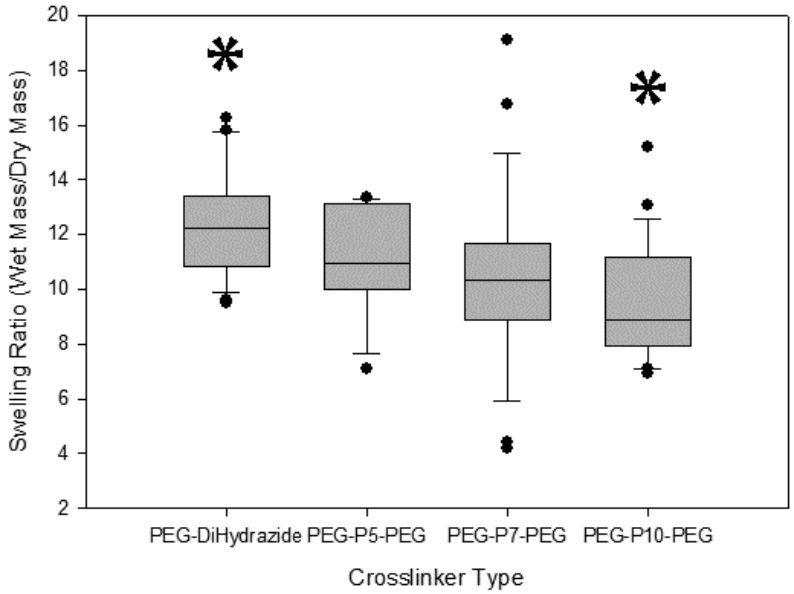

FIGURE 27. Swelling ratios of 4%PEG-86%PCL-10%cPCL scaffolds by crosslinker type. Upper and lower ends of boxes represent the 25th and 75th percentiles, respectively. Solid lines represent the median swelling ratios. Whiskers indicate 90th and 10th percentiles, and dots indicate outliers. The ability of the scaffolds to retain water was somewhat related to the length of the proline oligomer used as a crosslinker. PEG-P10-PEG-crosslinked scaffolds retained significantly less water than PEG-dihydrazide-crosslinked scaffolds (*$p < 0.05$, $n = 24$). Differences in swelling ratios versus the other two scaffold types were not statistically significant.

To examine if this was due in part to the hygroscopic nature of PEG-dihydrazide, swelling ratios of the scaffolds were measured as a function of the crosslinker employed. Due to the primarily PCL composition of the polymers, the resulting scaffolds exhibited swelling ratios that were on the order of 10x lower than those typically exhibited by hydrogels (Figure 27). However, the swelling ratios can be controlled to some extent by varying the length of the oligo(proline) peptide used in the crosslinker. PEG-dihydrazide, PEG-P_5-PEG, PEG-P_7-PEG, and PEG-P_{10}-PEG-crosslinked scaffolds exhibited swelling ratios of 12.4 ± 1.9 (n = 24), 11.1 ± 1.9 (n = 12), 10.4 ± 3.2 (n = 24), and 9.5 ± 2.1 (n = 24), respectively. Across these four groups, only PEG-dihydrazide versus PEG-P_{10}-PEG exhibited statistically significant differences in hydration ($p < 0.05$).

We also attempted the fabrication of the scaffolds using other solvents to dissolve the pre-polymer, including N-methylpyrrolidone (NMP), THF, and toluene. When NMP is used, the resulting scaffolds completely disintegrate into small clumps during the salt-leaching process. This is consistent with the poor solubility of PCL in NMP, and suggests that widespread crosslinked polymer networks were not successfully formed under these conditions. Toluene and THF both solubilized the pre-polymer, and produced crosslinked, macroporous scaffolds following salt-leaching. However, examination of these scaffolds via SEM failed to show any micropores in the resulting polymer network.

Overall, these results suggest the successful formulation of widespread crosslinked polymeric scaffolds of relatively uniform macroporous and microporous

architecture, via the methods described above. The scaffolds are also capable of absorbing about ten-fold their dry mass in water.

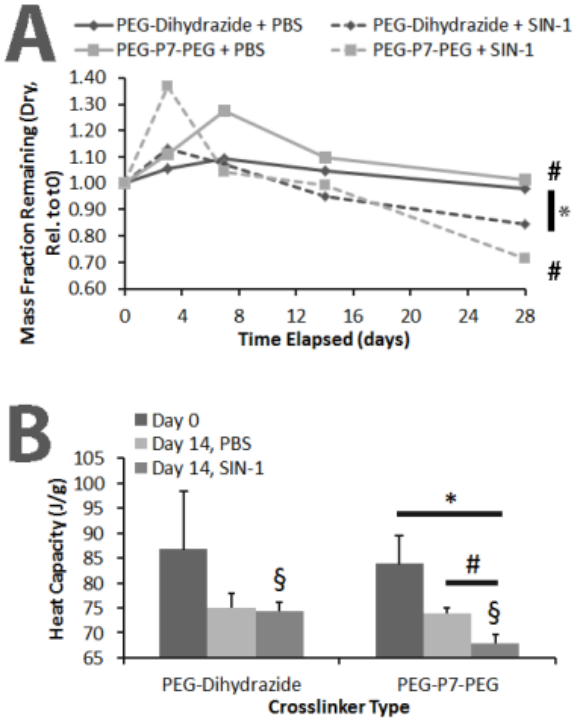

FIGURE 28. Accelerated degradation of terpolymer scaffolds crosslinked with PEG-P_7-PEG crosslinkers. Scaffolds crosslinked with PEG-dihydrazide or PEG-P_7-PEG were soaked in PBS or PBS + 1 mM SIN-1 for 28 days. (A) At each time point, scaffolds were dried and massed. The average remaining mass fraction of each scaffold is calculated by dividing dry mass following treatment, by dry mass at the beginning of the study. Scaffolds containing both crosslinker types experienced some degree of oxidative degradation, but PEG-P_7-PEG-crosslinked scaffolds lost more mass under oxidative conditions (#,* $p < 0.05$, $n = 3$). (B) Heat capacity of scaffolds for the melting point transition following 14 d treatment was measured via DSC. Error bars represent standard deviation of 3 independent experiments (# $p < 0.01$, $n = 3$; * $p < 0.05$; § $p < 0.05$).

ROS-Mediated Oxidative Degradation of Crosslinked Scaffolds

Because control PEG-dihydrazide-crosslinked scaffolds and PEG-P_7-PEG-crosslinked scaffolds demonstrated similar morphology (Figure 26) and insignificant difference in swelling ratios, these two scaffold types were selected for

further study. To verify that the proline crosslinkers can accelerate the degradation of the scaffolds under oxidative conditions, scaffolds were soaked for up to 28 d at 37°C in buffer with or without 1 mM of the ROS generator SIN-1. SIN-1 is typically known to produce nitric oxide and superoxide simultaneously, which can further lead to the generation of peroxynitrite and hydroxyl radicals *in situ* (Hogg, Darley-Usmar, Wilson, & Moncada, 1992). At each time point, scaffolds were dried and weighed.

Whereas the dry mass of scaffolds soaked in PBS only did not change significantly over the 28 d incubation period, both scaffold types underwent significant degradation within the oxidative environment (Figure 28). Under oxidative conditions, PEG-dihydrazide-crosslinked scaffolds retained 85 ± 5% of their mass following 28 d of treatment, while PEG-P_7-PEG-crosslinked scaffolds retained 72 ± 18% of their mass (n = 3). Neither scaffold completely degraded in this time frame. This can be attributed to the composition of the scaffolds, which is ~82% terpolymer by weight.

The oxidative degradation of both scaffold types was further characterized by DSC. These results showed that all scaffolds exhibited melting points at 53-56°C regardless of treatment duration and type or crosslinker. However, the oxidative degradation of the PEG-P_7-PEG scaffolds resulted in significantly decreased heat capacities during this phase transition (67.8 ± 1.8 J/g, n = 3), relative to PBS only-treated scaffolds (73.8 ± 1.2 J/g). This difference was not seen for the correspondingly treated PEG-dihydrazide-crosslinked scaffolds (75.0 ± 3.0 J/g in PBS versus 74.4 ± 1.6 J/g in SIN-1). Further, following 14 d of treatment with SIN-1

in PBS, all scaffolds exhibited significantly lower heat capacities, as compared to their day 0, untreated counterparts. This phenomenon is attributable to hydrolysis of the polymer networks, which can occur throughout the incubation period.

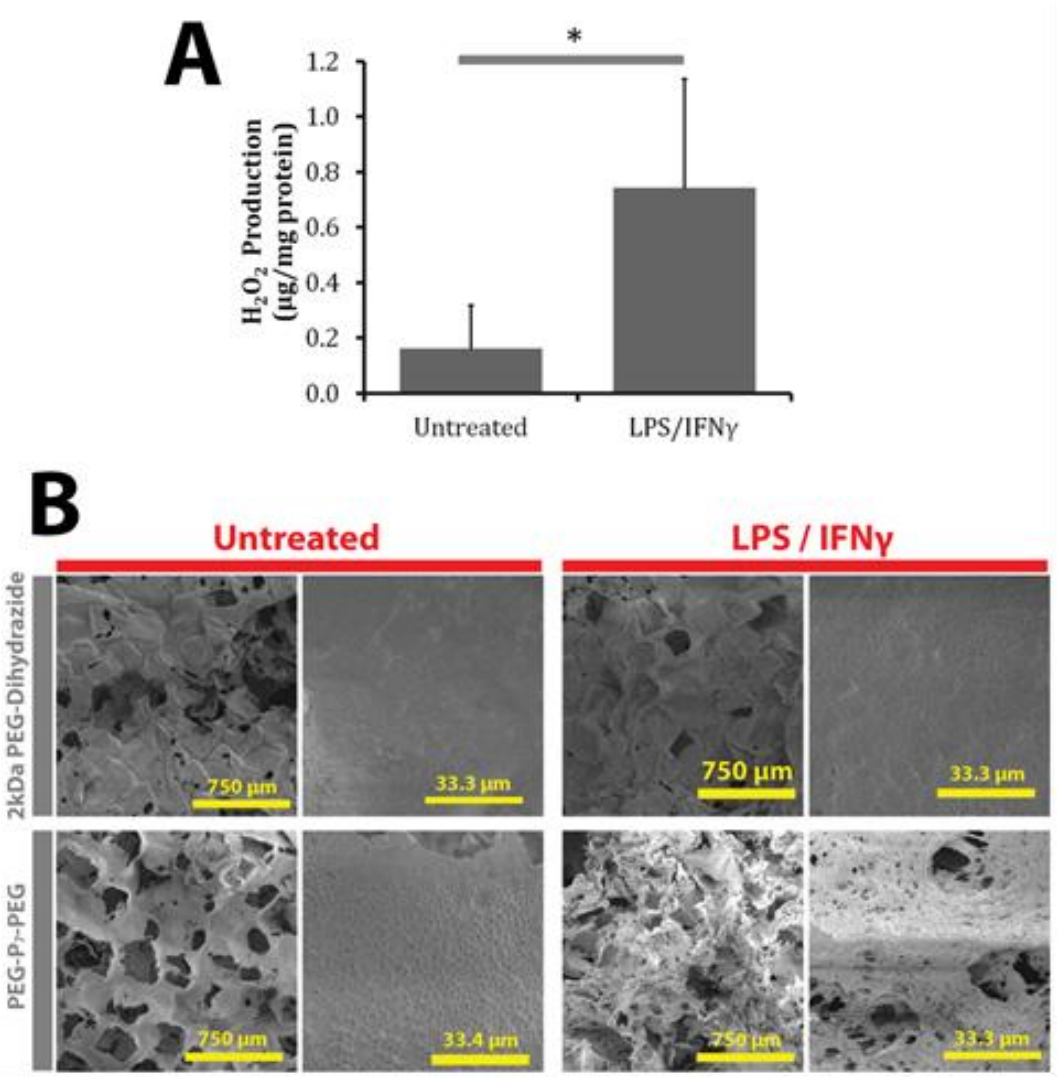

FIGURE 29. LPS/IFNγ-activated BMDMs exhibited H_2O_2-dependent degradation of PEG-P_7-PEG-crosslinked scaffolds. (A) Immortalized murine BMDMs cultured in tissue culture plates for 24 h in the presence of 50 ng/mL IFNγ and 10 µg/mL LPS produced higher levels of H2O2 per cell (H2O2 production normalized to cell number indirectly via protein assay), relative to untreated BMDMs (*$p < 0.05$, $n = 3$). (B) SEM images (40x and 900x) of scaffolds incubated with untreated or activated BMDMs for 9 d. Only PEG-P7-PEG-crosslinked scaffolds incubated with activated BMDMs exhibited the appearance of widespread pitting and < 10 µm pores in the polymer network.

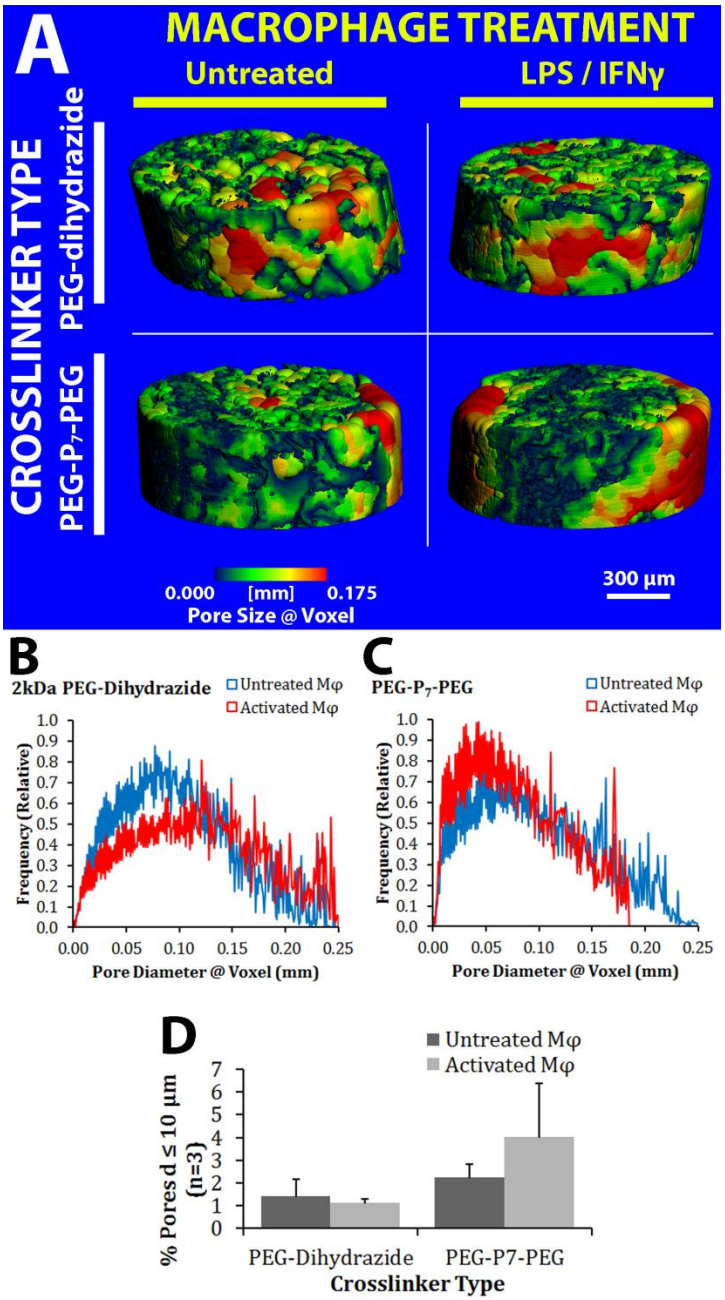

FIGURE 30. µCT imaging of scaffolds incubated with NGL-BMDMs (Mφ). Isotropic voxel size = 1 µm. (A) 3D pore diameter heat maps of scaffolds following incubation with untreated or activated (LPS/IFNγ-treated) BMDMs for 9 d. (B-C) Pore diameter histograms for scaffolds by crosslinker and treatment (average of n = 3 independent experiments). (D) From these histograms, a range of pore diameters (0-10 µm) was gated as an ROI, and the cumulative percentage of voxels containing pores of diameters within this range was plotted versus crosslinker type and treatment method. Consistent with the intended drug delivery function of this scaffold, the PEG-P_7-PEG-crosslinked scaffolds experienced an increase in the appearance of small pores ≤ 10 µm in diameter. These results are consistent with SEM observations demonstrating the appearance of micropores and pits in these polymer matrices, as well as the widespread disintegration of the macroporous scaffold structure as shown in (A).

Macrophage-Mediated Oxidative Degradation of Crosslinked Scaffolds

To evaluate the oxidative degradation of the scaffolds in a cellular model of oxidative stress, immortalized murine BMDMs were cultured on the scaffolds for 9 d with or without pro-inflammatory activation using 50 ng/mL IFNγ and 10 μg/mL LPS. This model was used because macrophages primed with γ-interferon (IFNγ) and activated with LPS typically respond through the upregulation of the M1, pro-inflammatory phenotype, which results in increased production of ROS and nitric oxide (Antonio Sica, Schioppa, Mantovani, & Allavena, 2006). When cultured in tissue culture plates, the immortalized BMDMs produced higher levels of H_2O_2 per cell, relative to untreated BMDMs (Figure 29A).

The increased peroxide production by the immortalized BMDMs due to IFNγ/LPS treatment likely facilitated the accelerated degradation of PEG-P_7-PEG-crosslinked scaffolds (Figure 29B). This was evidenced by the appearance of widespread pitting and < 10 μm pores in the polymer networks of peptide-containing scaffolds incubated in the presence of activated BMDMs. For all scaffolds that were incubated with non-activated BMDMs, as well as PEG-dihydrazide-crosslinked scaffolds treated with activated BMDMs, the scaffolds exhibited no observable changes in pore architecture during the same incubation period.

To quantify these changes in the pore architecture of the scaffolds, scaffolds were imaged via μCT, and the porosity was assessed from the reconstructed images (Figure 30). 3D heat maps of the pore sizes at each voxel were constructed, and pores were visualized as the blue regions in the images (Figure 30A). Notably, macropores were evident in all non-degraded scaffolds. However, the high density

of blue voxels in the PEG-P_7-PEG-crosslinked scaffolds seeded with activated BMDMs, indicating the increased occurrence of micropores in this scaffold (Figure 30A). These observations are consistent with observations via SEM (Figure 29).

The distribution of pore diameters was plotted from these images. PEG-dihydrazide-crosslinked scaffolds exhibited similar pore size distributions regardless of whether they were incubated with untreated or activated BMDMs (Figure 30B). However, in PEG-P_7-PEG-crosslinked scaffolds, activated BMDMs elevated the presence of micropores (diameters < 10 μm; Figure 30C). Because SEM results showed an increase in the occurrence of pores with diameters < 10 μm within these particular scaffolds, the 0-10 μm pore diameter range was gated as a region of interest (ROI), and the number of voxels that contain pores within this range can be measured as a percentage of the total number of voxels in the 3D image. After incubation with untreated BMDMs for 9 d, 1.4 ± 0.7% and 2.2 ± 0.6% of pores within PEG-dihydrazide- and PEG-P_7-PEG-crosslinked scaffolds, respectively, were generated within the ROI. PEG-dihydrazide-crosslinked scaffolds incubated with activated BMDMs for the same time period contained 1.1 ± 0.2% pores within the ROI. PEG-P_7-PEG-crosslinked scaffolds under these same conditions demonstrated a noticeable increase in pores within the ROI (4.0 ± 2.4%) relative to the same scaffold type incubated with untreated BMDMs.

Discussion

The goal of the present work is to demonstrate proof-of-concept of ROS-mediated degradable scaffolds through the covalent association of ROS-responsive

crosslinkers with non-responsive backbone polymers. Such a scaffold provides a new model in the toolbox to design an ROS-responsive biomaterials platform that exerts effects over a much longer time scale than the poly(propylene sulfide)-based platform (Napoli, et al., 2004).

Proline oligomers were selected to be the ROS-responsive component of the model scaffold, based on earlier work by Amici et al., which demonstrated that proline, histidine, lysine, and arginine residues within polypeptide chains are particularly susceptible to oxidative cleavage (Amici, et al., 1989). While oligomers of these other amino acids were not investigated as crosslinkers in the work presented here, they are expected to also be degradable under oxidative environments. Nevertheless, proline oligomers were selected in this study, because proline is the only amino acid that is capable of forming a tertiary amide bond, which is known to be more easily oxidized than secondary amide bonds (Schuessler & Schilling, 1984). It is therefore expected that linear peptide or polymer chains containing secondary amide linkages can also degrade under oxidative conditions, although the degradation rate may be slower than that of the proline oligomers shown here. The oxidative degradation of the polymer networks containing secondary amide bonds was evidenced by our data, where control PEG-dihydrazide-crosslinked scaffolds also experienced degradation through 28 d in 1 mM SIN-1, although not to the same extent as the P_7-crosslinked scaffolds (Figure 28).

With the intended controlled release application of these scaffolds, methods to increase the surface area of contact between the scaffold and the fluid environment were of paramount importance. To achieve this goal, a salt-leaching

process was employed in order to introduce pores throughout the crosslinked polymer network. Further, the crosslinking reaction takes place in a hydrophobic solvent. Hence, the condensation of water due to the amine-carboxylic acid crosslinking reaction results in the phase separation of water from the bulk solvent, producing smaller diameter 'micropores' (diameter < 10 μm) in the polymer network (Figure 26). The presence of micropores further increases the surface area of contact between the scaffolds and their environments, but μCT of the scaffolds suggests that micropores account for less than 1% of all the pores in the scaffolds following synthesis. However, following oxidative degradation of the PEG-P_7-PEG-crosslinked scaffolds, an increase in the occurrence of these micropores was observed (Figure 30C).

It is also notable that the observed response rates for the polymeric scaffolds in this study are much slower than those observed for other oxidation-responsive scaffolds. For example, poly(propylene sulfide)-based systems have been shown to degrade within the time scale of < 6 h in response to H_2O_2 (Napoli, et al., 2004). More recently, polythioether ketal nanoparticles were shown to degrade in response to ROS on the order of 15 h, but required an acidic environment to completely degrade (Mahmoud, Sankaranarayanan, Morachis, Kim, & Almutairi, 2011). Therefore, the complete degradation of the polymeric system discussed in the current study is expected to occur in > 10x as much time as other, alternative systems.

In order to completely isolate oxidation-responsive behavior to the crosslinkers, alternative coupling chemistries may be necessary to covalently bind

the crosslinkers to the backbone polymers. The Huisgen 1,3-dipolar cycloaddition reaction—better known as azide-alkyne 'click' chemistry—has been suggested to form linkages that remain relatively inert under oxidative conditions (Kolb & Sharpless, 2003). Alternatively, disulfide bridges are not susceptible to oxidative cleavage, as such conditions actually promote the formation of these 'crosslinks'—even under physiologically relevant constraints (Tu, Ho-Schleyer, Travers, & Weissman, 2000). This strategy has been successfully employed by others to form highly-crosslinked hydrogels (Shu, Liu, Luo, Roberts, & Prestwich, 2002). With the goals and scope of the present work in mind, these modifications are an appropriate subject for further development and refinement of our system.

Nevertheless, the oxidation response of the proline oligomers was tracked throughout the synthetic process, from the free peptides to the crosslinkers to the scaffolds. It is clear that the proline oligomers are more susceptible to oxidative cleavage rather than their flanking PEG chains. This was supported by GPC measurements that suggested that the PEG-P_n-PEG crosslinkers retained intact PEG structure under MCO conditions (Figure 25). The harsh MCO conditions were chosen because in the presence of copper ions, H_2O_2 can be decomposed into highly reactive hydroxyl radicals (McCall & Frei, 2000).

While the MCO system has been widely employed to mimic oxidative stress *in vitro*, evidence for its physiological relevance *in vivo* remain controversial in spite of the availability of plausible mechanisms (McCall & Frei, 2000; Murphy, Packer, Scarlett, & Martin, 1998; Earl R. Stadtman, 1990). This is partly because significantly greater concentrations of free metals and H_2O_2 are used in the *in vitro* model than

what is typically found *in vivo*. Alternatively, the contributions of peroxynitrite ($ONOO^-$) to oxidative stress *in vivo* are known to be more significant, because of their high reactivity, and capability of diffusing across lipid bilayers (Murphy, et al., 1998). Therefore, upon formation of the crosslinked scaffolds, oxidative environments were established via a SIN-1 treatment, since SIN-1 slowly decomposes under aqueous conditions to form O_2^- and $NO^\cdot$ ions, which can very rapidly combine to form $ONOO^-$. This treatment regime produces a more physiologically relevant model of the oxidative stress environment versus the MCO system used in preceding studies. Under these conditions, the presence of proline oligomers within the scaffolds promoted the ROS-responsiveness of the model scaffolds.

Because the scaffolds contained approximately 18% PEG-P_n-PEG by weight, oxidized scaffolds were expected to retain up to ~82% of their mass (the backbone polymer component) following oxidative treatment. While control PEG-dihydrazide-crosslinked scaffolds retained more than 82% of their mass during the study period, the peptide-containing scaffolds retained ~70%. These findings suggest that oxidative degradation is not limited to the crosslinker components of the scaffolds. Although we selected a 4%PEG-86%PCL-10%cPCL-based polymer to avert this possibility, the PCL/cPCL components are polyesters and therefore, can undergo both hydrolytic and oxidative degradation. These conclusions are consistent with the findings of other groups (Ali, et al., 1994).

The scaffolds were next incubated with untreated or activated murine macrophages in order to establish the ability of these scaffolds to respond to

oxidative stimuli presented in a more physiologically-relevant model. SEM and μCT imaging were used to observe changes in the pore architecture of the scaffolds after the 9 d incubation period, and confirmed that PEG-P_7-PEG-crosslinked scaffolds, only when incubated with activated macrophages, experienced structural changes and an increase in the occurrence of micropores. Therefore, within this *in vitro* model of inflammation-related oxidative stress, the activated macrophages degraded the proline oligomer-containing scaffolds more effectively than they did the control scaffolds that were crosslinked with PEG-dihydrazide. This is likely due to increased H_2O_2 production by activated macrophages relative to untreated macrophages. Because of the relatively short study period, complete degradation and disintegration of the scaffolds was not observed.

This is, to our knowledge, the first demonstration of an ROS-mediated, degradable polymeric scaffold, and paves the way for applications in tissue engineering and controlled release where chronic oxidative stress is expected due to disease progression, or as a response to implanted materials. The results presented in this study also have widespread implications, since polymeric scaffolds containing peptide-based elements, such as protease-degradable peptide sequences and cell binding motifs, are very widely used (DeLong, Gobin, & West, 2005; Miller et al., 2010; West & Hubbell, 1998). In particular, protease-treated hydrogels containing degradable peptide sequences have been shown to degrade significantly over the course of a few days. Because oxidative degradation of peptide-containing scaffolds occurs over longer time frames, this phenomenon is unlikely to significantly affect their proteolytic degradation *in vivo*. However, our findings

suggest that in applications where an implanted, peptide-containing biomaterial is required to remain viable for months, local ROS production may influence the function and stability of the implant.

In conclusion, we have synthesized polymeric biomaterials scaffolds chemically crosslinked with proline oligomers, which are degradable via local ROS production. These scaffolds may be potentially loaded with drugs and other species for the site-specific therapy of conditions where ROS levels are elevated due to pathogenesis, such as in implant rejection and atherosclerotic plaques. Due to the weeks-to-months timescale required to completely degrade these materials, the use of these materials to treat such conditions, where chronic oxidative stress is often observed, will reduce the necessity for multiple injections or implantation procedures to address the condition.

Summary

Recent work in the laboratory of Craig Duvall has shown that polymeric scaffolds can be loaded with polymeric nanoparticles carrying siRNA, in order to achieve localized, intracellular delivery of drugs and other biologics at pathologic sites (C. E. Nelson, et al., 2012). In light of this work, a combination of the work in this chapter and the previous one offers a glimpse of how local, pathologic inflammatory processes can be leveraged to achieve localized delivery of siRNA into macrophages via the ManNPs, released via oxidation-degradable scaffolds.

CHAPTER V

SYSTEMIC INJECTION OF MANNOSYLATED POLYMERIC MICELLES FOR TARGETED DRUG DELIVERY TO TUMOR-ASSOCIATED MACROPHAGES

In Chapter III, I described the design, synthesis, and *in vitro* performance of ManNPs, which are composed of mannosylated triblock copolymers, including a cationic block for electrostatic condensation of nucleic acid-based therapeutics, as well as a pH-responsive block that is hydrophobic at physiologic pH ranges, enabling the potential for encapsulation of hydrophobic small-molecule drugs. The ManNPs are targeted to CD206, which is upregulated by TAMs, and were minimally internalized into human breast cancer cell lines *in vitro* (Figure 18). In this chapter, the ManNPs were administered retro-orbitally into two murine tumor-bearing models, including the polyoma middle T oncogene (PyMT) model of spontaneously-arising breast cancer, and a tail-vein tumor cell injection model of metastatic breast cancer. The purpose of these experiments was to evaluate the cell-specificity of the ManNPs and the potential to achieve TAM-targeted drug delivery. While the ManNPs delivered fluorescently-labeled siRNA into TAMs more specifically than into tumor cells in both models, significant levels of TAMs remained untreated as evaluated by flow cytometry, suggesting that the first generation of ManNPs developed here may require further refinement and optimization in order to enable more widespread targeting of TAMs. Nevertheless, the cell-specificity of the carriers described in this work provides new avenues for TAM-centric immunotherapies.

Introduction

TAMs represent an intriguing target for cancer immunotherapy, because of their ability to perform a spectrum of functions, from pro-inflammatory, cytotoxic activities, to anti-inflammatory, growth-promoting functions. In various human cancers, TAMs have been observed in the tumor periphery and in some cases, in the necrotic, hypoxic core regions. In either case, TAMs have been known to be anti-inflammatory, secreting an array of proteins that lead to immunosuppression, tumor growth, extracellular matrix proteolysis, and local angiogenesis (Fridman, Pages, Sautes-Fridman, & Galon, 2012; Antonio Sica, et al., 2006). Therefore, TAM-targeted interventions, including depletion, modification, and reprogramming have been proposed as potential immunotherapeutic routes in cancer (DeNardo et al., 2011; Hagemann, et al., 2008).

Because macrophages are among the most phagocytic cell types in the body, it is not difficult to deliver drugs into these cells. Work by others suggests that targeting motifs may not be necessary in order to target nanoparticles for macrophage uptake (Daldrup-Link et al., 2011; Van Rooijen & Sanders, 1994). In many cases, the minimization of macrophage uptake of drug delivery systems is a significant challenge (Li & Huang, 2009). However, macrophages are resident cells in many tissues and organs, including the bone marrow, liver, and spleen. Therefore, site-specific drug delivery into TAMs presents a significant challenge in order to minimize the risk of eliciting autoimmune manifestations in off-target organs and tissues.

To achieve this, molecularly-targeted drug delivery systems have been developed that home into receptors and biomarkers upregulated in macrophages located at pathologic sites. These include the LyP-1 peptide directed against p32, toll-like receptor agonists, dextran-coated nanoparticles against SIGNR-1, monosaccharides against various macrophage lectins, and HDL-mimetic peptides and nanoparticles (Cormode, Briley-Saebo, et al., 2008; Cormode, Skajaa, et al., 2008; Fogal, Zhang, Krajewski, & Ruoslahti, 2008; Frias, Ma, Williams, Fayad, & Fisher, 2006; Kortylewski, et al., 2009; Laakkonen, Porkka, Hoffman, & Ruoslahti, 2002; Morishige et al., 2010; Song et al., 2012; Taylor et al., 2004). With the exception of the monosaccharide-based approaches, most of these approaches exhibited some targeting of other tumor cells or immune cells, suggesting that such approaches hold the most promise for TAM-specific drug delivery systems.

Mannose receptor (CD206) is an endocytotic receptor present mainly on macrophages and dendritic cells, and upregulated on TAMs (East & Isacke, 2002; Joyce & Pollard, 2009; A. Sica, et al., 2008; Taylor, et al., 2005). Through the use of endosomolytic polymers such as those developed in Chapter III, intracellular delivery of biologics can be achieved, potentially enabling the interference with pathological mechanisms present in TAMs. These polymers self-assembled into micellar structures with a mannose-presenting corona, and have been shown to promote siRNA delivery into primary macrophages and immortalized human macrophages *in vitro*. In this work, the TAM-specificity of these particles is further evaluated in an *in vivo* environment, in order to showcase its potential applicability to TAM-centric immunotherapies and imaging approaches.

Materials and Methods

Animals and Cell Lines

Animal work was approved by the Vanderbilt University Institutional Animal Care and Use Committee. All mice were on an FVB background strain. The primary, spontaneously-arising tumor model involved FVB mice carrying the polyoma middle T oncoprotein (PyVT) gene. Originally developed by Bill Muller and colleagues, the PyVT mouse model is now commercially available through Jackson Laboratories, and naturally develop palpable mammary tumors as early as 5 weeks of age, with pulmonary metastases observed in 80-94% of adult mice 12-15 weeks of age (Guy, Cardiff, & Muller, 1992). At 13 weeks old, female mice were anesthesized via isoflurane inhalation, and injected retro-orbitally with 1 mg/kg FAM-labeled siRNA loaded into polymers at a 4:1 N:P ratio. The mice were then incubated for 24 h, sacrificed via CO_2 inhalation and then cervical dislocation, and then organs (tumors, liver, lungs, spleen, kidneys, and small intestines) were collected for detection of FAM-siRNA via immunohistochemistry or flow cytometry. Hematoxylin and eosin staining of paraformaldehyde-fixed, paraffin-embedded tissues (lungs, liver) was performed by the Vanderbilt Translational Pathology Shared Resource using standard techniques.

Flow Cytometry

Whole organs were isolated from mice post-mortem, and minced into a cleavage cocktail containing 3 mg/mL collagenase-A and 3 mg/mL DNAse I (Roche Applied Science, Indianapolis, IN). After 2 h incubation at 37°C, the cell suspensions

were run through 40-μm cell strainers and treated with ACK lysing buffer (Life Technologies) according to manufacturer's instructions, to lyse red blood cells. After pelleting the remaining cells by centrifugation at 300 x g for 5 min, cells were fixed in 8% paraformaldehyde for 10 min, treated with anti-CD16/CD32 (BD Biosciences, San Jose, CA) to block Fcγ receptors, and then stained with rat anti-mouse CD45-PECy7 (Clone 30-F11) and rat anti-mouse CD11b-APC (Clone M1/70; both antibodies from eBioscience, San Diego, CA). Multi-color flow cytometry, including analysis of single-stained controls for compensation calculation, was performed on a BD FACSCanto II system, operated by the BD FACSDiva software. Post-acquisition data analysis and reporting were performed on FlowJo (version 7.6.4).

Confocal Microscopy of Frozen Sections

For frozen sections, murine organs were collected into TissueTek OCT compound (Fisher Scientific), frozen at -80°C, and then cut into 5μm-thick sections prior to fixation in 4% paraformaldehyde for 20 min. After rinsing sections 3x with PBS, tissues were permeabilized via treatment with 1% Triton X-100 for 30 min, then blocked for 1 h in 1% BSA in PBS. After rinsing 3x with PBS, tissues were stained with RPE-conjugated rat anti-mouse CD206 (AbD Serotec, Raleigh, NC) overnight at 4°C. After rinsing 3x with PBS, slides were stained with DAPI, mounted, and imaged as described above. FAM (siRNA) and PE (CD206 Ab) images were collected separately using the available 488 nm and 561 nm lasers, respectively, in order to prevent spectral overlap between the two dyes. Correlation plots were

constructed using the JaCoP (Just Another Correlation Plugin) macro, loaded into ImageJ (version 1.45s) (Bolte & CordeliÈRes, 2006).

Results

Because ManNPs enhanced siRNA delivery and knockdown relative to untargeted diblock nanoparticles in primary and immortalized macrophage cell lines *in vitro*, we next evaluated the performance of the nanoparticles *in vivo* in tumor-bearing mice. For these studies, we used FVB mice expressing the polyoma middle T oncoprotein (PyVT), which spontaneously develop primary tumors within 5-7 weeks of age, with pulmonary metastases occurring as early as 12-15 weeks of age (Guy, et al., 1992). In this way, PyVT mice model the natural progression of human disease from localized tumors into metastatic disease, and the involvement of leukocytic subtypes in disease progression continues to make this model among the most reliable murine models of breast cancer in humans today (Lin et al., 2003).

Therefore, 13-week old, female PyVT mice were injected retro-orbitally with 1 mg/kg FAM-siRNA, loaded into ManNPs or non-targeted diblock nanoparticles, and allowed to incubate for 24 h prior to sacrifice and collection of organs for detection of FAM-siRNA via flow cytometry and confocal microscopy (Figure 31). As a control, some mice received a blank PBS injection (mock).

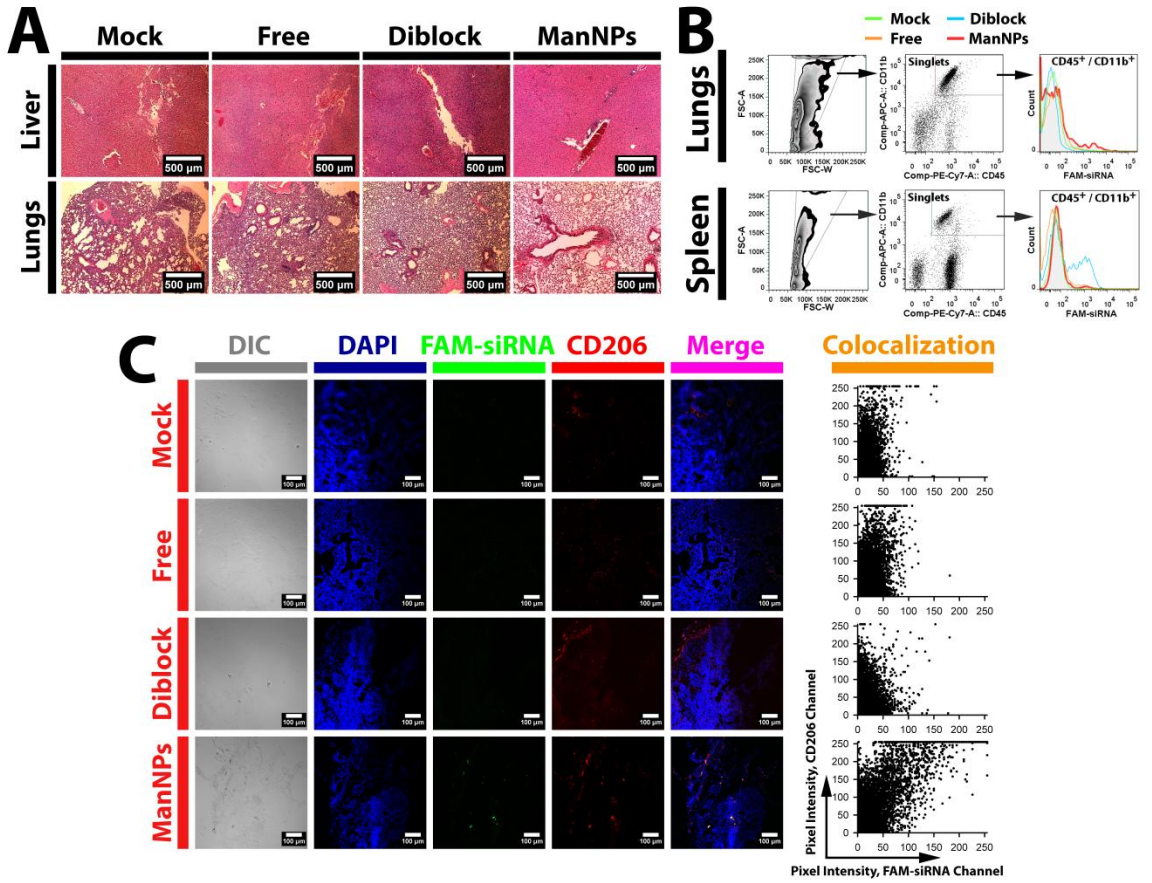

FIGURE 31. ManNPs Enhance siRNA Delivery into TAMs in Primary Murine Breast Tumor Model. 24 h after retro-orbital administration of 1 mg/kg FAM-labeled siRNA, injections are well-tolerated by the mice as evidenced by the lack of significant necrotic tissue or abnormal staining patterns via H&E of harvested livers and lungs, where nanoparticles are either cleared or can cause acute toxicity (A; scale bars = 500 µm). (B) Flow cytometry analysis of $CD45^+$ $CD11b^+$ cells in the lungs (top) and spleen (below) reveal some homing of ManNPs into these cells in the lungs, as well as splenic localization of non-targeted diblock nanoparticles. (C) Co-localization of FAM-siRNA with $CD206^+$ cells in primary mammary tumors is only observed when ManNPs were used as the vehicle (Scale bars = 100 µm).

In all cases, injections were well-tolerated by the animals, as evidenced by insignificant differences in lung and liver morphology by hematoxylin & eosin staining (Figure 31A). Injected nanoparticles typically clear through the liver and the spleen, and consistent with this, some siRNA localization was observed in the spleen, when the untargeted diblock nanoparticles were used as the delivery vehicle

(Figure 31B) (Alexis, Pridgen, Molnar, & Farokhzad, 2008). The lungs are also typically home to a small subset of alveolar and interstitial macrophages, and some siRNA localization was also observed here (Laskin, Weinberger, & Laskin, 2001).

Most importantly, ManNPs enhanced siRNA colocalization with CD206 in frozen sections of the primary tumors (Figure 31C). This was not observed for sections collected from mice treated with free siRNA or siRNA complexed with untargeted diblock nanoparticles. These results suggest that mannosylation of the polymers via 'click' chemistry enables cell-specific siRNA delivery into TAMs *in vivo*.

Discussion

The modulation of TAM behavior *in vivo* requires cell-specific drug delivery vehicles in order to reactivate pro-inflammatory functions in TAMs while leaving resident macrophages elsewhere untouched. This is particularly important because inadvertent activation of off-target macrophages may lead to autoimmune manifestations (Caspi, 2008). Because ManNPs were previously shown to enhance siRNA delivery into primary macrophages, while demonstrating modest delivery into tumor cells, we investigated their ability to achieve TAM-specific siRNA delivery in a spontaneous murine breast tumor model (Lin, et al., 2003).

As shown earlier, the ManNPs are block copolymers that exhibit a mannose-presenting corona for CD206 targeting, a cationic layer for complexation of nucleic acids, and a pH-responsive endosomolytic layer to enable endosomal escape of the polymers and their cargo (Figures 12, 19). Overall, the ManNPs exhibit a positive surface charge (Table 5). Significant safety issues hamper the translation of cationic

gene and siRNA delivery vehicles into humans. Some major questions include (1) the rapid adsorption of serum proteins onto the cationic surface, thereby mitigating the targeting functions and ligands on the nanoparticle corona and leading to rapid clearance and toxicity in the RES, (2) the induction of platelet aggregation and coagulopathies, (3) formation of emboli in the smallest-diameter (<10 μm) capillaries in the lungs (Alexis, et al., 2008; Fako & Furgeson, 2009; Jones et al., 2012). Because of these safety concerns, it is necessary to examine the effects of *in vivo* nanoparticle injection on the host animal's lungs and clearing organs. A pathological examination of these organs showed that the nanoparticles were well-tolerated and did not cause significant emboli formation or necrosis here.

Further, the nanoparticles were able to home into the primary tumors of the mice, and mannosylated carriers even targeted TAMs in these tissues, as evidenced by $CD206^+$ (macrophage mannose receptor) staining, which is almost exclusive to these cells Figure 31C). While this study did not quantify effects of siRNA delivery on target gene expression in the TAMs versus in other cells in the tumor, previous evidence *in vitro* suggests that the delivered siRNA remains functional (Figure 21A). Future extensions of this work are ongoing and to quantify siRNA-mediated gene knockdown in TAMs within the same PyVT mouse model described here, as well as in metastatic tumor models.

Other strategies also exist to target macrophages *in vivo*, including peptides, antibodies, synthetic lipid nanoparticles, and non-targeted PEGylated nanoparticles (Bastús et al., 2009; Larsen, et al., 2009; Shann S. Yu et al., 2011). In many cases, macrophages are among the most phagocytic cell types present in the body, and

therefore, molecular targeting motifs may not be necessary to produce significant macrophage targeting *in vivo* (Daldrup-Link, et al., 2011). To deliver genes or siRNA into macrophages, the vehicle must overcome the highly degradative lysosomal and phagosomal compartments present within these cells, in order to access the target intracellular compartments where these agents can function (Stacey, et al., 1993).

Because ManNPs are able to selectively target TAMs without affecting other tumor cells, they provide a platform for the interrogation of TAMs with the goals of characterizing downstream effects on the tumor and on the rest of the immune system. To achieve these ends, key targets of interest for siRNA knockdown within TAMs include the NF-κB and STAT families of pathways, which regulate their expression of whole libraries of cytokines, growth factors, enzymes, and angiogenic factors (Connelly et al., 2011; Murray, 2007; Porta, et al., 2009). These families of pathways include more than 40 interesting genes to target, and the potential effects of siRNA-mediated knockdown have been studied through the use of genetically-engineered knockout models. Some, such as STAT3, have additionally been studied in the context of therapeutic siRNA-mediated knockdown, resulting in the induction of anti-tumor immune responses in murine tumor models (Kortylewski, et al., 2009). Therefore, this area remains a burgeoning area for investigation of new immunotherapeutic strategies for cancer.

Summary

In this chapter, the ManNPs developed earlier (Chapter III) were systemically injected *in vivo* into a well-investigated spontaneous murine model of breast cancer,

in order to evaluate the ability of these glycoconjugates to home into TAMs. The preliminary data shown here suggests that these nanoparticles are well-tolerated by the mice at the doses administered, and enhance siRNA delivery into $CD206^+$ cells present in the tumor. The ManNPs present a viable platform for the interrogation of TAMs without affecting other cell types present in the tumor environment.

CHAPTER VI

ASSESSMENT OF THE EFFICACY OF CANCER IMMUNOTHERAPIES IN HUMAN BREAST CANCER PATIENTS

Despite the successful treatment of some patients with recent cancer immunotherapies, many non-responders have been reported. It is increasingly clear that this is partly due to the ability of tumors to exhibit multiple mechanisms for the suppression of anti-tumor immunity, suggesting that combination immunotherapeutic approaches may be necessary to overcome these barriers. Because T-cells are the primary effector cells that clear tumor masses, many immunotherapies are designed with the goal of augmenting anti-tumor T-cell responses. While phenotypic biomarkers of T-cell subtypes and activation states have been well-documented, T-cell-based biomarkers of immunotherapeutic efficacy have not been identified. Therefore, the purpose of this study was to design flow cytometric and miRNA-profiling assays for the longitudinal assessment of T-cell responses in patients enrolled in cancer immunotherapy clinical trials, with the ultimate goal of uncovering biomarkers of the efficacy of anti-cancer immunotherapies. The ongoing work presented here may promote the development of new, streamlined methods for the temporal tracking of patients enrolled in future immunotherapeutic clinical trials, and the identification of novel biomarkers and targets for drug development.

Introduction

Cancer immunotherapies seek to jump-start anti-tumor immune responses and have the potential to induce long-term immunity to phenotypically similar tumor cells due to the ability of the immune system to 'remember' past antigens. However, the activation of anti-tumor immunity requires the involved immune cells to overcome several hurdles. First, dendritic cells with access to the tumor must be capable of sampling tumor antigens and becoming activated, leading to their migration into the lymph nodes. There, they must be able to interact with immature T-cells, selecting and expanding clones that are specific for tumor antigens. Finally, the activated T-cells must be able to migrate back into the tumor, where they must then overcome the immunosuppressive environment promoted by the tumor and its supporting stroma, which commonly includes TAMs, myeloid-derived suppressor cells (MDSCs), and T_{reg} cells, all of which contribute towards the de-activation of the incoming T-cells (Mellman, Coukos, & Dranoff, 2011).

A number of current FDA-approved immunotherapeutic approaches are capable of achieving one of these three requirements. A recent example is the anti-CTLA4 antibody (ipilimumab), which essentially releases the 'brakes' on T-cell activation, re-activating pre-existing anti-tumor T-cells that may have become suppressed by the tumor (Mellman, et al., 2011). While these therapies have improved long-term survival through the induction of anti-tumor immunity in some patients, many non-responders exist, suggesting the need for an integrative, multi-pronged immunotherapeutic approach that uses several agents in combination, in order to tackle the three hurdles listed above. The recognition that such

combination approaches may improve the efficacy of immunotherapies was among the reasons behind the recent creation of the Cancer Immunotherapy Trials Network (CITN) by the National Cancer Institute, and its first clinical trials include a few such approaches ("Immunotherapy Network Launches First Trial," 2012).

While various immunotherapies differ in terms of target cell type or biomarker, approach, and mechanism of action, the ultimate goal is typically to activate anti-tumor $CD3^+/CD8^+$ T-cells. These cells, also called cytotoxic T lymphocytes (CTLs), are capable of potent anti-tumor cell effector functions, and thus, their presence at tumor sites has been commonly correlated with promising clinical outcomes and longer disease-free survival for patients of various cancers (Fridman, et al., 2012). In consequence, the characterization of the T-cell response in clinical trials patients treated with experimental immunotherapies is of significant interest to the community.

While much is known about phenotypic markers of various T-cell subtypes and activation, biomarkers of immunotherapy efficacy remain elusive. The identification of such biomarkers may streamline the longitudinal assessment of patient responses during the clinical trials, and also provide new avenues for drug development aimed at the promotion or suppression of those biomarkers. For this purpose, we designed a multiparameter flow cytometry panel aimed at characterization of T-cell phenotypic subtypes and activation states (Table 6). Further, we also assessed the miRNA expression profile within the T-cells, as miRNAs have been shown to regulate entire gene pathways and networks due to their polygamous nature (Pritchard, Cheng, & Tewari, 2012).

TABLE 6. Multicolor Phenotyping Panel for Assessment of T-Cell Responses in Immunotherapy Clinical Trials Patients.

Marker	Fluorophore	Description	Reference
CD3	FITC	Associated with T-cell receptor	(Kindt, et al., 2007)
CD4	AF700	Marker of T_H cells	(Kindt, et al., 2007)
CD8	APC-Cy7	Marker of T_C cells	(Kindt, et al., 2007)
CD25	APC	IL-2 receptor α-chain	(B. H. Nelson, 2004; Papiernik, de Moraes, Pontoux, Vasseur, & Pénit, 1998)
CD28	PE-CF594	T-cell co-stimulatory factor, related to CTLA-4	(Boise et al., 1995; Sharpe & Freeman, 2002)
CD45	AmCyan	Marker of all immune cell subtypes, also known as leukocyte common antigen	(Kindt, et al., 2007)
CD45RA	PE-Cy5[1]	Commonly used to identify naïve T-cells	(Kindt, et al., 2007)
CD56	PE-Cy7	Neural cell-adhesion molecule (NCAM), also commonly used to identify NK cells	(Lanier, Testi, Bindl, & Phillips, 1989)
CD127	BV421[2]	IL-7 receptor α-chain; mediates expansion and survival of memory and naïve T-cells	(Hartigan-O'Connor, Poon, Sinclair, & McCune, 2007)
CD197	PerCP-Cy5.5	CCR7; Receptor for chemoattractants CCL19/21, mediates functional organization of the immune system and lymph nodes	(Worbs & Förster, 2007)
CD278	PE	Inducible T-cell costimulatory molecule (ICOS)	(Hutloff et al., 1999)
CD279	BV711[2]	Programmed cell death-1; engagement by PD-L1 reduces T-cell activation, proliferation, and cytokine secretion	(Freeman et al., 2000)
HLA-DR	BV605[2]	MHC-II isotype	(Choi, Majumder, & Boss, 2011)

[1]This particular fluorophore appears to give a significant level of spectral overlap into other channels, and has since been replaced with a dye that exhibits a narrower emission spectrum.
[2]BV dyes are shorthand for "Brilliant Violet."

Materials and Methods

Patients and Human Subjects

For assay development, healthy human volunteers were consented and whole blood samples were collected into heparin-coated tubes via venipuncture on the median cubital vein. For microarray experiments, blood samples were obtained from consented patients enrolled in a clinical trial approved by the United States Food and Drug Administration and the University of Washington Human Subjects Division. Full description of the enrollment criteria and the characteristics of the patients were documented elsewhere (Disis et al., 2009).

Antibodies and Flow Cytometry

All antibodies were purchased from BD Biosciences (Franklin Lakes, NJ) unless otherwise noted, and titrated on heparinized whole blood isolated from consenting healthy human volunteers. The antibodies included CD3-FITC (clone SK7), CD4-AlexaFluor 700 (clone RPA-T4; BioLegend, San Diego, CA), CD8-APC-Cy7 (clone SK1), CD25-APC (clone M-A251), CD28-PE-CF594 (clone CD28.2), CD45-AmCyan (clone 2D1), CD45RA-PE-Cy5 (clone HI100), CD56-PE-Cy7 (clone NCAM16.2), CD127-Brilliant Violet 421 (clone HIL-7R-M21), CD197-PerCP-Cy5.5 (clone 150503), CD278-PE (clone DX29), CD279-Brilliant Violet 711 (clone EH12.2H7; BioLegend), and HLA-DR-Brilliant Violet 605 (clone L243; BioLegend).

Antibodies were first diluted into FACS Buffer (1% BSA in PBS), to a total volume of 100 μL of the 13-antibody master mix per sample to be tested. After aliquoting 100 μL of the master mix into individual FACS tubes, 100 μL of whole

blood was added directly to the antibodies by reverse-pipeting, and mixed by vortexing briefly. The samples were incubated at room temperature in the dark for 15 min, after which 900 μL of 1X FACS lysis buffer (BD Biosciences; contains buffered < 1.5% formaldehyde and < 5% diethylene glycol) was added to each tube in order to fix the PBMCs while simultaneously lysing excess erythrocytes. After incubating samples for another 15 min at room temperature, they were stored at 4°C prior to same-day analysis, or -80°C for analysis within 1 week.

Data was acquired on a five-laser (355, 408, 488, 532, and 633 nm lasers), eighteen-channel BD LSR-II flow cytometer at the Fred Hutchinson Cancer Research Center Flow Cytometry Core (Seattle, WA). Spectral compensation using single-stained control samples, data analysis and graph generation was performed on FlowJo software.

T-Cell miRNA Profiling

PBMC aliquots (10,000,000 cells/patient/timepoint) from 10 patients, taken at 0 and 12 weeks post-treatment, were thawed and resuspended into ice-cold MACS buffer (PBS + 2% FBS + 2 mM EDTA). They were then treated with CD3-antibody-coated magnetic beads and eluted through magnetic selection columns according to the manufacturer's instructions (Miltenyi Biotec, Cologne, Germany). The purity of the isolated $CD3^+$ cells was determined to be 70-80% via flow cytometry, using antibodies against CD3 and CD4.

1,000,000 $CD3^+$ cells were then lysed and total RNA was isolated using a commercial kit according to manufacturer's instructions (Clontech NucleoSpin

miRNA kit; Clontech Laboratories, Mountain View, CA). RNA purity, concentration, and quality were assessed via Agilent BioAnalyzer (Santa Clara, CA) and NanoDrop (ThermoFisher Scientific, Waltham, MA), prior to hybridization onto Affymetrix human miRNA microarrays (Santa Clara, CA).

Results

13-Marker T-Cell Phenotyping Panel

Multiparameter flow cytometry panels suffer from issues of spectral overlap due to fluorophores of similar excitation and emission spectrum, leading to the necessity to 'compensate' for this effect through mathematical algorithms (Perfetto, Chattopadhyay, & Roederer, 2004). Crucial steps to create these matrices include the acquisition of single-stained controls (ie, samples that were stained with single antibodies from the proposed panel; Figure 32), and fluorescence-minus-one controls (ie, samples that were stained with all of the antibodies in the panel minus one of the antibodies; Figure 33). The ultimate result of this protocol is a compensation matrix such as that shown below (Table 7), which describes the interactions between individual dyes with unintended channels. In some cases, values above 100% may result, which signifies that cells stained with a certain dye show up more brightly on an unintended channel, compared with cells stained with a different dye intended for the same channel.

In particular, the original CD45RA antibody used in this panel (PE-Cy5 fluorophore) showed significant levels of spectral overlap into multiple channels, and has since been replaced with a different dye to mitigate these effects.

Nevertheless, the original panel was still functional enough for use in basic phenotyping of whole blood (Figure 34).

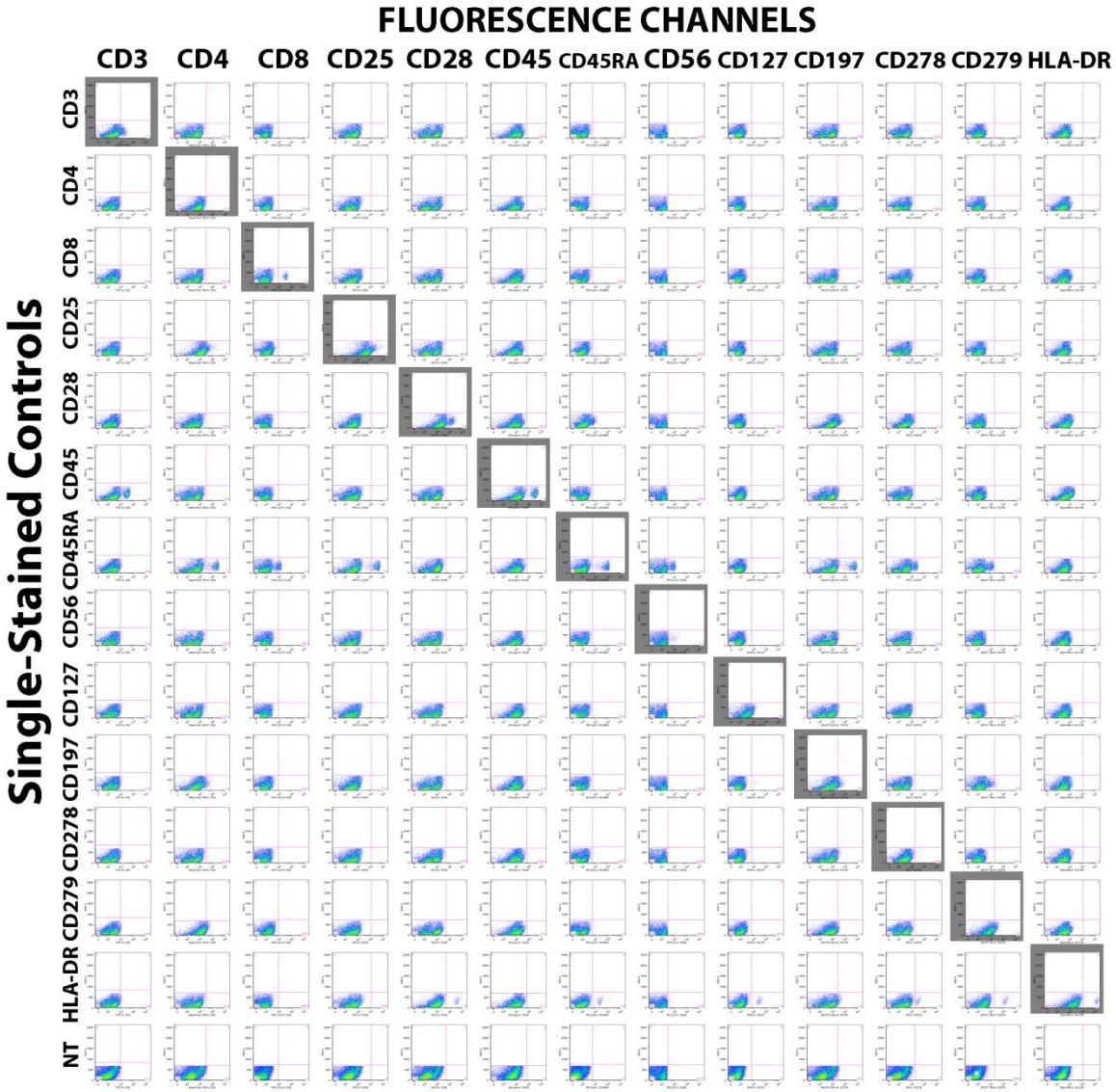

FIGURE 32. Uncompensated Acquisition of Representative Whole Blood Sample Stained with Single Antibodies from the 13-Marker Panel. Whole blood samples from a consenting human volunteer were treated with individual antibodies from the proposed panel (Table 6) or left untreated (NT) and analyzed by flow cytometry to quantify cell fluorescence in the 13 channels corresponding to each fluorophore present in the panel. In all plots, SSC-A (side scatter) has been plotted on the y-axis, and fluorescence intensity in the x-axis. Each row corresponds to a different sample, and columns correspond to each channel used in acquisition. Cells were gated for singlets and then lymphocytes based on size scatter plots. Gray highlighted boxes indicate the intended channel for which each sample is expected to show any positive signal. Some antibodies (e.g., CD25, CD278, CD279) stain the whole population and appear to cause a population shift.

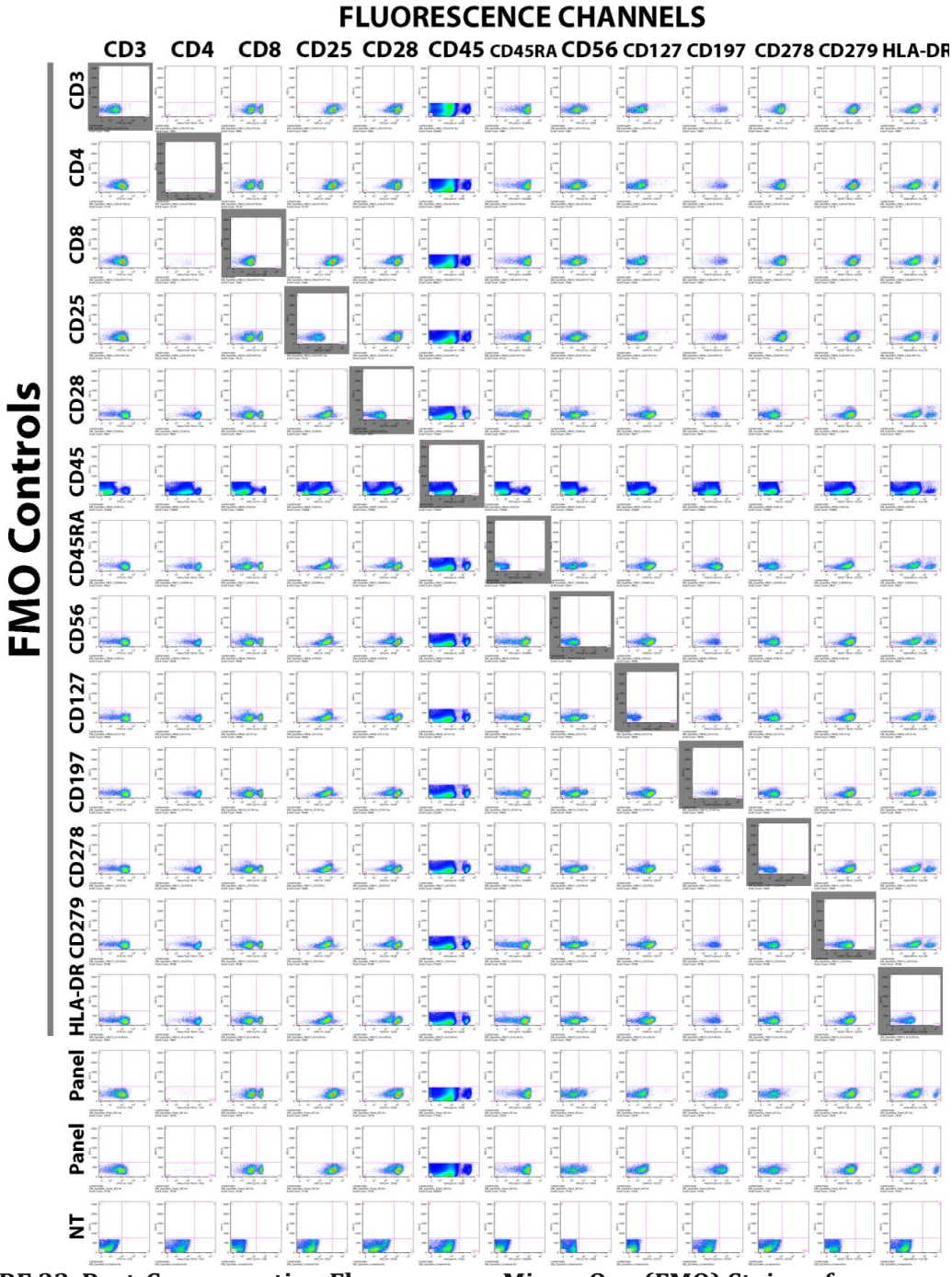

FIGURE 33. Post-Compensation Fluorescence-Minus-One (FMO) Stains of Representative Whole Blood Sample. Whole blood samples were stained with 12 of 13 of the antibodies in the proposed panel (Table 6) and analyzed by flow cytometry. Each row corresponds to a different sample missing the antibody indicated on the left, with columns indicating the channel represented. Each plot is a side scatter (y-axis) vs. fluorescence (x-axis) distribution. Gray highlights indicate plots where no positive staining should be observed, due to the particular antibody being missing from the sample. Two samples stained with the full panel and an untreated sample (NT) have been shown for comparison. All samples were gated on $CD45^+$ singlets and on size scatter plots, except CD45 plots and the CD45 FMO, which was gated based on singlets and size scattering alone.

TABLE 7. Compensation Matrix Resulting From the 13-Color Panel, with Significant Channels of Spectral Overlap Highlighted In Yellow.

	CD278-PE	CD3-FITC	CD127-BV42	CD4-AF700	CD56-PECy7	CCR7-PerCP	CD8-APCCy	CD28-ECD	CD25-APC	CD45-AmCy	HLADR-BV6	CD45RA-PE	CD279-BV71
CD278-PE		45.70	7.32	87.44	5.62	152.50	8.65	173.30	78.96	161.20	59.60	17.24	14.37
CD3-FITC	-11.04		-1.32	-19.76	-1.40	-25.42	-3.00	-33.38	-17.77	-5.60	-2.82	-4.00	-1.90
CD127-BV421	6.11	12.24		4.46	0.51	6.49	0.95	10.61	9.47	128.70	30.47	0.31	5.22
CD4-AF700	-3.00	-1.70	-0.47		-0.67	-5.65	3.74	-6.99	-7.20	-0.07	-0.10	-1.57	0.09
CD56-PECy7	40.18	0.27	0.54	-7.83		-8.99	29.65	15.62	-14.05	9.18	8.49	-1.15	1.45
CCR7-PerCPCy5.5	-2.30	-0.08	0.10	74.41	1.38		4.50	-6.14	5.04	0.49	1.11	0.07	30.06
CD8-APCCy7	-3.23	-0.99	-0.38	10.13	1.89	-6.70		-8.23	37.27	-3.66	1.20	-0.83	-0.14
CD28-ECD	4.94	-0.08	-0.08	0.06	0.17	20.88	-0.16		1.36	-0.86	5.41	3.69	0.37
CD25-APC	-0.13	0.24	0.00	23.32	0.00	0.00	1.12	-0.27		1.09	0.78	0.64	0.42
CD45-AmCyan	-0.62	9.12	0.10	-1.04	-0.07	-1.36	-0.15	-1.72	-0.91		3.02	-0.20	0.00
HLADR-BV605	1.76	0.00	1.63	0.54	0.09	1.65	0.00	24.26	1.02	1.41		1.39	8.86
CD45RA-PECy5	20.44	-0.15	-0.16	250.10	8.51	669.30	10.07	10.13	443.50	-2.43	0.34		10.81
CD279-BV711	1.01	3.38	4.87	126.80	-0.06	24.57	9.45	0.92	3.74	25.63	8.31	-0.16	

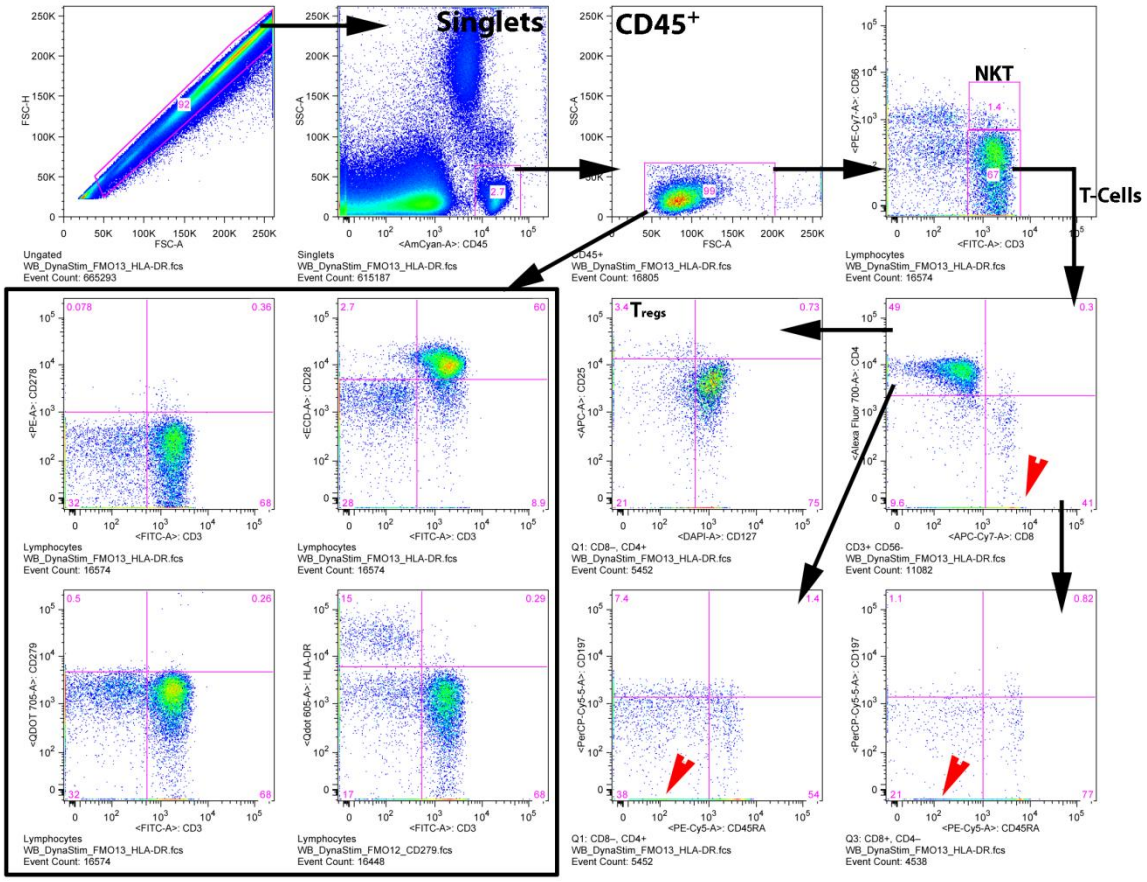

Black arrows indicate parent-subpopulation relationships.
Red arrows indicate where large populations have <0 fluorescence signal.

FIGURE 34. Phenotyping T-Cells in Whole Blood via the 13-Antibody Panel. A representative whole blood sample from a consenting human volunteer was stained with the 13-antibody panel described in Table 6. Gating strategy has been delineated with black arrows. Some major ramifications of >100% spectral overlap (as shown in Table 7) include the appearance of large populations with <0 fluorescence signal as marked with red arrowheads.

Optimization of miRNA Extraction Methods for Microarray Analysis of T-Cells in Immunotherapy Clinical Trials Patients

Patients for study were selected based on their response or non-response to concurrent treatment with trastuzumab and a HER2/*neu* peptide vaccine (Figure 35). In this clinical trial, it was observed that all patients had existing immunity to HER2/*neu* and other breast cancer antigens, which were boosted in some patients following vaccination (Disis, et al., 2009).

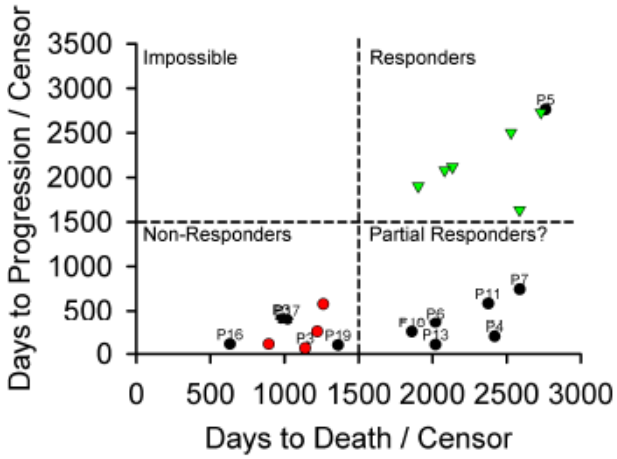

FIGURE 35. Long-Term Outcomes of Patients Enrolled in Clinical Trials for a HER2/neu Peptide Vaccine. Patients were tracked long-term for progression of breast cancer (y-axis) or death (x-axis) following concurrent treatment with trastuzumab and a HER2/neu peptide vaccine as previously described (Disis, et al., 2009). Selected responders (green) and non-responders (red) were selected for further study based on the availability of PBMCs for analysis.

First, we optimized the T-cell purification process via magnet-assisted cell sorting (MACS). PBMCs isolated by Ficoll-gradient separation were treated with magnetic beads for positive selection of $CD3^+$ cells or $CD4^+/CD8^+$ cells, and were analyzed by flow cytometry for CD3 cell purity, as well as the expression of the activation markers CD25, CD278, CD279, and HLA-DR (Figure 36). While $CD4^+/CD8^+$ selection resulted in higher purity of T-cells versus $CD3^+$ selection (85% vs. 74%,

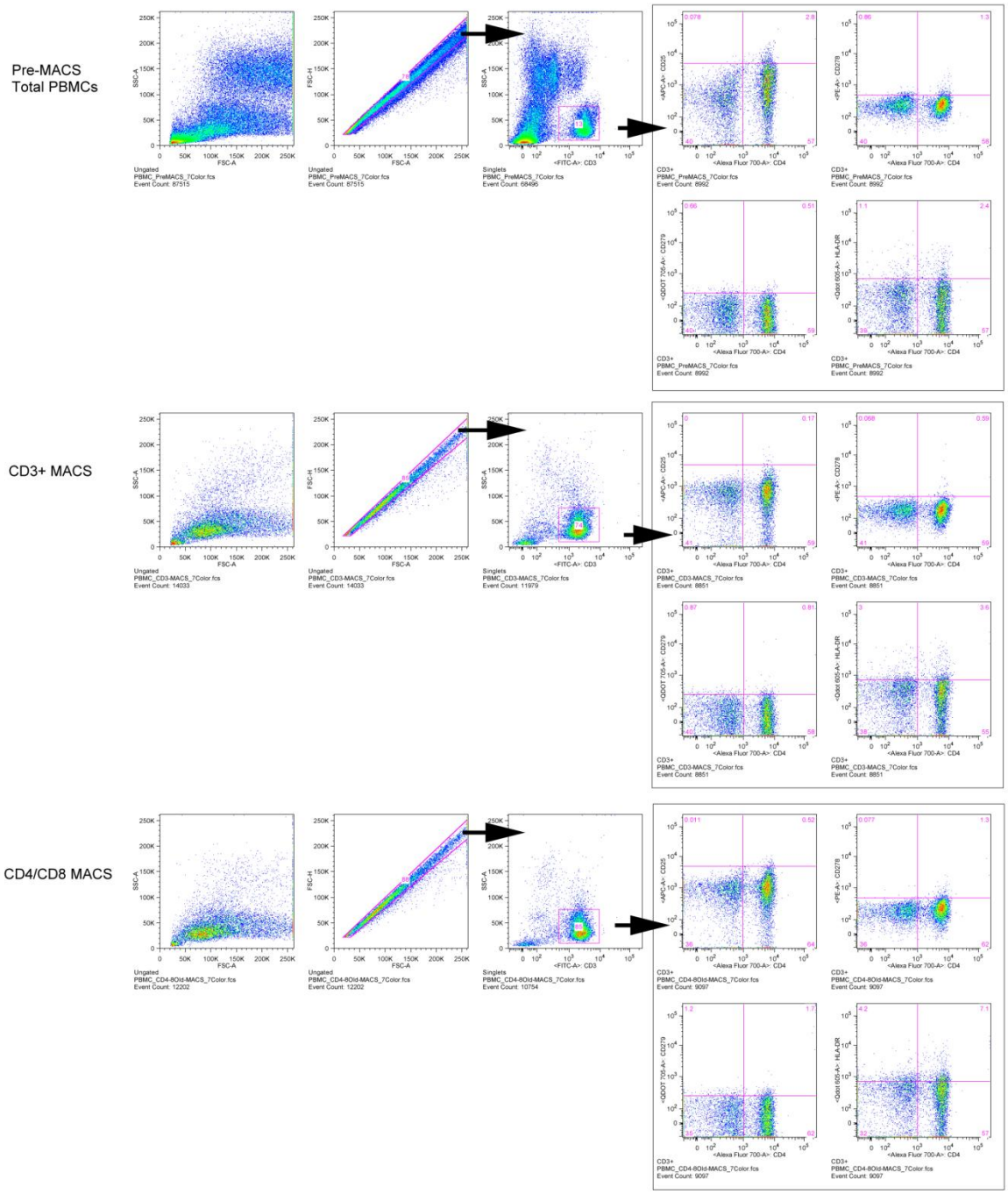

FIGURE 36. Analysis of T-Cell Purity and Activation Before and After MACS Purification from Thawed PBMCs. PBMCs (top panel) or purified T-cells via CD3+ selection (middle panel) or CD4+/CD8+ selection (bottom panel) were stained with antibodies for CD3, CD4, CD25, CD278 (ICOS), CD279 (PD-1), and HLA-DR in order to analyze for T-cell purity and activation before and after MACS purification. Gating strategies have been shown with black arrows. Size scatter plots of all of the cells in the samples prior to any gating have also been shown (left).

relative to 13% pre-MACS), it also resulted in a significant level of activation of the T-cells. HLA-DR appeared to be the most sensitive marker to T-cell activation, as it was the only marker of the four investigated that showed significant differences in expression before and after MACS. Initially, 3.5% of $CD3^+$ cells expressed the marker, but this increased to 6.6% post-$CD3^+$ selection, or 11.3% post-$CD4^+$/$CD8^+$ selection. Because it is of paramount importance to preserve the original T-cell miRNA/gene expression profiles at isolation from the patients, the poor cell purity and significant cell activation observed here was not undesirable and motivated our switch to the use of FACS for the purification of $CD3^+$ cell populations for microarray analysis.

Next, we quantified the amount of RNA yielded per cell in light of the requirements for microarray analysis (200-250 ng RNA in 8μL; 25-32 ng/μL). This was done by collecting RNA from known numbers of purified T-cells, and analyzing the resulting RNA mixtures by BioAnalyzer and NanoDrop (Table 8). In all cases, the BioAnalyzer gave "run indexes" of >9, which indicate sufficient RNA purity for microarray analysis.

TABLE 8. Purity and Concentration of Total RNA Collected from Purified T-Cells.

Cell Source	T-Cell Purity	Total Cells Lysed	Final [RNA]	Final Volume	RNA Yield (ng)	Comments
P 107250	-	500,000	7 ng/μL	100 μL	700	Too dilute
Healthy	78%	500,000	23.4 ng/μL	35 μL	819	OK for array
Healthy	78%	500,000	20.8 ng/μL	35 μL	728	OK for array
Healthy	78%	1,000,000	32.8 ng/μL	35 μL	1148	OK for array
Healthy	78%	1,000,000	44.4 ng/μL	35 μL	1554	OK for array

While the commercial kit used for miRNA isolation recommended the use of 30-100 μL water for elution and collection of total RNA in the final step of the

included protocol, it is clear that lower amounts of water are necessary to achieve the necessary RNA yields and contents for downstream analysis. In one case, 100 μL of water was used for RNA collection, and this resulted in very low RNA concentrations (7 ng/μL; Table 8). In all cases, the total quantity of RNA collected (in μg) was sufficient for analysis. Therefore, in order to meet microarray requirements, all further studies were conducted by lysing 1,000,000 T-cells and collecting the purified RNA in 35 μL of water.

At the time of writing, miRNA microarrays are in progress, and may take weeks for the completion of data acquisition and analysis.

Discussion

Continuing the early success of novel cancer immunotherapies such as the anti-CTLA4 and anti-PD-1 antibodies, more and more immunotherapies are entering clinical trials. To assess the efficacy of these agents, many have continued to use metrics that previously enabled the evaluation of other anti-cancer agents, such as anti-proliferative agents and anti-angiogenic agents. These metrics may include the quantification of short-term and immediate endpoints such as tumor growth, spreading and progression. However, immunotherapies exert their anti-tumor functions under very different mechanisms, and therefore, in some cases, effective immunotherapies were developed that enhanced immunity to tumor antigens in patients, but were shelved due to the inability of the agent to reduce tumor growth according to RECIST criteria (Mellman, et al., 2011; Pardoll & Drake, 2012). Frequently, effective immunotherapies may successfully elicit antigen-

specific T-cells, but these T-cells will still have to overcome the immunosuppressive tumor microenvironment in order to clear tumor cells (Mellman, et al., 2011). Therefore, new methods and metrics are necessary in order to independently assess the efficacy of immunotherapeutic agents, instead of subjecting them to the same criteria used to evaluate anti-proliferative or anti-angiogenic agents.

While significant strides have been made, there continues to be limited information on consensus biomarkers that correlate with the efficacy of immunotherapy. For example, the induction of optimal anti-tumor immunity through the CTLA-4 antibody seems to correlate with CD278 (ICOS) expression on T-cells (Fu, He, & Sharma, 2011). At the same time, CD279 (PD-1) expression on the same cells inversely correlates with efficacy and has been suggested as an indicator of poor prognosis (Disis, 2010). Therefore, the assays developed here represent efforts to assess vaccine efficacy and response to immunotherapy, informed through current understanding of tumor immunology or clinical trials involving other FDA-approved immunotherapeutic agents (Maecker, McCoy, & Nussenblatt, 2012; Mitchell et al., 2008; Perfetto, et al., 2004; Pritchard, et al., 2012; Ruffell et al., 2012).

The current 13-marker flow cytometry panel enables the gating of leukocytic subtypes (CD45) for the classification of multiple T-cell subtypes (CD3, CD4, CD8, CD25, CD45RA, CD56, CD127, CD197) and the quantification of activation states (CD28, CD278, CD279, HLA-DR) of these cells in clinical trials patients. The phenotyping markers were selected based on current understanding of different T-cell subtypes identified by the Human Immunology Project Consortium (Maecker, et al., 2012). The activation markers were chosen because of their central roles as part

of various T-cell activation cascades (CD28, CD278, CD279) (Boise, et al., 1995; Freeman, et al., 2000; Fu, et al., 2011; Hutloff, et al., 1999; Sharpe & Freeman, 2002) or in antigen cross-presentation and T-cell priming (HLA-DR) (Choi, et al., 2011). Therefore, the panel (Table 6) represents biomarkers currently known to play roles in anti-tumor responses elicited by other immunotherapeutic agents.

While many other markers exist that would also be interesting to include in this panel, conventional flow cytometry suffers from the need to compensate for spectral overlap of various fluorophores (Perfetto, et al., 2004). The recent advent of mass cytometry (CyTOF) bypasses the need to 'compensate' because cellular biomarkers are quantified using antibodies tagged with lanthanide metals not typically found in living systems above trace background levels. Labeled cells are then injected into a mass spectrometer, which quantifies the amount of metals present (Bendall et al., 2011). To date, others have used CyTOF to quantify 30 biomarkers at single-cell resolutions, although theoretically, much higher parallelization is possible (Bendall, et al., 2011).

At the same time, there is also a pressing need to discover other markers that correlate with vaccine response. In the HER2/*neu* clinical trial noted earlier, all patients were treated concurrently with trastuzumab and a HER2/*neu* peptide vaccine, which boosted anti-tumor immunity and promoted long-term survival in a small subset of patients (Figure 35) (Disis, et al., 2009). Because some patients did not respond to treatment, and PBMCs were collected from the patients over a long-term follow-up period, this study provided a sample set that allows us to probe for biomarkers that were upregulated in the responders over the course of treatment,

and also biomarkers that were differentially regulated between the responders and non-responders. As this study is ongoing, it has potential to improve our ability to more accurately assess patient responses to treatment with cancer immunotherapies. It will also potentially lead to the identification of biomarkers that enable prediction of response or non-response in the patients, allowing for further treatments to be discontinued if they are unlikely to benefit the patients.

Summary

T-cells form the most potent effector arms of the immune system, and it is believed that effective cancer immunotherapies will require the elicitation of strong, anti-tumor T-cells. In this chapter, T-cell-centric assays were developed that enable (1) phenotyping and analysis of T-cell activation via flow cytometry and (2) the discovery of regulatory biomarkers (miRNA or mRNA) that are selectively upregulated in cancer patients that responded well to concurrent trastuzumab and HER2/*neu* vaccine treatment. These assays represent current understanding of the assessment of the responses of cancer patients to immunotherapy, while seeking to push the boundaries of understanding by providing novel, robust biomarkers for these purposes.

CHAPTER VII

SYNOPSIS AND CONCLUSIONS

In my dissertation work, we worked towards the development of novel nanomaterials for the delivery of immunotherapeutics in cancer patients. The ultimate goal was to overcome the immunosuppressive tumor environment and re-activate immune responses in breast cancer patients, which has promise in promoting long-term immunity from phenotypically similar cancer cells, by leveraging the immune system's ability to 'remember' past challengers. In particular, I focused on the macrophage, which can become hijacked in the context of a tumor into promoting tumor growth and invasiveness. While we have not yet identified the best drug candidates to enable reprogramming of the tumor-associated macrophages, my work has enables us to take strides in other ways.

First, I identified design parameters that governed nanoparticle-macrophage interactions, with a focus on nanoparticle size and charge. I found that PEGylated nanoparticles are internalized by macrophages in a size-dependent fashion for diameters between 30-100 nm. Charge-uptake relationships were investigated by varying the surface properties of nanoparticles. However, within the ranges investigated, nanoparticle size, not charge, is a stronger determinant of non-specific uptake by macrophages. The results presented here inform the design of nanoparticles to target or evade macrophages in future *in vivo* applications.

With this evidence, I designed the mannosylated nanoparticles to exhibit a 30-40 nm diameter in order to discourage non-specific recognition by macrophages. The nanoparticles were mannosylated in order to encourage mannose receptor-mediated uptake mechanisms, which are primarily present on macrophages and antigen-presenting cells, but upregulated on tumor-associated macrophages. I showed that this mannose layer led to improved siRNA delivery into primary macrophages. The delivered siRNA also retains its activity and successfully facilitates knockdown of a model gene in these cells, which are known to be notoriously difficult-to-transfect stably. I also showed that these cells appear to target tumor-associated macrophages in a spontaneously-arising primary mammary murine tumor model.

For applications where long-term stable transfections may be desirable, I also designed polymeric scaffolds crosslinked with proline oligomers, which can be actively degraded by environmental ROS to release biologics and other encapsulated active agents. Other work in our group shows that nanoparticle-mediated siRNA delivery can be accomplished by encapsulating siRNA-loaded nanoparticles in degradable scaffolds (C. E. Nelson, et al., 2012).

To summarize, in this work, I identified nanoparticle size ranges ideal for the reduction of non-specific uptake of injected nanomaterials into resident macrophages in the body (< 50 nm diameter; Chapter II), synthesized mannosylated nanoparticles that enable siRNA-mediated knockdown of target gene expression in primary macrophages (Chapter III), created polymeric scaffolds that respond to environmental ROS, which may be loaded with such nanoparticles to enable long-

term modulation of macrophage function (Chapter IV), evaluated TAM-specific targeting of the nanoparticles in an *in vivo* tumor model (Chapter V), and designed of T-cell-based assays to enable the characterization of the efficacy of immunotherapies in clinical trial patients (Chapter VI). Taken together, this work provides a framework to enable us to interrogate TAM function and activity in pre-clinical models, with the goals of identifying drugs that can reprogram TAMs into exerting anti-tumor functions. Downstream, if the agents developed here were to become the centerpiece of a clinical trial, we have designed assays that may enable us to quantify the wider effects of TAM-centric immunotherapy on T-cells and in mediating T-cell-mediated immunity in the patients.

Moving from here, significant challenges exist for future work by my successors and other future lab members, including (1) the identification of immunotherapeutic agents—small molecules or peptides or nucleic acids, that can reprogram TAMs into combating tumors, (2) optimization of nanoparticle properties for efficient *in vivo* targeting of TAMs within primary and metastatic tumor sites, (3) the creation of new *in vitro* assays to evaluate and characterize the serum stability of nanoparticles and their interactions with blood cells in circulation, and (4) the optimization of the assays shown in Chapter VI to facilitate their adoption into other immunotherapeutic clinical trials and studies.

Today, cancer immunotherapy remains a burgeoning and promising area for further study across both academic and industrial labs, following the recent FDA approvals of the agents Provenge (Sipuleucel-T; Dendreon) and Yervoy (ipilimumab; Bristol-Myers Squibb) (Mellman, et al., 2011). The development of this field will

continue to require novel approaches to optimally and robustly promote anti-tumor immunity, as well as reliable and accurate assays and methods to characterize that immune response.

APPENDIX A

MANUSCRIPTS PUBLISHED AND CANDIDATE'S ROLES

1. **S.S. Yu**, C.M. Lau, W.J. Barham, H.M. Onishko, C.E. Nelson, H. Li, F.E. Yull, C.L. Duvall, & T.D. Giorgio. (2012) "Macrophage-Specific RNAi Targeting via 'Click', Mannosylated Polymeric Micelles." *Molecular Pharmaceutics* (Under Revision).
    - Designed, planned, and carried out all experiments and measurements with the assistance of C.M.L.
    - Analyzed all data.
    - Wrote the manuscript
    - Formulated the idea for and wrote the grant that led to the 2009 DoD BCRP Concept Award that funded this project.

2. H. Li, **S.S. Yu**, M. Miteva, C.E. Nelson, T. Werfel, T.D. Giorgio, & C.L. Duvall. (2012) "Matrix Metalloproteinase-Responsive, Proximity-Activated Targeting Polymeric Nanoparticles for siRNA Delivery." *Advanced Functional Materials* (Under Revision).
    - Provided extensive technical input for the synthesis and purification of the polymers and peptide-polymer conjugates.
    - Assisted in the design and planning of *in vitro* experiments.
    - Performed confocal microscopy.

- Co-developed the idea and co-wrote the grant proposal that led to the 2010 BCRP Idea Award that funds this project.

3. B.C. Evans, C.E. Nelson, **S.S. Yu**, A.J. Kim, H. Li, T.D. Giorgio, & C.L. Duvall. (2012) "Ex Vivo Red Blood Cell Hemolysis Assay for the Evaluation of pH-responsive Endosomolytic Agents for Cytosolic Delivery of Biomacromolecular Drugs." *J. Visualized Exp* (in press).
    - Wrote the IRB protocol that enabled us to do these studies in our lab.
    - Performed the experiments with help from co-authors.
    - Wrote the manuscript.
    - Provided input and suggestions for the video component of the submission, which was managed by BCE and CEN.

4. A.L. Zachman, S.W. Crowder, O. Ortiz, K.J. Zienkiewicz, C.M. Bronikowski, **S.S. Yu**, T.D. Giorgio, S.A. Guelcher, J.B. Kohn, & H.J. Sung. (2012) "Pro-angiogenic and anti-inflammatory regulation by functional peptides loaded in polymeric implants for soft tissue regeneration." *Tissue Engineering* (in press).
    - Performed immunoassays and flow cytometry experiments for characterization of macrophage behavior and polarization.
    - Consultant for the design of experiments to characterize macrophages and immune response.
    - Co-wrote the Results and Discussion sections of the manuscript.

5. H. Li, **S.S. Yu**, M. Miteva, C.E. Nelson, T.D. Giorgio, & C.L. Duvall. (2012) "Matrix Metalloproteinase Responsive, Proximity-Activated Targeting Polymeric Nanoparticles for siRNA Delivery to Tumor Metastases." *Molecular Therapy* 20: S266.

    - See publication #2 above.

6. **S.S. Yu**, C.M. Lau, S.N. Thomas, W.G. Jerome, D.J. Maron, J.H. Dickerson, J.A. Hubbell, & T.D. Giorgio. (2012) "Size- and Charge-Dependent Non-Specific Uptake of PEGylated Nanoparticles by Macrophages." *Int J Nanomedicine* 7: 799-813.

    - Designed, planned, and carried out all experiments.
    - Managed and analyzed all data.
    - Wrote the manuscript.

7. **S.S. Yu**, R.L. Koblin, A.L. Zachman, D.S. Perrien, L.H. Hofmeister, T.D. Giorgio, & H.J. Sung. (2011) "Physiologically Relevant Oxidative Degradation of Oligo(proline)-Cross-linked Polymeric Scaffolds." *Biomacromolecules* 12(12): 4357-4366.

    - Designed, planned, and carried out all experiments.
    - Managed and analyzed all data.
    - Wrote the manuscript.

8. M.K. Gupta, J.M. Walthal, R. Venkataraman, S.W. Crowder, D.K. Jung, **S.S. Yu**, T.K. Feaster, T.D. Giorgio, C.C. Hong, F.J. Baudenbacher, A.K. Hatzopoulos, & H.J. Sung. (2011) "Combinatorial Electrospun Matrices Promote Physiologically-Relevant Cardiomyogenic Stem Cell Differentiation." *PLoS ONE* 6(12): e28935.
    - Optimized the electrospinning protocol that enabled all of the studies documented in this paper.
    - Consultant for biological data interpretation.
    - Edited the manuscript.

9. **S.S. Yu**, R.A. Ortega, B.W. Reagan, J.A. McPherson, H.J. Sung, & T.D. Giorgio. (2011) "Emerging applications of nanotechnology for the diagnosis and management of vulnerable atherosclerotic plaques." *Wiley Interdiscip Rev Nanomed Nanobiotechnol* 3(6): 620-646.
    - Assembled the team of authors and coordinated writing assignments for various sections.
    - Wrote 60% of the manuscript.
    - Edited and compiled all of the pieces of writing into the cohesive manuscript that was ultimately submitted.

10. C.S. Bell, **S.S. Yu**, & T.D. Giorgio. (2011) "The MultiStrata Nanoparticle: A FeOx/Au Core/Shell Enveloped in a Silica-Gold Shell." Small 7(9): 1158-1162.
    - Consultant for the design and synthesis of the nanoparticles; co-developed synthetic scheme with CSB.

11. **S.S. Yu**, R.L. Scherer, R.A. Ortega, C.S. Bell, C.P. O'Neil, J.A. Hubbell, & T.D. Giorgio. (2011) "PPS-b-PEG block copolymers for the encapsulation of ultrasmall superparamagnetic iron oxides (USPIOs)." *J. Nanobiotechnology* 9:7.
    - Designed, planned, and carried out all experiments.
    - Managed and analyzed all data.
    - Wrote the manuscript.

12. S.N. Thomas, C.P. O'Neil, A.J. van der Vlies, **S.S. Yu**, T.D. Giorgio, M.A. Swartz, & J.A. Hubbell. (2011) "Engineering complement activation on polypropylene sulfide vaccine nanoparticles." *Biomaterials* 32(8): 2194-3303.
    - Synthesized all iron oxide nanoparticles used in this work.
    - Wrote relevant Materials & Methods sections.
    - Edited the manuscript.

BIBLIOGRAPHY

Alexis, F., Pridgen, E., Molnar, L. K., & Farokhzad, O. C. (2008). Factors affecting the clearance and biodistribution of polymeric nanoparticles. *Molecular Pharmaceutics, 5*(4), 505-515.

Ali, S. A. M., Doherty, P. J., & Williams, D. F. (1994). The mechanisms of oxidative degradation of biomedical polymers by free radicals. *Journal of Applied Polymer Science, 51*(8), 1389-1398.

Amici, A., Levine, R. L., Tsai, L., & Stadtman, E. R. (1989). Conversion of amino acid residues in proteins and amino acid homopolymers to carbonyl derivatives by metal-catalyzed oxidation reactions. *J Biol Chem, 264*(6), 3341-3346.

An, S. G., & Cho, C. G. (2004). Synthesis and Characterization of Amphiphilic Poly(caprolactone) Star Block Copolymers. *Macromolecular Rapid Communications, 25*(5), 618-622.

Azuma, H., & Tilney, N. L. (1994). Chronic graft rejection. *Current Opinion in Immunology, 6*(5), 770-776.

Bastús, N. G., Sánchez-Tilló, E., Pujals, S., Farrera, C., López, C., Giralt, E., et al. (2009). Homogeneous Conjugation of Peptides onto Gold Nanoparticles Enhances Macrophage Response. *Acs Nano, 3*(6), 1335-1344.

Bendall, S. C., Simonds, E. F., Qiu, P., Amir el, A. D., Krutzik, P. O., Finck, R., et al. (2011). Single-cell mass cytometry of differential immune and drug responses across a human hematopoietic continuum. *Science, 332*(6030), 687-696.

Benoit, D. S. W., Srinivasan, S., Shubin, A. D., & Stayton, P. S. (2011). Synthesis of Folate-Functionalized RAFT Polymers for Targeted siRNA Delivery. *Biomacromolecules, 12*(7), 2708-2714.

Berlett, B. S., & Stadtman, E. R. (1997). Protein oxidation in aging, disease, and oxidative stress. *J Biol Chem, 272*(33), 20313-20316.

Boise, L. H., Minn, A. J., Noel, P. J., June, C. H., Accavitti, M. A., Lindsten, T., et al. (1995). CD28 costimulation can promote T cell survival by enhancing the expression of Bcl-XL. *Immunity, 3*(1), 87-98.

Bolte, S., & CordeliÈRes, F. P. (2006). A guided tour into subcellular colocalization analysis in light microscopy. *Journal of Microscopy, 224*(3), 213-232.

Bonizzi, G., & Karin, M. (2004). The two NF-kappaB activation pathways and their role in innate and adaptive immunity. *Trends Immunol, 25*(6), 280-288.

Bouwens, L., Baekeland, M., de Zanger, R., & Wisse, E. (1986). Quantitation, tissue distribution and proliferation kinetics of kupffer cells in normal rat liver. *Hepatology, 6*(4), 718-722.

Boyer, C., Bulmus, V., Davis, T. P., Ladmiral, V., Liu, J., & Perrier, S. (2009). Bioapplications of RAFT polymerization. *Chem Rev, 109*(11), 5402-5436.

Brancato, S. K., & Albina, J. E. (2011). Wound macrophages as key regulators of repair: origin, phenotype, and function. *The American journal of pathology, 178*(1), 19-25.

Briley-Saebo, K. C., Cho, Y. S., Shaw, P. X., Ryu, S. K., Mani, V., Dickson, S., et al. (2011). Targeted Iron Oxide Particles for In Vivo Magnetic Resonance Detection of

Atherosclerotic Lesions With Antibodies Directed to Oxidation-Specific Epitopes. *J Am Coll Cardiol, 57*(3), 337-347.
Brown, M. S., & Goldstein, J. L. (1983). Lipoprotein metabolism in the macrophage: implications for cholesterol deposition in atherosclerosis. *Annu Rev Biochem, 52*, 223-261.
Cammas, S., Suzuki, K., Sone, C., Sakurai, Y., Kataoka, K., & Okano, T. (1997). Thermo-responsive polymer nanoparticles with a core-shell micelle structure as site-specific drug carriers. *Journal of Controlled Release, 48*(2-3), 157-164.
Cao, Y., Bonizzi, G., Seagroves, T. N., Greten, F. R., Johnson, R., Schmidt, E. V., et al. (2001). IKKalpha provides an essential link between RANK signaling and cyclin D1 expression during mammary gland development. *Cell, 107*(6), 763-775.
Cao, Y., & Karin, M. (2003a). NF-kappaB in mammary gland development and breast cancer. *J Mammary Gland Biol Neoplasia, 8*(2), 215-223.
Cao, Y., & Karin, M. (2003b). NF-kappaB in mammary gland development and breast cancer. *Journal of mammary gland biology and neoplasia, 8*(2), 215-223.
Caspi, R. R. (2008). Immunotherapy of autoimmunity and cancer: the penalty for success. *Nat Rev Immunol, 8*(12), 970-976.
Chan, W. C., & White, P. D. (2000). *Fmoc solid phase peptide synthesis : a practical approach*. Oxford ; New York: Oxford University Press.
Chnari, E., Nikitczuk, J. S., Wang, J., Uhrich, K. E., & Moghe, P. V. (2006). Engineered Polymeric Nanoparticles for Receptor-Targeted Blockage of Oxidized Low Density Lipoprotein Uptake and Atherogenesis in Macrophages. *Biomacromolecules, 7*(6), 1796-1805.
Choi, N. M., Majumder, P., & Boss, J. M. (2011). Regulation of major histocompatibility complex class II genes. *Current Opinion in Immunology, 23*(1), 81-87.
Christian, G. D. (1994). *Analytical chemistry* (5th ed.). New York: Wiley & Sons.
Cogswell, P. C., Guttridge, D. C., Funkhouser, W. K., & Baldwin, A. S., Jr. (2000). Selective activation of NF-kappa B subunits in human breast cancer: potential roles for NF-kappa B2/p52 and for Bcl-3. *Oncogene, 19*(9), 1123-1131.
Connelly, L., Barham, W., Onishko, H. M., Chen, L., Sherrill, T. P., Zabuawala, T., et al. (2011). NF-kappaB activation within macrophages leads to an anti-tumor phenotype in a mammary tumor lung metastasis model. *Breast cancer research : BCR, 13*(4), R83.
Connelly, L., Jacobs, A. T., Palacios-Callender, M., Moncada, S., & Hobbs, A. J. (2003). Macrophage endothelial nitric-oxide synthase autoregulates cellular activation and pro-inflammatory protein expression. *J Biol Chem, 278*(29), 26480-26487.
Convertine, A. J., Benoit, D. S., Duvall, C. L., Hoffman, A. S., & Stayton, P. S. (2009). Development of a novel endosomolytic diblock copolymer for siRNA delivery. *J Control Release, 133*(3), 221-229.
Cormode, D. P., Briley-Saebo, K. C., Mulder, W. J., Aguinaldo, J. G., Barazza, A., Ma, Y., et al. (2008). An ApoA-I mimetic peptide high-density-lipoprotein-based MRI contrast agent for atherosclerotic plaque composition detection. *Small, 4*(9), 1437-1444.

Cormode, D. P., Skajaa, T., van Schooneveld, M. M., Koole, R., Jarzyna, P., Lobatto, M. E., et al. (2008). Nanocrystal core high-density lipoproteins: a multimodality contrast agent platform. *Nano Lett, 8*(11), 3715-3723.

Crowder, S. W., Gupta, M. K., Hofmeister, L. H., Zachman, A. L., & Sung, H.-J. (2011). Modular polymer design to regulate phenotype and oxidative response of human coronary artery cells for potential stent coating applications. *Acta Biomaterialia, in press*(0).

Crownover, E., Duvall, C. L., Convertine, A., Hoffman, A. S., & Stayton, P. S. (2011). RAFT-synthesized graft copolymers that enhance pH-dependent membrane destabilization and protein circulation times. *Journal of controlled release : official journal of the Controlled Release Society, 155*(2), 167-174.

Daldrup-Link, H. E., Golovko, D., Ruffel, B., DeNardo, D., Castaneda, R., Ansari, C., et al. (2011). MR Imaging of Tumor Associated Macrophages with Clinically-Applicable Iron Oxide Nanoparticles. *Clinical Cancer Research*.

de Nooijer, R., Verkleij, C. J., von der Thusen, J. H., Jukema, J. W., van der Wall, E. E., van Berkel, T. J., et al. (2006). Lesional overexpression of matrix metalloproteinase-9 promotes intraplaque hemorrhage in advanced lesions but not at earlier stages of atherogenesis. *Arterioscler Thromb Vasc Biol, 26*(2), 340-346.

de Visser, K. E., Eichten, A., & Coussens, L. M. (2006). Paradoxical roles of the immune system during cancer development. *Nat Rev Cancer, 6*(1), 24-37.

Deguchi, J. O., Aikawa, M., Tung, C. H., Aikawa, E., Kim, D. E., Ntziachristos, V., et al. (2006). Inflammation in atherosclerosis: visualizing matrix metalloproteinase action in macrophages in vivo. *Circulation, 114*(1), 55-62.

Dejardin, E., Bonizzi, G., Bellahcene, A., Castronovo, V., Merville, M. P., & Bours, V. (1995). Highly-expressed p100/p52 (NFKB2) sequesters other NF-kappa B-related proteins in the cytoplasm of human breast cancer cells. *Oncogene, 11*(9), 1835-1841.

DeLong, S. A., Gobin, A. S., & West, J. L. (2005). Covalent immobilization of RGDS on hydrogel surfaces to direct cell alignment and migration. *J Control Release, 109*(1-3), 139-148.

DeNardo, D. G., Brennan, D. J., Rexhepaj, E., Ruffell, B., Shiao, S. L., Madden, S. F., et al. (2011). Leukocyte Complexity Predicts Breast Cancer Survival and Functionally Regulates Response to Chemotherapy. *Cancer Discovery, 1*(1), 54-67.

Devaraj, S., & Jialal, I. (2011). C-Reactive Protein Polarizes Human Macrophages to an M1 Phenotype and Inhibits Transformation to the M2 Phenotype. *Arterioscler Thromb Vasc Biol*, ATVBAHA.111.225508.

Dirkx, A. E., Oude Egbrink, M. G., Wagstaff, J., & Griffioen, A. W. (2006). Monocyte/macrophage infiltration in tumors: modulators of angiogenesis. *J Leukoc Biol, 80*(6), 1183-1196.

Disis, M. L. (2010). Immune Regulation of Cancer. *Journal of Clinical Oncology, 28*(29), 4531-4538.

Disis, M. L., Wallace, D. R., Gooley, T. A., Dang, Y., Slota, M., Lu, H., et al. (2009). Concurrent Trastuzumab and HER2/neu-Specific Vaccination in Patients

With Metastatic Breast Cancer. *Journal of Clinical Oncology, 27*(28), 4685-4692.
Doshi, N., & Mitragotri, S. (2010). Macrophages recognize size and shape of their targets. *PLoS One, 5*(4), e10051.
Duvall, C. L., Convertine, A. J., Benoit, D. S., Hoffman, A. S., & Stayton, P. S. (2010). Intracellular Delivery of a Proapoptotic Peptide via Conjugation to a RAFT Synthesized Endosomolytic Polymer. *Mol Pharm, 7*(2), 468-476.
East, L., & Isacke, C. M. (2002). The mannose receptor family. *Biochimica et Biophysica Acta (BBA) - General Subjects, 1572*(2–3), 364-386.
Ece Gamsiz, D., Shah, L. K., Devalapally, H., Amiji, M. M., & Carrier, R. L. (2008). A model predicting delivery of saquinavir in nanoparticles to human monocyte/macrophage (Mo/Mac) cells. *Biotechnol Bioeng, 101*(5), 1072-1082.
Eliopoulos, A. G., Caamano, J. H., Flavell, J., Reynolds, G. M., Murray, P. G., Poyet, J. L., et al. (2003). Epstein-Barr virus-encoded latent infection membrane protein 1 regulates the processing of p100 NF-kappaB2 to p52 via an IKKgamma/NEMO-independent signalling pathway. *Oncogene, 22*(48), 7557-7569.
Espuelas, S., Thumann, C., Heurtault, B. a., Schuber, F., & Frisch, B. (2008). Influence of Ligand Valency on the Targeting of Immature Human Dendritic Cells by Mannosylated Liposomes. *Bioconjugate Chemistry, 19*(12), 2385-2393.
Evans, B. C., Nelson, C. E., Yu, S. S., Kim, A. J., Li, H., Nelson, H. M., et al. (2012). Ex Vivo Red Blood Cell Hemolysis Assay for the Evaluation of pH-responsive Endosomolytic Agents for Cytosolic Delivery of Biomacromolecular Drugs. *J Vis Exp, in press*.
Everhart, M. B., Han, W., Sherrill, T. P., Arutiunov, M., Polosukhin, V. V., Burke, J. R., et al. (2006). Duration and intensity of NF-kappaB activity determine the severity of endotoxin-induced acute lung injury. *J Immunol, 176*(8), 4995-5005.
Fako, V. E., & Furgeson, D. Y. (2009). Zebrafish as a correlative and predictive model for assessing biomaterial nanotoxicity. *Advanced Drug Delivery Reviews, 61*(6), 478-486.
Fattori, R., & Piva, T. (2003). Drug-eluting stents in vascular intervention. *Lancet, 361*(9353), 247-249.
Felix, R., Cecchini, M. G., Hofstetter, W., Elford, P. R., Stutzer, A., & Fleisch, H. (1990). Rapid publication: Impairment of macrophage colony-stimulating factor production and lack of resident bone marrow macrophages in the osteopetrotic op/op Mouse. *Journal of Bone and Mineral Research, 5*(7), 781-789.
Fire, A., Xu, S., Montgomery, M. K., Kostas, S. A., Driver, S. E., & Mello, C. C. (1998). Potent and specific genetic interference by double-stranded RNA in Caenorhabditis elegans. *Nature, 391*(6669), 806-811.
Fogal, V., Zhang, L., Krajewski, S., & Ruoslahti, E. (2008). Mitochondrial/cell-surface protein p32/gC1qR as a molecular target in tumor cells and tumor stroma. *Cancer research, 68*(17), 7210-7218.

Freeman, G. J., Long, A. J., Iwai, Y., Bourque, K., Chernova, T., Nishimura, H., et al. (2000). Engagement of the PD-1 Immunoinhibitory Receptor by a Novel B7 Family Member Leads to Negative Regulation of Lymphocyte Activation. *The Journal of Experimental Medicine, 192*(7), 1027-1034.

Frias, J. C., Ma, Y., Williams, K. J., Fayad, Z. A., & Fisher, E. A. (2006). Properties of a versatile nanoparticle platform contrast agent to image and characterize atherosclerotic plaques by magnetic resonance imaging. *Nano Lett, 6*(10), 2220-2224.

Fridman, W. H., Pages, F., Sautes-Fridman, C., & Galon, J. (2012). The immune contexture in human tumours: impact on clinical outcome. *Nature Reviews Cancer, 12*(4), 298-306.

Fu, T., He, Q., & Sharma, P. (2011). The ICOS/ICOSL Pathway Is Required for Optimal Antitumor Responses Mediated by Anti–CTLA-4 Therapy. *Cancer Research, 71*(16), 5445-5454.

Galis, Z. S., Sukhova, G. K., Lark, M. W., & Libby, P. (1994). Increased expression of matrix metalloproteinases and matrix degrading activity in vulnerable regions of human atherosclerotic plaques. *J Clin Invest, 94*(6), 2493-2503.

Gimenez, S., Ponsart, S., Coudane, J., & Vert, M. (2001). Synthesis, properties and in vitro degradation of carboxyl-bearing PCL. *Journal of Bioactive and Compatible Polymers, 16*(1), 32-46.

Gleissner, C. A., Shaked, I., Little, K. M., & Ley, K. (2010). CXC Chemokine Ligand 4 Induces a Unique Transcriptome in Monocyte-Derived Macrophages. *The Journal of Immunology, 184*(9), 4810-4818.

Gordon, S. (2003). Alternative activation of macrophages. *Nature reviews. Immunology, 3*(1), 23-35.

Gough, P. J., Gomez, I. G., Wille, P. T., & Raines, E. W. (2006). Macrophage expression of active MMP-9 induces acute plaque disruption in apoE-deficient mice. *J Clin Invest, 116*(1), 59-69.

Griffin, E. E., Ullery, J. C., Cox, B. E., & Jerome, W. G. (2005). Aggregated LDL and lipid dispersions induce lysosomal cholesteryl ester accumulation in macrophage foam cells. *Journal of lipid research, 46*(10), 2052-2060.

Guiducci, C., Vicari, A. P., Sangaletti, S., Trinchieri, G., & Colombo, M. P. (2005). Redirecting in vivo elicited tumor infiltrating macrophages and dendritic cells towards tumor rejection. *Cancer Res, 65*(8), 3437-3446.

Gupta, P., Vermani, K., & Garg, S. (2002). Hydrogels: from controlled release to pH-responsive drug delivery. *Drug Discovery Today, 7*(10), 569-579.

Guy, C. T., Cardiff, R. D., & Muller, W. J. (1992). Induction of mammary tumors by expression of polyomavirus middle T oncogene: a transgenic mouse model for metastatic disease. *Mol Cell Biol, 12*(3), 954-961.

Hagemann, T., Lawrence, T., McNeish, I., Charles, K. A., Kulbe, H., Thompson, R. G., et al. (2008). "Re-educating" tumor-associated macrophages by targeting NF-kappaB. *J Exp Med, 205*(6), 1261-1268.

Halliwell, B., Clement, M. V., & Long, L. H. (2000). Hydrogen peroxide in the human body. *FEBS letters, 486*(1), 10-13.

Han, F., Li, S., Yin, R., Liu, H., & Xu, L. (2008). Effect of surfactants on the formation and characterization of a new type of colloidal drug delivery system:

Nanostructured lipid carriers. *Colloids and Surfaces A: Physicochemical and Engineering Aspects, 315*(1-3), 210-216.
Hartigan-O'Connor, D. J., Poon, C., Sinclair, E., & McCune, J. M. (2007). Human CD4+ regulatory T cells express lower levels of the IL-7 receptor alpha chain (CD127), allowing consistent identification and sorting of live cells. *Journal of Immunological Methods, 319*(1–2), 41-52.
Henry, S. M., Convertine, A. J., Benoit, D. S., Hoffman, A. S., & Stayton, P. S. (2009). End-functionalized polymers and junction-functionalized diblock copolymers via RAFT chain extension with maleimido monomers. *Bioconjug Chem, 20*(6), 1122-1128.
Herman, M. P., Sukhova, G. K., Libby, P., Gerdes, N., Tang, N., Horton, D. B., et al. (2001). Expression of neutrophil collagenase (matrix metalloproteinase-8) in human atheroma: a novel collagenolytic pathway suggested by transcriptional profiling. *Circulation, 104*(16), 1899-1904.
Hermanson, G. T. (2008 (2nd ed.)). *Bioconjugate Techniques*. San Diego: Academic Press.
Hildebrand, T., & Ruegsegger, P. (1997). A new method for the model-independent assessment of thickness in three-dimensional images. *Journal of Microscopy-Oxford, 185*, 67-75.
Hirose, K., Iwabuchi, K., Shimada, K., Kiyanagi, T., Iwahara, C., Nakayama, H., et al. (2011). Different responses to oxidized low-density lipoproteins in human polarized macrophages. *Lipids in health and disease, 10*, 1.
Hogg, N., Darley-Usmar, V. M., Wilson, M. T., & Moncada, S. (1992). Production of hydroxyl radicals from the simultaneous generation of superoxide and nitric oxide. *Biochem. J., 281*(2), 419-424.
Hutloff, A., Dittrich, A. M., Beier, K. C., Eljaschewitsch, B., Kraft, R., Anagnostopoulos, I., et al. (1999). ICOS is an inducible T-cell co-stimulator structurally and functionally related to CD28. *Nature, 397*, 263-266.
Immunotherapy Network Launches First Trial. (2012). *Cancer Discovery*.
Insull, W., Jr. (2009). The pathology of atherosclerosis: plaque development and plaque responses to medical treatment. *Am J Med, 122*(1 Suppl), S3-S14.
Jerome, W. G., Cox, B. E., Griffin, E. E., & Ullery, J. C. (2008). Lysosomal cholesterol accumulation inhibits subsequent hydrolysis of lipoprotein cholesteryl ester. *Microscopy and microanalysis : the official journal of Microscopy Society of America, Microbeam Analysis Society, Microscopical Society of Canada, 14*(2), 138-149.
Johnson, C., Sung, H. J., Lessner, S. M., Fini, M. E., & Galis, Z. S. (2004). Matrix metalloproteinase-9 is required for adequate angiogenic revascularization of ischemic tissues: potential role in capillary branching. *Circ Res, 94*(2), 262-268.
Jones, C. F., Campbell, R. A., Franks, Z., Gibson, C. C., Thiagarajan, G., Vieira-de-Abreu, A., et al. (2012). Cationic PAMAM Dendrimers Disrupt Key Platelet Functions. *Molecular Pharmaceutics, 9*(6), 1599-1611.
Joyce, J. A., & Pollard, J. W. (2009). Microenvironmental regulation of metastasis. *Nat Rev Cancer, 9*(4), 239-252.

Kindt, T. J., Goldsby, R. A., Osborne, B. A., & Kuby, J. (2007). *Kuby immunology* (6th ed.). New York: W.H. Freeman.

Kirkland-York, S., Zhang, Y., Smith, A. E., York, A. W., Huang, F., & McCormick, C. L. (2010). Tailored design of Au nanoparticle-siRNA carriers utilizing reversible addition-fragmentation chain transfer polymers. *Biomacromolecules, 11*(4), 1052-1059.

Kolb, H. C., & Sharpless, K. B. (2003). The growing impact of click chemistry on drug discovery. *Drug Discovery Today, 8*(24), 1128-1137.

Kortylewski, M., Swiderski, P., Herrmann, A., Wang, L., Kowolik, C., Kujawski, M., et al. (2009). In vivo delivery of siRNA to immune cells by conjugation to a TLR9 agonist enhances antitumor immune responses. *Nat Biotechnol, 27*(10), 925-932.

Kumari, A., Yadav, S. K., & Yadav, S. C. (2010). Biodegradable polymeric nanoparticles based drug delivery systems. *Colloids and Surfaces B: Biointerfaces, 75*(1), 1-18.

Laakkonen, P., Porkka, K., Hoffman, J. A., & Ruoslahti, E. (2002). A tumor-homing peptide with a targeting specificity related to lymphatic vessels. *Nature medicine, 8*(7), 751-755.

Lanier, L. L., Testi, R., Bindl, J., & Phillips, J. H. (1989). Identity of Leu-19 (CD56) leukocyte differentiation antigen and neural cell adhesion molecule. *The Journal of Experimental Medicine, 169*(6), 2233-2238.

Larsen, E. K., Nielsen, T., Wittenborn, T., Birkedal, H., Vorup-Jensen, T., Jakobsen, M. H., et al. (2009). Size-Dependent Accumulation of PEGylated Silane-Coated Magnetic Iron Oxide Nanoparticles in Murine Tumors. *ACS Nano*.

Laskin, D. L., Weinberger, B., & Laskin, J. D. (2001). Functional heterogeneity in liver and lung macrophages. *Journal of Leukocyte Biology, 70*(2), 163-170.

Li, S. D., & Huang, L. (2009). Nanoparticles evading the reticuloendothelial system: role of the supported bilayer. *Biochim Biophys Acta, 1788*(10), 2259-2266.

Libby, P. (2002). Inflammation in atherosclerosis. *Nature, 420*(6917), 868-874.

Lin, E. Y., Jones, J. G., Li, P., Zhu, L., Whitney, K. D., Muller, W. J., et al. (2003). Progression to malignancy in the polyoma middle T oncoprotein mouse breast cancer model provides a reliable model for human diseases. *Am J Pathol, 163*(5), 2113-2126.

Linehan, S. A., Martinez-Pomares, L., & Gordon, S. (2000). Mannose receptor and scavenger receptor: two macrophage pattern recognition receptors with diverse functions in tissue homeostasis and host defense. *Advances in experimental medicine and biology, 479*, 1-14.

Lipinski, M. J., Amirbekian, V., Frias, J. C., Aguinaldo, J. G., Mani, V., Briley-Saebo, K. C., et al. (2006). MRI to detect atherosclerosis with gadolinium-containing immunomicelles targeting the macrophage scavenger receptor. *Magn Reson Med, 56*(3), 601-610.

Liu, Y., Stewart, K. N., Bishop, E., Marek, C. J., Kluth, D. C., Rees, A. J., et al. (2008). Unique expression of suppressor of cytokine signaling 3 is essential for classical macrophage activation in rodents in vitro and in vivo. *J Immunol, 180*(9), 6270-6278.

Lloyd-Jones, D., Adams, R. J., Brown, T. M., Carnethon, M., Dai, S., De Simone, G., et al. (2010). Heart disease and stroke statistics--2010 update: a report from the American Heart Association. *Circulation, 121*(7), e46-e215.

Luo, Y., Zhou, H., Krueger, J., Kaplan, C., Lee, S.-H., Dolman, C., et al. (2006). Targeting tumor-associated macrophages as a novel strategy against breast cancer. *The Journal of Clinical Investigation, 116*(8), 2132-2141.

Lv, H., Zhang, S., Wang, B., Cui, S., & Yan, J. (2006). Toxicity of cationic lipids and cationic polymers in gene delivery. *Journal of Controlled Release, 114*(1), 100-109.

Maecker, H. T., McCoy, J. P., & Nussenblatt, R. (2012). Standardizing immunophenotyping for the Human Immunology Project. *Nat Rev Immunol, 12*(3), 191-200.

Mahmoud, E. A., Sankaranarayanan, J., Morachis, J. M., Kim, G., & Almutairi, A. (2011). Inflammation responsive logic gate nanoparticles for the delivery of proteins. *Bioconjugate chemistry, 22*(7), 1416-1421.

Mantovani, A., Garlanda, C., & Locati, M. (2009). Macrophage Diversity and Polarization in Atherosclerosis: A Question of Balance. *Arterioscler Thromb Vasc Biol, 29*(10), 1419-1423.

Mantovani, A., Sica, A., & Locati, M. (2005). Macrophage Polarization Comes of Age. *Immunity, 23*(4), 344-346.

Mantovani, A., Sozzani, S., Locati, M., Allavena, P., & Sica, A. (2002). Macrophage polarization: tumor-associated macrophages as a paradigm for polarized M2 mononuclear phagocytes. *Trends Immunol, 23*(11), 549-555.

Martin, P. (1997). Wound Healing--Aiming for Perfect Skin Regeneration. *Science, 276*(5309), 75-81.

Martinez, F. O., Gordon, S., Locati, M., & Mantovani, A. (2006). Transcriptional Profiling of the Human Monocyte-to-Macrophage Differentiation and Polarization: New Molecules and Patterns of Gene Expression. *The Journal of Immunology, 177*(10), 7303-7311.

Massia, S. P., Holecko, M. M., & Ehteshami, G. R. (2004). In vitro assessment of bioactive coatings for neural implant applications. *Journal of Biomedical Materials Research Part A, 68A*(1), 177-186.

McCall, M. R., & Frei, B. (2000). Mechanisms of LDL Oxidation. In J. F. Keaney, Jr. (Ed.), *Oxidative Stress and Vascular Disease* (1st ed., pp. 75-98). Norwell, MA, USA: Kluwer Academic Publishers.

Mellman, I., Coukos, G., & Dranoff, G. (2011). Cancer immunotherapy comes of age. *Nature, 480*(7378), 480-489.

Miller, J. S., Shen, C. J., Legant, W. R., Baranski, J. D., Blakely, B. L., & Chen, C. S. (2010). Bioactive hydrogels made from step-growth derived PEG-peptide macromers. *Biomaterials, 31*(13), 3736-3743.

Miselis, N. R., Wu, Z. J., Van Rooijen, N., & Kane, A. B. (2008). Targeting tumor-associated macrophages in an orthotopic murine model of diffuse malignant mesothelioma. *Mol Cancer Ther, 7*(4), 788-799.

Mitchell, P. S., Parkin, R. K., Kroh, E. M., Fritz, B. R., Wyman, S. K., Pogosova-Agadjanyan, E. L., et al. (2008). Circulating microRNAs as stable blood-based

markers for cancer detection. *Proceedings of the National Academy of Sciences, 105*(30), 10513-10518.
Moilanen, E., Moilanen, T., Knowles, R., Charles, I., Kadoya, Y., al-Saffar, N., et al. (1997). Nitric oxide synthase is expressed in human macrophages during foreign body inflammation. *The American journal of pathology, 150*(3), 881-887.
Morishige, K., Kacher, D. F., Libby, P., Josephson, L., Ganz, P., Weissleder, R., et al. (2010). High-resolution magnetic resonance imaging enhanced with superparamagnetic nanoparticles measures macrophage burden in atherosclerosis. *Circulation, 122*(17), 1707-1715.
Mosser, D. M., & Edwards, J. P. (2008). Exploring the full spectrum of macrophage activation. *Nat Rev Immunol, 8*(12), 958-969.
Muller, K., Skepper, J. N., Posfai, M., Trivedi, R., Howarth, S., Corot, C., et al. (2007). Effect of ultrasmall superparamagnetic iron oxide nanoparticles (Ferumoxtran-10) on human monocyte-macrophages in vitro. *Biomaterials, 28*(9), 1629-1642.
Murdoch, C., Muthana, M., Coffelt, S. B., & Lewis, C. E. (2008). The role of myeloid cells in the promotion of tumour angiogenesis. *Nat Rev Cancer, 8*(8), 618-631.
Murphy, M. P., Packer, M. A., Scarlett, J. L., & Martin, S. W. (1998). Peroxynitrite: A Biologically Significant Oxidant. *General Pharmacology: The Vascular System, 31*(2), 179-186.
Murray, P. J. (2007). The JAK-STAT Signaling Pathway: Input and Output Integration. *The Journal of Immunology, 178*(5), 2623-2629.
Naghavi, M., & Falk, E. (2010). From Vulnerable Plaque to Vulnerable Patient *Asymptomatic Atherosclerosis* (pp. 13-38): Humana Press.
Nakshatri, H., Bhat-Nakshatri, P., Martin, D. A., Goulet, R. J., Jr., & Sledge, G. W., Jr. (1997). Constitutive activation of NF-kappaB during progression of breast cancer to hormone-independent growth. *Mol Cell Biol, 17*(7), 3629-3639.
Napoli, A., Valentini, M., Tirelli, N., Muller, M., & Hubbell, J. A. (2004). Oxidation-responsive polymeric vesicles. *Nat Mater, 3*(3), 183-189.
Nelson, B. H. (2004). IL-2, Regulatory T Cells, and Tolerance. *The Journal of Immunology, 172*(7), 3983-3988.
Nelson, C. E., Gupta, M. K., Adolph, E. J., Shannon, J. M., Guelcher, S. A., & Duvall, C. L. (2012). Sustained local delivery of siRNA from an injectable scaffold. *Biomaterials, 33*(4), 1154-1161.
Palanca-Wessels, M. C., Convertine, A. J., Cutler-Strom, R., Booth, G. C., Lee, F., Berguig, G. Y., et al. (2011). Anti-CD22 antibody targeting of pH-responsive micelles enhances small interfering RNA delivery and gene silencing in lymphoma cells. *Molecular therapy : the journal of the American Society of Gene Therapy, 19*(8), 1529-1537.
Papiernik, M., de Moraes, M. L., Pontoux, C., Vasseur, F., & Pénit, C. (1998). Regulatory CD4 T cells: expression of IL-2R alpha chain, resistance to clonal deletion and IL-2 dependency. *International Immunology, 10*(4), 371-378.
Pardoll, D., & Drake, C. (2012). Immunotherapy earns its spot in the ranks of cancer therapy. *The Journal of Experimental Medicine, 209*(2), 201-209.

Perez, J. M., O'Loughin, T., Simeone, F. J., Weissleder, R., & Josephson, L. (2002). DNA-based magnetic nanoparticle assembly acts as a magnetic relaxation nanoswitch allowing screening of DNA-cleaving agents. *Journal of the American Chemical Society, 124*(12), 2856-2857.

Perfetto, S. P., Chattopadhyay, P. K., & Roederer, M. (2004). Seventeen-colour flow cytometry: unravelling the immune system. *Nat Rev Immunol, 4*(8), 648-655.

Perkins, N. D. (2003). Oncogenes, tumor suppressors and p52 NF-kappaB. *Oncogene, 22*(48), 7553-7556.

Phillips, N. C., & Heydari, C. (1996). Modulation of Cationic Liposomal DNA Zeta Potential and Liposome-protein Interaction by Amphiphilic Poly (ethylene glycol)*. *Pharmacy and Pharmacology Communications, 2*(2), 73-76.

Plotz, P. H., & Rifai, A. (1982). Stable, Soluble, Model Immune-Complexes Made with a Versatile Multivalent Affinity-Labeling Antigen. *Biochemistry, 21*(2), 301-308.

Pluddemann, A., Neyen, C., & Gordon, S. (2007). Macrophage scavenger receptors and host-derived ligands. *Methods, 43*(3), 207-217.

Pollard, J. W. (2008). Macrophages define the invasive microenvironment in breast cancer. *J Leukoc Biol, 84*(3), 623-630.

Porta, C., Rimoldi, M., Raes, G., Brys, L., Ghezzi, P., Di Liberto, D., et al. (2009). Tolerance and M2 (alternative) macrophage polarization are related processes orchestrated by p50 nuclear factor kappaB. *Proceedings of the National Academy of Sciences of the United States of America, 106*(35), 14978-14983.

Pritchard, C. C., Cheng, H. H., & Tewari, M. (2012). MicroRNA profiling: approaches and considerations. *Nature reviews. Genetics, 13*(5), 358-369.

Ratner, B. D. (1996). *Biomaterials science : an introduction to materials in medicine*. San Diego: Academic Press.

Raynal, I., Prigent, P., Peyramaure, S., Najid, A., Rebuzzi, C., & Corot, C. (2004). Macrophage endocytosis of superparamagnetic iron oxide nanoparticles: mechanisms and comparison of ferumoxides and ferumoxtran-10. *Invest Radiol, 39*(1), 56-63.

Reddy, S. T., Rehor, A., Schmoekel, H. G., Hubbell, J. A., & Swartz, M. A. (2006). In vivo targeting of dendritic cells in lymph nodes with poly(propylene sulfide) nanoparticles. *Journal of Controlled Release, 112*(1), 26-34.

Reddy, S. T., van der Vlies, A. J., Simeoni, E., Angeli, V., Randolph, G. J., O'Neil, C. P., et al. (2007). Exploiting lymphatic transport and complement activation in nanoparticle vaccines. *Nat Biotechnol, 25*(10), 1159-1164.

Rehor, A., Hubbell, J. A., & Tirelli, N. (2005). Oxidation-sensitive polymeric nanoparticles. *Langmuir, 21*(1), 411-417.

Rettig, G. R., & Behlke, M. A. (2012). Progress toward in vivo use of siRNAs-II. *Molecular therapy : the journal of the American Society of Gene Therapy, 20*(3), 483-512.

Ribatti, D., Levi-Schaffer, F., & Kovanen, P. T. (2008). Inflammatory angiogenesis in atherogenesis--a double-edged sword. *Ann Med, 40*(8), 606-621.

Romieu-Mourez, R., Landesman-Bollag, E., Seldin, D. C., Traish, A. M., Mercurio, F., & Sonenshein, G. E. (2001). Roles of IKK kinases and protein kinase CK2 in

activation of nuclear factor-kappaB in breast cancer. *Cancer Research, 61*(9), 3810-3818.
Ruegsegger, P., Hildebrand, T., Laib, A., Muller, R., & Dequeker, J. (1999). Direct three-dimensional morphometric analysis of human cancellous bone: Microstructural data from spine, femur, iliac crest, and calcaneus. *Journal of Bone and Mineral Research, 14*(7), 1167-1174.
Ruffell, B., Au, A., Rugo, H. S., Esserman, L. J., Hwang, E. S., & Coussens, L. M. (2012). Leukocyte composition of human breast cancer. *Proceedings of the National Academy of Sciences, 109*(8), 2796-2801.
Saam, T., Hatsukami, T. S., Takaya, N., Chu, B., Underhill, H., Kerwin, W. S., et al. (2007). The vulnerable, or high-risk, atherosclerotic plaque: noninvasive MR imaging for characterization and assessment. *Radiology, 244*(1), 64-77.
Saitoh, T., Nakayama, M., Nakano, H., Yagita, H., Yamamoto, N., & Yamaoka, S. (2003). TWEAK induces NF-kappaB2 p100 processing and long lasting NF-kappaB activation. *J Biol Chem, 278*(38), 36005-36012.
Schellenberger, E., Rudloff, F., Warmuth, C., Taupitz, M., Hamm, B., & Schnorr, J. (2008). Protease-specific nanosensors for magnetic resonance imaging. *Bioconjug Chem, 19*(12), 2440-2445.
Scherer, R. L., McIntyre, J. O., & Matrisian, L. M. (2008). Imaging matrix metalloproteinases in cancer. *Cancer Metastasis Rev, 27*(4), 679-690.
Schmedlen, R. H., Elbjeirami, W. M., Gobin, A. S., & West, J. L. (2003). Tissue engineered small-diameter vascular grafts. *Clin Plast Surg, 30*(4), 507-517.
Schuessler, H., & Schilling, K. (1984). Oxygen Effect in the Radiolysis of Proteins. *International Journal of Radiation Biology, 45*(3), 267-281.
Scott, P. (1993). IL-12: initiation cytokine for cell-mediated immunity. *Science, 260*(5107), 496-497.
Senftleben, U., Cao, Y., Xiao, G., Greten, F. R., Krahn, G., Bonizzi, G., et al. (2001). Activation by IKKalpha of a second, evolutionary conserved, NF-kappa B signaling pathway. *Science, 293*(5534), 1495-1499.
Sewell, S. L., & Giorgio, T. D. (2009). Synthesis and enzymatic cleavage of dual-ligand quantum dots. *Materials Science & Engineering C-Materials for Biological Applications, 29*(4), 1428-1432.
Sharpe, A. H., & Freeman, G. J. (2002). The B7-CD28 superfamily. *Nat Rev Immunol, 2*(2), 116-126.
Shu, X. Z., Liu, Y., Luo, Y., Roberts, M. C., & Prestwich, G. D. (2002). Disulfide Cross-Linked Hyaluronan Hydrogels. *Biomacromolecules, 3*(6), 1304-1311.
Sica, A., Larghi, P., Mancino, A., Rubino, L., Porta, C., Totaro, M. G., et al. (2008). Macrophage polarization in tumour progression. *Semin Cancer Biol, 18*(5), 349-355.
Sica, A., Schioppa, T., Mantovani, A., & Allavena, P. (2006). Tumour-associated macrophages are a distinct M2 polarised population promoting tumour progression: Potential targets of anti-cancer therapy. *European journal of cancer (Oxford, England : 1990), 42*(6), 717-727.
Sluijter, J. P., Pulskens, W. P., Schoneveld, A. H., Velema, E., Strijder, C. F., Moll, F., et al. (2006). Matrix metalloproteinase 2 is associated with stable and matrix metalloproteinases 8 and 9 with vulnerable carotid atherosclerotic lesions: a

study in human endarterectomy specimen pointing to a role for different extracellular matrix metalloproteinase inducer glycosylation forms. *Stroke, 37*(1), 235-239.
Smith, R., Sewell, S. L., & Giorgio, T. D. (2008). Proximity-activated nanoparticles: in vitro performance of specific structural modification by enzymatic cleavage. *Int J Nanomedicine, 3*(1), 95-103.
Solan, N. J., Miyoshi, H., Carmona, E. M., Bren, G. D., & Paya, C. V. (2002). RelB cellular regulation and transcriptional activity are regulated by p100. *J Biol Chem, 277*(2), 1405-1418.
Song, E.-H., Manganiello, M. J., Chow, Y.-H., Ghosn, B., Convertine, A. J., Stayton, P. S., et al. (2012). In vivo targeting of alveolar macrophages via RAFT-based glycopolymers. *Biomaterials, 33*(28), 6889-6897.
Sovak, M. A., Bellas, R. E., Kim, D. W., Zanieski, G. J., Rogers, A. E., Traish, A. M., et al. (1997). Aberrant nuclear factor-kappaB/Rel expression and the pathogenesis of breast cancer. *J Clin Invest, 100*(12), 2952-2960.
Stacey, K. J., Ross, I. L., & Hume, D. A. (1993). Electroporation and DNA-dependent cell death in murine macrophages. *Immunol Cell Biol, 71*(2), 75-85.
Stadtman, E. R. (1990). Metal ion-catalyzed oxidation of proteins: Biochemical mechanism and biological consequences. *Free Radical Biology and Medicine, 9*(4), 315-325.
Stadtman, E. R., & Berlett, B. S. (1997). Reactive oxygen-mediated protein oxidation in aging and disease. *Chem Res Toxicol, 10*(5), 485-494.
Stadtman, E. R., & Levine, R. L. (2003). Free radical-mediated oxidation of free amino acids and amino acid residues in proteins. *Amino Acids, 25*(3), 207-218.
Stahl, P. D., & Ezekowitz, R. A. B. (1998). The mannose receptor is a pattern recognition receptor involved in host defense. *Current Opinion in Immunology, 10*(1), 50-55.
Stout, R. D., Jiang, C., Matta, B., Tietzel, I., Watkins, S. K., & Suttles, J. (2005). Macrophages sequentially change their functional phenotype in response to changes in microenvironmental influences. *J Immunol, 175*(1), 342-349.
Sumerlin, B. S., Tsarevsky, N. V., Louche, G., Lee, R. Y., & Matyjaszewski, K. (2005). Highly Efficient "Click" Functionalization of Poly(3-azidopropyl methacrylate) Prepared by ATRP. *Macromolecules, 38*(18), 7540-7545.
Sung, H. J., Luk, A., Murthy, N. S., Liu, E., Jois, M., Joy, A., et al. (2010). Poly(ethylene glycol) as a sensitive regulator of cell survival fate on polymeric biomaterials: the interplay of cell adhesion and pro-oxidant signaling mechanisms. *Soft Matter, 6*(20), 5196-5205.
Sung, H. J., Sakala Labazzo, K. M., Bolikal, D., Weiner, M. J., Zimnisky, R., & Kohn, J. (2008). Angiogenic competency of biodegradable hydrogels fabricated from polyethylene glycol-crosslinked tyrosine-derived polycarbonates. *Eur Cell Mater, 15*, 77-87.
Sung, H. J., Su, J., Berglund, J. D., Russ, B. V., Meredith, J. C., & Galis, Z. S. (2005). The use of temperature-composition combinatorial libraries to study the effects of biodegradable polymer blend surfaces on vascular cells. *Biomaterials, 26*(22), 4557-4567.

Tabas, I. (2010). Macrophage death and defective inflammation resolution in atherosclerosis. *Nat Rev Immunol, 10*(1), 36-46.
Tanaka, T., Decuzzi, P., Cristofanilli, M., Sakamoto, J. H., Tasciotti, E., Robertson, F. M., et al. (2009). Nanotechnology for breast cancer therapy. *Biomed Microdevices, 11*(1), 49-63.
Taylor, P. R., Brown, G. D., Herre, J., Williams, D. L., Willment, J. A., & Gordon, S. (2004). The Role of SIGNR1 and the β-Glucan Receptor (Dectin-1) in the Nonopsonic Recognition of Yeast by Specific Macrophages. *The Journal of Immunology, 172*(2), 1157-1162.
Taylor, P. R., Gordon, S., & Martinez-Pomares, L. (2005). The mannose receptor: linking homeostasis and immunity through sugar recognition. *Trends in Immunology, 26*(2), 104-110.
Thomas, S. N., van der Vlies, A. J., O'Neil, C. P., Reddy, S. T., Yu, S. S., Giorgio, T. D., et al. (2011). Engineering complement activation on polypropylene sulfide vaccine nanoparticles. *Biomaterials, 32*(8), 2194-2203.
Tsimikas, S., Willerson, J. T., & Ridker, P. M. (2006). C-reactive protein and other emerging blood biomarkers to optimize risk stratification of vulnerable patients. *J Am Coll Cardiol, 47*(8 Suppl), C19-31.
Tu, B. P., Ho-Schleyer, S. C., Travers, K. J., & Weissman, J. S. (2000). Biochemical Basis of Oxidative Protein Folding in the Endoplasmic Reticulum. *Science, 290*(5496), 1571-1574.
Vallabhapurapu, S., & Karin, M. (2009). Regulation and function of NF-kappaB transcription factors in the immune system. *Annu Rev Immunol, 27*, 693-733.
van der Vlies, A. J., O'Neil, C. P., Hasegawa, U., Hammond, N., & Hubbell, J. A. (2010). Synthesis of pyridyl disulfide-functionalized nanoparticles for conjugating thiol-containing small molecules, peptides, and proteins. *Bioconjugate chemistry, 21*(4), 653-662.
Van Rooijen, N., & Sanders, A. (1994). Liposome mediated depletion of macrophages: mechanism of action, preparation of liposomes and applications. *Journal of immunological methods, 174*(1-2), 83-93.
Vasievich, E. A., & Huang, L. (2011). The Suppressive Tumor Microenvironment: A Challenge in Cancer Immunotherapy. *Molecular Pharmaceutics, 8*(3), 635-641.
Velluto, D., Demurtas, D., & Hubbell, J. A. (2008). PEG-b-PPS diblock copolymer aggregates for hydrophobic drug solubilization and release: cyclosporin A as an example. *Mol Pharm, 5*(4), 632-642.
Verma, I. M., Stevenson, J. K., Schwarz, E. M., Van Antwerp, D., & Miyamoto, S. (1995). Rel/NF-kappa B/I kappa B family: intimate tales of association and dissociation. *Genes Dev, 9*(22), 2723-2735.
Watkins, S. K., Egilmez, N. K., Suttles, J., & Stout, R. D. (2007). IL-12 rapidly alters the functional profile of tumor-associated and tumor-infiltrating macrophages in vitro and in vivo. *J Immunol, 178*(3), 1357-1362.
Weischenfeldt, J., & Porse, B. (2008). Bone Marrow-Derived Macrophages (BMM): Isolation and Applications. *Cold Spring Harb Protoc, 2008*(12), pdb.prot5080-.
West, J. L., & Hubbell, J. A. (1998). Polymeric Biomaterials with Degradation Sites for Proteases Involved in Cell Migration. *Macromolecules, 32*(1), 241-244.

Williams, L. M., Sarma, U., Willets, K., Smallie, T., Brennan, F., & Foxwell, B. M. J. (2007). Expression of Constitutively Active STAT3 Can Replicate the Cytokine-suppressive Activity of Interleukin-10 in Human Primary Macrophages. *Journal of Biological Chemistry, 282*(10), 6965-6975.

Woo, K., Hong, J., Choi, S., Lee, H. W., Ahn, J. P., Kim, C. S., et al. (2004). Easy synthesis and magnetic properties of iron oxide nanoparticles. *Chemistry of Materials, 16*(14), 2814-2818.

Worbs, T., & Förster, R. (2007). A key role for CCR7 in establishing central and peripheral tolerance. *Trends in Immunology, 28*(6), 274-280.

Xiao, G., Rabson, A. B., Young, W., Qing, G., & Qu, Z. (2006). Alternative pathways of NF-kappaB activation: a double-edged sword in health and disease. *Cytokine Growth Factor Rev, 17*(4), 281-293.

Yu, S. S., Koblin, R. L., Zachman, A. L., Perrien, D. S., Hofmeister, L. H., Giorgio, T. D., et al. (2011). Physiologically relevant oxidative degradation of oligo(proline) cross-linked polymeric scaffolds. *Biomacromolecules, 12*(12), 4357-4366.

Yu, S. S., Lau, C. M., Thomas, S. N., Jerome, W. G., Maron, D. J., Dickerson, J. H., et al. (2012). Size-and charge-dependent non-specific uptake of PEGylated nanoparticles by macrophages. *International Journal of Nanomedicine, 7*, 799-813.

Yu, S. S., Ortega, R. A., Reagan, B. W., McPherson, J. A., Sung, H.-J., & Giorgio, T. D. (2011). Emerging applications of nanotechnology for the diagnosis and management of vulnerable atherosclerotic plaques. *Wiley Interdisciplinary Reviews: Nanomedicine and Nanobiotechnology, 3*(6), 620-646.

Yu, S. S., Scherer, R. L., Ortega, R. A., Bell, C. S., O'Neil, C. P., Hubbell, J. A., et al. (2011). Enzymatic- and temperature-sensitive controlled release of ultrasmall superparamagnetic iron oxides (USPIOs). *Journal of Nanobiotechnology, 9*, 7.

Zhang, J. L., Srivastava, R. S., & Misra, R. D. K. (2007). Core-shell magnetite nanoparticles surface encapsulated with smart stimuli-responsive polymer: Synthesis, characterization, and LCST of viable drug-targeting delivery system. *Langmuir, 23*(11), 6342-6351.